

University of Central Florida

**STARS**

---

Electronic Theses and Dissertations

---

2013

## Injection Locking Of Semiconductor Mode-locked Lasers For Long-term Stability Of Widely Tunable Frequency Combs

Charles Williams

*University of Central Florida*



Part of the [Electromagnetics and Photonics Commons](#), and the [Optics Commons](#)

Find similar works at: <https://stars.library.ucf.edu/etd>

University of Central Florida Libraries <http://library.ucf.edu>

This Doctoral Dissertation (Open Access) is brought to you for free and open access by STARS. It has been accepted for inclusion in Electronic Theses and Dissertations by an authorized administrator of STARS. For more information, please contact [STARS@ucf.edu](mailto:STARS@ucf.edu).

---

### STARS Citation

Williams, Charles, "Injection Locking Of Semiconductor Mode-locked Lasers For Long-term Stability Of Widely Tunable Frequency Combs" (2013). *Electronic Theses and Dissertations*. 2594.  
<https://stars.library.ucf.edu/etd/2594>

# **INJECTION LOCKING OF SEMICONDUCTOR MODE-LOCKED LASERS FOR LONG-TERM STABILITY OF WIDELY TUNABLE FREQUENCY COMBS**

by

CHARLES G. WILLIAMS

B.S. University of Missouri – Rolla, 2006

M.S. University of Central Florida, 2008

A dissertation submitted in partial fulfillment of the requirements  
for the degree of Doctor of Philosophy  
in the College of Optics and Photonics  
at the University of Central Florida  
Orlando, Florida

Spring Term  
2013

Major Professor: Peter J. Delfyett

© 2013 Charles G Williams

## **ABSTRACT**

Harmonically mode-locked semiconductor lasers with external ring cavities offer high repetition rate pulse trains while maintaining low optical linewidth via long cavity storage times. Single frequency injection locking generates widely-spaced and tunable frequency combs from these harmonically mode-locked lasers, while stabilizing the optical frequencies. The output is stabilized long-term with the help of a feedback loop utilizing either a novel technique based on Pound-Drever-Hall stabilization or by polarization spectroscopy. Error signals of both techniques are simulated and compared to experimentally obtained signals. Frequency combs spaced by 2.5 GHz and ~10 GHz are generated, with demonstrated optical sidemode suppression of unwanted modes of 36 dB, as well as RF supermode noise suppression of 14 dB for longer than 1 hour. In addition to the injection locking of actively harmonically mode-locked lasers, the injection locking technique for regeneratively mode-locked lasers, or Coupled Opto-Electronic Oscillators (COEOs), is also demonstrated and characterized extensively.



For my wife, Allison, who locks me away in rooms to force help me to write, and brings me food and encouragement all the while.

And for my mother, Joyce, who did the same for many years of my life to get me to this point, when the writing had more to do with the Titanic than Injection Locked Lasers.

## **ACKNOWLEDGMENTS**

I would first like to acknowledge Prof. Peter Delfyett for his teaching and guidance throughout my dissertation research, as well as my CREOL professors and committee members for the same: Professors Patrick LiKamWa, Eric Van Stryland, and David Hagan, and Dr. Richard DeSalvo. I owe a great deal of my early understanding of lasers and scientific training to my former labmate, Dr. Franklyn Quinlan.

In addition, many members of the Ultrafast Photonics Group, past and present, have helped immensely in thinking and talking through the concepts herein. Those in particular whose discussions and vigorous debates have stood out in my mind are: Dr. Sangyoun Gee, Dr. Dimitrios Mandridis, Dr. Josue Davila-Rodriguez, Dr. Nazanin Hoghooghi, Marcus Bagnell, Tony Klee, Kristina Bagnell, Dr. Sarper Ozharar, Dr. Ibrahim Ozdur, Dr. Ji-Myung Kim, Abhijeet Ardey, and Edris Sarailou.

Separately, I would like to acknowledge the work of all past UP members, whose work I was privileged to build upon, and those I have been in the group with for sharing your research and allowing me to gain knowledge and experience far beyond what I could gather on my own.

Lastly, many friends in CREOL and out have helped immensely in scientific discussions, paper editing, and moral support: Dr. Matthew Weidman, Mark Ramme, Dr. John Broky, Matthew Weed, James Williams Jr., Dr. Robert Bernath, Dr. Casey Boutwell, Kyle Douglass and countless others in ways large and small.

# TABLE OF CONTENTS

LIST OF FIGURES .....	VIII
LIST OF ABBREVIATIONS .....	XIII
CHAPTER 1: INTRODUCTION.....	1
1.1 Definitions .....	2
1.2 Applications.....	3
1.2.1 Optical Time Domain Multiplexing .....	3
1.2.2 Optical Arbitrary Waveform Generation .....	4
1.2.3 Coherent Communication.....	5
1.2.4 RF Photonics and Optical Clocks .....	6
1.2.5 Multiheterodyne Spectroscopy .....	7
1.2.6 Photonic Analog-to-Digital Conversion .....	9
CHAPTER 2: HARMONICALLY MODE-LOCKED LASERS .....	11
2.1 Harmonic Mode-Locking Mechanism.....	11
2.2 Sources of Noise in Harmonically Mode-Locked Lasers .....	12
CHAPTER 3: INJECTION LOCKING OF OSCILLATORS.....	14
3.1 Applications of Injection Locking.....	16
3.2 Semiconductor Cavity Dynamics of Injection Locking.....	17
CHAPTER 4: LASER CAVITY STABILIZATION VIA POUND-DREVER-HALL METHOD .....	22
4.1 Pound-Drever-Hall Cavity Stabilization Overview .....	22
4.2 Modified Pound-Drever-Hall Stabilization Error Signal Simulation .....	25
4.2.1 Conventional Pound-Drever-Hall Error Signal.....	25
4.2.2 Simulated Cavity Resonances .....	28
4.2.3 Modified Pound-Drever-Hall Simulations .....	30
CHAPTER 5: CW INJECTION LOCKING OF AN ACTIVELY MODE-LOCKED LASER .....	38
5.1 Actively Mode-Locked Injection Locked Laser Setup .....	38
5.2 Laser Preparation for Frequency Comb Generation .....	40
5.2.1 Laser Parameters for Effective Injection Locking.....	40
5.2.2 Injection Locking Procedure.....	41
5.2.3 Pound-Drever-Hall Stabilization Error Signal Locking Exploration.....	43
5.3 Actively mode-locked injection locked laser results .....	46
CHAPTER 6: LASER CAVITY STABILIZATION VIA POLARIZATION SPECTROSCOPY .....	51
6.1 Polarization Spectroscopy: Introduction and Experimental Setup.....	52
6.1.1 Polarization Spectroscopy Error Signal Locking Exploration.....	53
6.2 Polarization Spectroscopy Stabilization Error Signal Simulation.....	56
6.2.1 Simulated Cavity Resonances .....	56
6.3 Stabilization via Polarization Spectroscopy: Results and Conclusion .....	59

CHAPTER 7: CW INJECTION LOCKING OF A COUPLED OPTO-ELECTRONIC OSCILLATOR .....	61
7.1 Regenerative Mode-Locking.....	62
7.2 Injection Locked COEO Experimental Setup.....	64
7.3 Injection Locked COEO Results.....	66
7.3.1 Optical, RF Spectra and Time Domain Traces .....	66
7.3.2 Amplitude and Phase Noise .....	71
7.3.3 Allan Deviation .....	75
7.4 RF Frequency dependence on Injected Optical Frequency of Injection Locked COEO .....	78
7.4.1 Experimental Results .....	80
7.4.2 Discussion and Conclusion .....	82
CHAPTER 8: CONCLUSION .....	83
APPENDIX A: ALLAN DEVIATION MEASUREMENT .....	84
Equation and its Explanation.....	88
Experimental Measurement .....	89
Simulation .....	91
Examples and Explanations .....	94
APPENDIX B: LIST OF PUBLICATIONS AND CONFERENCES .....	104
Primary Author .....	105
Secondary Author.....	106
APPENDIX C: MATLAB CODE USED FOR SIMULATIONS .....	109
Pound Drever Hall and Polarization Spectroscopy Error Signal .....	110
Allan Deviation Simulation .....	116
REFERENCES.....	118

## LIST OF FIGURES

<b>Figure 1.1</b> Schematic of Optical Time Domain Multiplexing as a utilization of mode-locked laser pulse trains. Pulses are directed to different modulating signals via an active optical switching mechanism. Each user then sees a lower repetition rate pulse train on which to impart a signal. Original pulse train is reconstituted and transmitted to another switch, separated again, and sent to corresponding receivers.	4
<b>Figure 1.2</b> Schematic of Optical Arbitrary Waveform Generation (OAWG). Individual frequency components of a frequency comb are isolated via wavelength division multiplexing (WDM), affected individually using phase and amplitude modulation (PM and AM, respectively). When remultiplexed, a repetitive arbitrary optical signal is generated.	5
<b>Figure 1.3</b> Schematic of an optical coherent communication setup. Each optical frequency component of a frequency comb is encoded by a unique user's signal, resulting in a seemingly arbitrary signal sent to the receiver side, where the individual signals are demultiplexed and received individually.	6
<b>Figure 1.4</b> Conceptual diagram of photonic enabled RF arbitrary waveform generation. An RF waveform corresponding to the intensity of the arbitrary optical waveform is generated with instantaneous frequency up to that of the photodetector bandwidth.	7
<b>Figure 1.5</b> Schematic and concept of multiheterodyne spectroscopy. Two mode-locked lasers with differing repetition rates are combined and photodetected. Combines from each laser are paired up to produce a spectrum of RF heterodyne beats, preserving the relative frequency and phase between combine pairs.	8
<b>Figure 1.6</b> A generalized picture of photonic enabled analog-to-digital conversion wherein mode-locked laser pulses with ultra-low timing jitter and pulse-to-pulse energy fluctuations are modulated using the signal to be converted. Each pulse samples the waveform at a set interval and its amplitude value can then be independently recorded in digital format.	10
<b>Figure 2.1</b> Fundamental (a) versus harmonic (b) mode-locking in the time domain for laser cavities of the same length showing multiple pulses traversing the harmonically mode-locked cavity. Representations of the spectral output in the fundamental (c) and harmonic (d) mode-locking cases showing the presence of optical supermode sets in a HMLL. The Semiconductor Optical Amplifier (SOA) gain media are shown as red triangles and the IMs are shown in the lower part of the cavities, along with the input sine wave to the respective modulators. In this example the HMLL contains three pulses traversing the cavity.	12
<b>Figure 3.1.</b> A slaved cavity resonance and its relevant injection locking properties. The locking range is demonstrated by the vertical cyan lines, as well as the injection lock phase limits of $\pm \pi/2$ , while the regenerative gain curve of the resonance (solid blue lines) is shown versus optical frequency. Within the locking range, the normalized output power is clamped, approximated by a higher order Gaussian (green circles). The normalized transmission of a passive cavity, defined by the real part of the Airy function, is shown in solid green. The phase shift that an injected tone experiences as it moves across the resonance is shown in red and is shown as an arcsin shape extending from $\pi/2$ to $-\pi/2$ over the locking range.	15

<b>Figure 3.2.</b> Semiconductor laser cavity resonances with non-zero alpha parameters, shifting resonance phase downward and broadening the injection locking range. Note the difference in frequency scale between figure a) and figures b) and c).....	19
<b>Figure 4.1.</b> Representation of the injection seed frequency and phase modulation sidebands injected into a HMLL. Note that the phase modulation sidebands are not resonant with the optical cavity when the injection seed frequency is within a cavity resonance injection locking range.....	24
<b>Figure 4.2.</b> a) Conventional PDH Error Signal derived from a cavity with $R = 0.99$ and PM frequency of $1.13 \cdot \text{FSR}$ . b) Passive FPE cavity normalized transmission (blue) and phase (green), according to the Airy function governing passive cavity behavior.....	27
<b>Figure 4.3.</b> Cavity amplitude and phase response within injection locking ranges for the center resonance and two nearest neighbor resonances, which PM sidebands interact with while the carrier is near zero detuning.....	29
<b>Figure 4.4.</b> Comparison of experimentally obtained error signal (blue, PM frequency $\sim 15.047 \cdot \text{FSR}$ ) to simulated error signal (red) with the parameters shown. The multiple cavity amplitude responses are shown in green, while their phase responses are shown in cyan.....	32
<b>Figure 4.5.</b> Comparison of experimentally obtained error signal (blue) to simulated error signal (red), as well as copies of simulated signals shifted by one FSR in the positive detuning direction (pink) and negative detuning direction (black) to illustrate the origin of triangle waveform features between each cavity resonance. ....	34
<b>Figure 4.6.</b> Comparison of realistic locking signal to simulation results. Visual fitting was able to closely approximate either a) the center features including the differential features used for feedback stabilization, or b) the overall shape of the error signal.....	36
<b>Figure 5.1.</b> Laser system schematic of actively mode-locked injection locked laser with long-term feedback. BPF: Optical Bandpass Filter; DBM: RF Double Balanced Mixer; DCF: Dispersion Compensating Fiber; FPS: Fiber Phase Shifter; IC: Injection Coupler; IM: Intensity Modulator; IPM: Injection Power Monitor; IS: Isolator; ISL: Injection Seed Laser; LPF: RF Low Pass Filter; OC: Output Coupler; PC: Polarization Controller; PD: Photodetector; PIC: PI Controller; PM: Phase Modulator; PS: RF Phase Shifter; RFA: Low Noise RF Amplifier; SOA: Semiconductor Optical Amplifier; VOA: Variable Optical Attenuator; VOD: Variable Optical Delay.....	39
<b>Figure 5.2.</b> a) Optical and b) Photodetected RF spectra of a harmonically mode-locked laser with injection from the single frequency injection laser, but not yet injection-locked. ....	42
<b>Figure 5.3.</b> Error Signal for laser system stabilization via PDH. The system was temporarily stabilized at the labeled points shown for observation of the locking characteristics, shown in the following figure..	44
<b>Figure 5.4.</b> a) Optical (0.05 nm resolution) and b) RF (60 MHz span; 6.8 kHz RBW) spectral observations of injection locking at various points along the PDH error signal, shown in the previous figure. Optimal injection locking was found at point 'G' (light purple). Other injection points of decent quality (points 'D' and 'I') occur where PM sidebands are aligned with other cavity resonances and therefore injection lock them.....	45
<b>Figure 5.5.</b> Optical spectra of the actively mode-locked laser free running, or without optical injection (black) and injection locked (red). (a) shows the entire mode-locked spectrum, while (b) is a high	

resolution view of a portion of the spectra. Two tones of the injection selected supermode are visible with a spacing of 2.5 GHz, while 36 dB suppression of the unselected supermodes is shown.....	46
<b>Figure 5.6.</b> RF spectra of the laser system in the free running (black) and injection locked (red) case. (a) shows the suppression of RF supermode noise spurs by 14 dB due to optical injection. In (b) the suppression of RF supermode noise spurs for fifteen minutes is shown while the modified PDH feedback loop is in use. ....	48
<b>Figure 5.7.</b> (a) Modified Pound-Drever-Hall error signal of the injection locked actively mode-locked laser cavity with CW injection. The discriminant portion of the error signal used for locking the cavity is highlighted in red. (b) Ideal Pound-Drever-Hall error signal shape for a passive cavity such as an etalon. The discriminant is the sharp vertical line in the center feature of the signal. ....	49
<b>Figure 5.8.</b> Residual phase noise of the laser in free running and injection locked states. In free running operation, an integrated timing jitter from 1Hz to 100 MHz of 427 fs was measured. Optical injection reduced the integrated jitter to 121 fs. ....	50
<b>Figure 5.9.</b> Pulse-to-pulse energy fluctuation, or amplitude noise of the laser in free running and injection locked states. In free running operation, integrated AM noise from 1Hz to 100 MHz of 0.61% was measured. Optical injection reduced this integrated AM noise to 0.24%. ....	50
<b>Figure 6.1.</b> Schematic of injection locked HMLL with long-term stabilization via polarization spectroscopy. ....	52
<b>Figure 6.2.</b> Error Signal for laser system stabilization via polarization spectroscopy. The system was temporarily stabilized at the labeled points shown for observation of the locking characteristics, shown in the following figure. ....	54
<b>Figure 6.3.</b> a) Optical (0.05 nm resolution) and b) RF (60 MHz span; 6.8 kHz RBW) spectral observations of injection locking at various points along the HC error signal, shown in the previous figure. Optimal injection locking was found at point 'K' (dark blue), while best error signal locking was found at point 'E'. ....	55
<b>Figure 6.4.</b> Amplitude (blue) and phase (green) response of slaved cavity resonance with gain, as well as original HC error signal (red) and signal of the HC technique applied to a semiconductor cavity with gain (teal). ....	57
<b>Figure 6.5.</b> Experimentally obtained polarization spectroscopy error signal (green) comparison to simulated (blue). ....	58
<b>Figure 6.6.</b> (a) Optical spectra of HMLL not subject to optical injection (black) and injection locked and stabilized via polarization spectroscopy (blue). (b) High resolution optical spectra of HMLL output showing frequency comb generation under optical injection with high OSNR. The latter curve was artificially offset by -10 dB to illustrate the absence of PM sidebands on each combline. ....	59
<b>Figure 6.7.</b> Photodetected RF spectra of the injection locked laser stabilized via the two methods. Note the absence of an RF sideband 550 MHz offset from the 10.24 GHz carrier for the HC stabilization method. ....	60
<b>Figure 7.1</b> Schematic of a typical Coupled Opto-Electronic Oscillator. The optical cavity is shown in blue, with gain (red triangle) and intensity modulator (left). The electronic part of the opto-electronic cavity is	

shown in black, where the output is photodetected (right), filtered (not shown for simplicity), amplified (black triangle) and fed back into the intensity modulator. ....	63
<b>Figure 7.2</b> Injection Locked COEO system schematic. BPF, Bandpass Filter; DBM, Double Balanced Mixer; DCF, Dispersion Compensating Fiber; FPS, Fiber Phase Shifter; IC, Injection Coupler; IM, Intensity Modulator; ISL, Injection Seed Laser; ISO, Isolator; LPF, Lowpass Filter; OC, Output Coupler; PC, Polarization Controller; PD, Photodetector; PIC, Proportional-Integral Controller; PM, Phase Modulator; PS, Phase Shifter; RFA, RF Amplifier; SOA, Semiconductor Optical Amplifier. ....	65
<b>Figure 7.3</b> (a) Optical spectra of the free-running (black) and injection-locked (red) states. The injection seed frequency is denoted by a black arrow. (b) High resolution optical spectra (100 MHz resolution). The optical modes in free-running operation (black) are too closely spaced (11 MHz) for the instrument to resolve. ....	67
<b>Figure 7.4</b> (a) RF power spectrum of the photodetected COEO optical output, free-running (black) and injection-locked (red) with fundamental RF tone and one supermode noise spur, suppressed via injection locking. (b) Zoomed view of fundamental RF tones at ~10.24 GHz.....	69
<b>Figure 7.5</b> Time domain normalized (a) sampling scope and (b) autocorrelation traces of the COEO output in both free-running (black) and injection-locked (red) cases.....	70
<b>Figure 7.6</b> Power spectral density of the amplitude noise of the injection-locked COEO for various injection powers: black, free-running; red, ~9 $\mu$ W; cyan, 14 $\mu$ W; orange, 20 $\mu$ W. Pulse-to-pulse energy fluctuation for each case, integrated from higher to lower offset frequencies. ....	71
<b>Figure 7.7</b> Supermode noise spur detail of the absolute phase noise power spectral density of the COEO system in the free-running (black) and injection-locked (red) cases. Blue dashed peaks are spurious results of the frequency discriminator measurement. Offset frequency is shown in linear scale to highlight the suppression of supermode noise spurs at higher offsets. Arrows indicate modes used in timing jitter estimation. ....	73
<b>Figure 7.8</b> Allan Deviation measurements of the Injection Locked COEO from the photodetected optical output for both injection locked (red triangle) and free-running (black) states. ....	76
<b>Figure 7.9</b> (a) Schematic of the injection locked COEO with feedback stabilization. (b) Experimental setup for measurement of optical-to-RF instability transfer.....	79
<b>Figure 7.10</b> (a) Allan Deviation measurements of the free-running and injection locked COEO, as well as of heterodyne beat signals between the injection seed lasers and an optical frequency reference. (b) Instability transfer from the optical injection frequency to the COEO RF output via sinusoidal modulation of the injection seed frequency. ....	81
<b>Figure A.1</b> Simulated instantaneous frequency values of a non-stable signal at a starting frequency of 10 GHz. ....	87
<b>Figure A.2</b> Typical Allan Deviation plot showing calculated fractional deviation values for increasing measurement times. ....	88
<b>Figure A.3</b> a) Oscillating signal of interest in blue with zero crossings shown by black dots. Boxes shown represent average frequency measurement times of b) 100 ns, c) 1 $\mu$ s, d) 10 $\mu$ s, and e) 100 $\mu$ s. ....	90
<b>Figure A.4</b> Instantaneous frequency values (blue) and averages (black) over four instantaneous time increments. ....	92



<b>Figure A.5</b> Instantaneous frequency values (blue) and averages (light blue) over 16 instantaneous time increments. ....	92
<b>Figure A.6</b> Instantaneous frequency values (blue) and averages (green) over 64 instantaneous time increments. ....	93
<b>Figure A.7</b> Instantaneous frequency values (blue) and averages (blue straight lines) over 256 instantaneous time increments. ....	93
<b>Figure A.8</b> Instantaneous frequency values (top, blue) and averages over several instantaneous time increments. ....	94
<b>Figure A.9</b> a) Instantaneous frequency values starting at 10 GHz and calculated with equal parts white noise and random walk. b) ADEV curve of the frequency values. c) Modified STDEV curve (blue) and difference between ADEV and STDEV (green) illustrating a lack of information given by such a measurement.....	95
<b>Figure A.10</b> a) A second example of instantaneous frequency values starting at 10 GHz and calculated with equal parts white noise and random walk. b) ADEV curve of the frequency values. c) Modified STDEV curve (blue) and difference between ADEV and STDEV (green). ....	96
<b>Figure A.11</b> a) Instantaneous frequency values starting at 10 GHz and calculated with five times more white noise than random walk. b) ADEV curve of the frequency values. c) Modified STDEV curve (blue) and difference between ADEV and STDEV (green).....	98
<b>Figure A.12</b> a) Instantaneous frequency values starting at 10 GHz and calculated with five times more white noise than random walk, as well as a rounding error and sinusoidal modulation introduced onto the signal. b) ADEV curve of the frequency values. Note the effect of the modulation on the curve shape at $8 \cdot \tau_0$ . c) Modified STDEV curve (blue) and difference between ADEV and STDEV (green).....	100
<b>Figure A.13</b> a) A second example of instantaneous frequency values starting at 10 GHz and calculated with five times more white noise than random walk, as well as a rounding error and sinusoidal modulation introduced onto the signal. b) ADEV curve of the frequency values. Note that the modulation is at a quarter of the frequency of the previous figure, and the associated anomaly in the ADEV curve is at $32 \cdot \tau_0$ , four times that of the previous example. c) Modified STDEV curve (blue) and difference between ADEV and STDEV (green).....	101
<b>Figure A.14</b> A subset of the instantaneous frequency values from last example along with measurement time averages used to calculate the ADEV curve. ....	103

## LIST OF ABBREVIATIONS

ADC	Analog-to-Digital Conversion (of data signals)
ADEV	Allan Deviation
AM	Amplitude Modulation
ASE	Amplified Spontaneous Emission
AVAR	Allan Variance
BPD	Balanced Photodetection
BPF	Bandpass Filter
CEP	Carrier-to-Envelope Phase
COEO	Coupled Opto-Electronic Oscillator
CW	Continuous Wave, here also implying ‘single frequency’
D	Fiber Dispersion Parameter
dB	Decibels
DBM	Double Balanced Mixer
DC	Direct Current, here meaning very low relative frequencies
DCF	Dispersion Compensating Fiber
$f$	RF frequency

FPS	Fiber Phase Shifter
FSR	Free Spectral Range
FWHM	Full Width at Half-Maximum
HC	Hänsch-Couillaud (Polarization Spectroscopy Stabilization Scheme)
HMLL	Harmonically Mode-Locked Laser
Hz	Hertz, frequency of 1/seconds
IC	Injection Coupler
IM	Intensity Modulator
IPM	Injection Power Monitor
IS(O)	Isolator
ISL	Injection Seed Laser
LEF	Linewidth Enhancement Factor, also $\alpha$
LIDAR	Laser Radar
LPF	Low Pass Filter
nm	nanometer, unit of optical wavelength
$\nu$ , $\nu$	Optical Frequency
OAWG	Optical Arbitrary Waveform Generation

OC	Output Coupler
$\omega$ , omega	Angular Optical Frequency ( $2\pi \cdot \nu$ )
$\omega_0$	Center of Cavity Resonance
OTDM	Optical Time-Domain Multiplexing
PBS	Polarization Beam Splitter
PC	Polarization Controller
PD	Photodetector
PDH	Pound-Drever-Hall (Stabilization Scheme)
PIC	Proportional-Integrating Controller
PM	Phase Modulation/Modulator
PS	RF Phase Shifter
PSD	Power Spectral Density
R	Mirror Reflectivity
RBW	Resolution Bandwidth, typically of RF spectrum analyzer
RF	Radiofrequency
RFA	RF Amplifier
RW	Random Walk

s	Seconds
SNS	Supermode Noise Spur
SOA	Semiconductor Optical Amplifier
STDEV	Standard Deviation
T	Period of cavity pulse propagation
TF	Transfer Function of frequency discriminator measurement
VOA	Variable Optical Attenuator
VOD	Variable Optical Delay
W	Watts
WN	White Noise
WDM	Wavelength Division Multiplexing

## CHAPTER 1: INTRODUCTION

Optical frequency combs have gained a lot of attention lately for their applicability in a wide range of fields, especially with the advent of absolute frequency stability due to carrier envelope phase stabilization [1-3]. By precise control of only two parameters, the repetition rate and the carrier envelope phase, the frequency of each optical tone within the comb spectrum can be determined with sub-Hz accuracy [4]. Indeed, optical frequency comb technology has found a multitude of uses, from precise control of the carrier envelope phase for high-harmonic generation [5], to optical frequency metrology [1, 6, 7], optical clocks [8, 9], and high resolution laser ranging [10-12]. Other applications, such as coherent communication, signal processing, and astronomy [13-16], require the frequency stability of optical combs with high repetition rates (and hence combline separation), typically greater than 10 gigahertz [17].

Traditionally, frequency comb repetition rates have stayed in the regime of 1 GHz and below [1, 4-8]. Various avenues are being explored for creating multi-gigahertz spaced frequency combs, including a fundamentally mode-locked Ti:Sapphire system [18], external modulation of continuous wave laser sources [19, 20], rational harmonic mode-locking [21] and external filtering of low-repetition rate comb sources [15, 22]. Passive fundamental mode-locking in fiber laser sources has only recently been shown to produce GHz spaced frequency combs with much engineering of the doping concentration within a small cavity [23]. Previously, the fastest repetition rates of fundamentally mode-locked fiber lasers were limited to  $< 1$  GHz due to long cavity lengths [24, 25].

Semiconductor-based mode-locked lasers are optimal for producing frequency combs with multi-gigahertz spacing, due to the short gain recovery time of the semiconductor [26], with the added benefit of high wall-plug efficiency due to direct electrical pumping. By incorporating a long external cavity and employing harmonic mode-locking, higher repetition rates can be achieved while decreasing the optical linewidth. Low timing jitter and pulse-to-pulse energy fluctuation can be realized as well, making semiconductor based laser systems ideal for such applications as optical time domain multiplexing (OTDM) [27] and optical signal processing, including analog to digital conversion (ADC) [28] and line-by-line pulse shaping [29]. Coherent communication such as phase shift keying and quadrature amplitude modulation can also be achieved [30, 31]. In addition, the set of widely spaced phase-locked frequency components can be exploited for the purposes of optical arbitrary waveform generation (OAWG) [27, 32] and frequency metrology [33].

Furthermore, the potential for low-noise, high-repetition rate, stand-alone oscillators offering both optical and radio frequency (RF) outputs through the use of regenerative mode-locking would be an added benefit to many of the above applications where cost, weight, size, and increased portability are important. To that end, a stand-alone system utilizing regenerative mode-locking and injection locking to produce an optical frequency comb is presented and fully characterized.

## **1.1 Definitions**

‘Frequency comb,’ in the context of this work, is defined as a set of discrete optical frequency components with a fixed phase relationship relative to one another.

Other works require that the laser's carrier-to-envelope phase (CEP) be actively stabilized for the output spectrum to be deemed a frequency comb, but this is not strictly required in the applications outlined here for the laser sources described here. Therefore, in this document, the term is not restricted to lasers with CEP stabilization.

Harmonically mode-locked lasers (HMLLs), as described in later chapters, exhibit a unique output spectrum wherein multiple comb groups are interleaved with each other. The number of these groups is determined by the number of pulses in the cavity and the integer ratio of the pulse repetition rate to the cavity fundamental frequency. Each of these groups is referred to as an axial mode group or a supermode. As each of these groups contains the necessary fixed phase relationship, suppression of all but one group in the output spectrum will generate a frequency comb, as defined above.

## **1.2 Applications**

Potential applications for high repetition rate mode-locked lasers and frequency comb sources in both the frequency and time domains are numerous. A few of these applications are summarized here.

### **1.2.1 Optical Time Domain Multiplexing**

The creation of pulse trains in the multi-gigahertz regime with low pulse-to-pulse timing jitter is a distinct advantage of external cavity semiconductor-based laser systems. Communication via optical time division multiplexing (OTDM) utilizes any number of communication schemes, with the common feature that the low noise pulse train use is split amongst many users [27], as illustrated in Figure 1.1. The optical



pulses are demultiplexed to be modulated for signal transmission by each individual user. This means that each user will use a 'pulse train' at a lower repetition rate equal to the original repetition rate divided by the number of users. The pulses are then multiplexed before transmission to the end-receiver [34, 35].

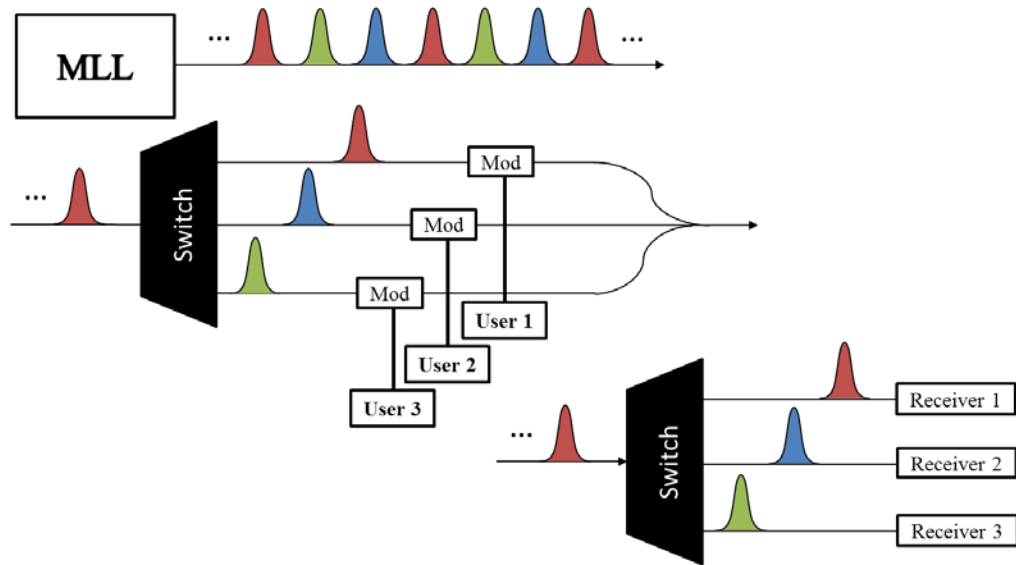


**Figure 1.1** Schematic of Optical Time Domain Multiplexing as a utilization of mode-locked laser pulse trains. Pulses are directed to different modulating signals via an active optical switching mechanism. Each user then sees a lower repetition rate pulse train on which to impart a signal. Original pulse train is reconstituted and transmitted to another switch, separated again, and sent to corresponding receivers.

### 1.2.2 Optical Arbitrary Waveform Generation

Frequency comb sources offer a set of frequency components coherent with each other, which typically add together to form a periodic set of pulses in the time domain. However, by spectral demultiplexing and affecting the phase and amplitude of each individual combline, an arbitrary optical waveform can be created out of the

resulting recombined optical signal. This is shown in Figure 1.2. Further uses for this technology lie in the signal processing and laser RADAR (LIDAR) fields [27, 32].

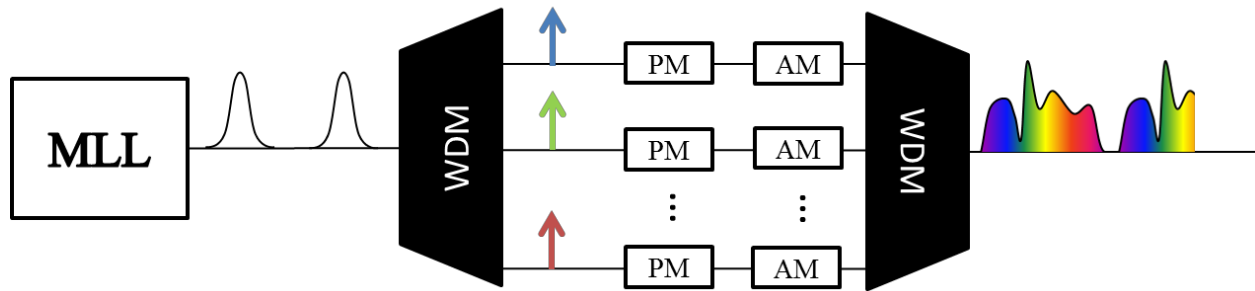


**Figure 1.2** Schematic of Optical Arbitrary Waveform Generation (OAWG). Individual frequency components of a frequency comb are isolated via wavelength division multiplexing (WDM), affected individually using phase and amplitude modulation (PM and AM, respectively). When remultiplexed, a repetitive arbitrary optical signal is generated.

### 1.2.3 Coherent Communication

The setup for coherent communication (Figure 1.3) is much the same as that of optical arbitrary waveform generation. For this application, the signals fed into the amplitude and phase modulators contain information for transmission to a distant receiver. Each user's information content is encoded on a single optical tone. The tones are remultiplexed and transmitted over optical fiber, only to be demultiplexed and coherently detected and read on the receiver end using knowledge of the original optical frequency and phase content [30, 31].

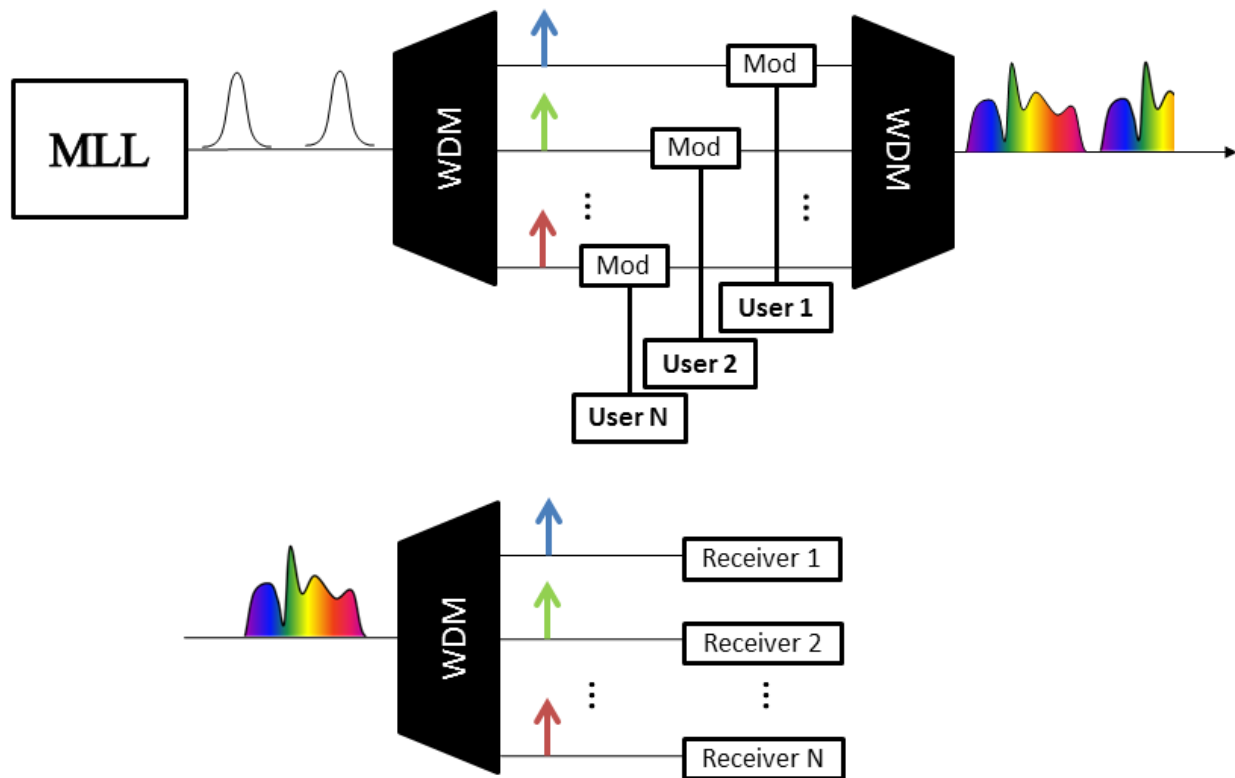


**Figure 1.3** Schematic of an optical coherent communication setup. Each optical frequency component of a frequency comb is encoded by a unique user's signal, resulting in a seemingly arbitrary signal sent to the receiver side, where the individual signals are demultiplexed and received individually.

### 1.2.4 RF Photonics and Optical Clocks

Building on the principles of optical arbitrary waveform generation, an arbitrary optical signal can be photodetected to produce arbitrary RF waveforms, shown in Figure 1.4. These waveforms, which contain high instantaneous frequencies up to the bandwidth of the photodetector used, are often less cumbersome to obtain by this method than by traditional electronic arbitrary waveform generation [27].

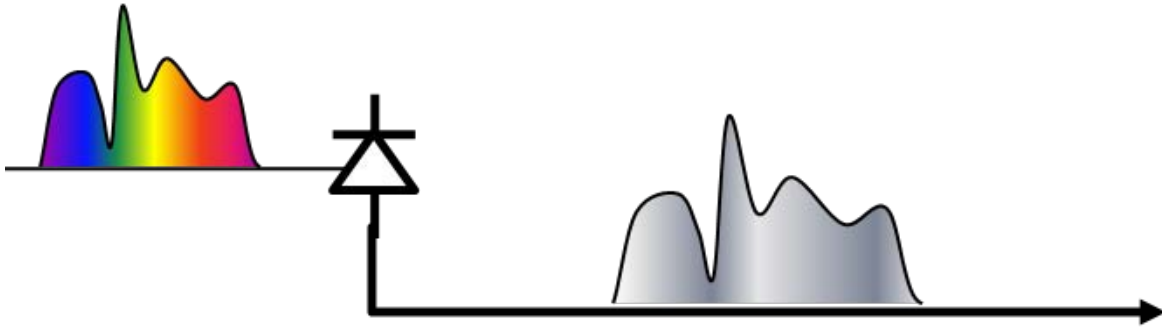


**Figure 1.4** Conceptual diagram of photonic enabled RF arbitrary waveform generation. An RF waveform corresponding to the intensity of the arbitrary optical waveform is generated with instantaneous frequency up to that of the photodetector bandwidth.

Frequency comb sources are being used to push the state-of-the-art of long-term stability of time standards. By stabilizing the optical frequency components in a comb, the beating of the optical tones with each other on a photodetector will produce a low-noise microwave signal [36]. This signal can be used to trigger subsequent modulators acting on the pulse train, such as in arbitrary waveform generators or ADCs, or can be combined with electronic counters to produce a stable clock.

An extension of this concept is radio-over-fiber, wherein a few ( $>2$ ) comb lines with stable frequency separation are modulated and transmitted over optical fiber then photodetected at the receiver end to produce a transmitted microwave signal [37].

### 1.2.5 Multiheterodyne Spectroscopy

The burgeoning field of multiheterodyne spectroscopy utilizes a frequency comb to probe the phase and amplitude information of an unknown multi-wavelength signal with different periodicity [10, 38-41], as shown in Figure 1.5. This field can also benefit from easily tunable frequency comb spacing by granting control over the detuning frequency between the two signal pulse-trains.

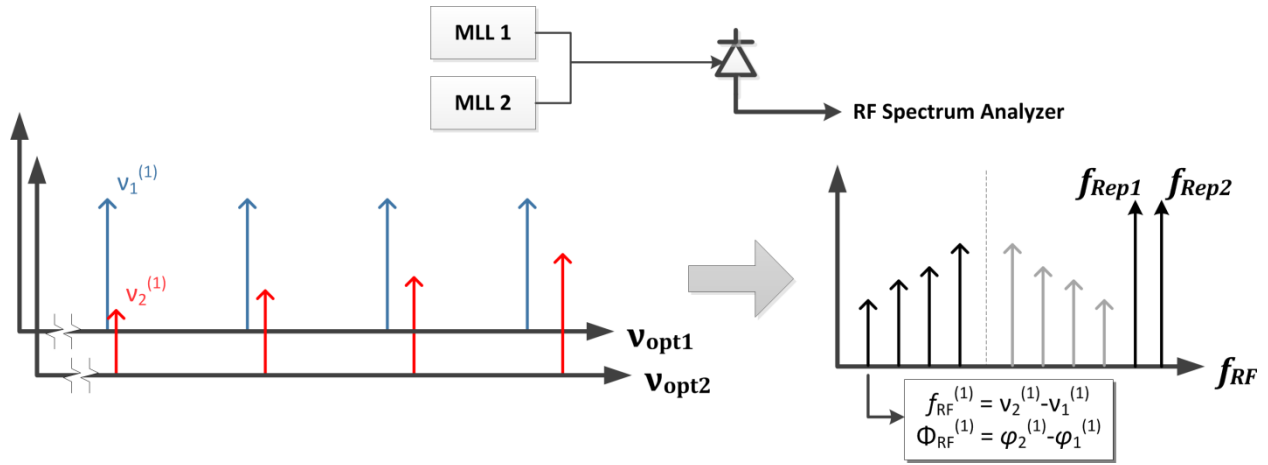


**Figure 1.5** Schematic and concept of multiheterodyne spectroscopy. Two mode-locked lasers with differing repetition rates are combined and photodetected. Combines from each laser are paired up to produce a spectrum of RF heterodyne beats, preserving the relative frequency and phase between combine pairs.

The versatility of multiheterodyne spectroscopy depends on a comb source with easily tunable repetition rate. In addition, narrow optical linewidth can assist in providing higher quality measurement of the amplitude and phase. Injection locking for frequency comb generation achieves both goals, provided a narrow linewidth, stable CW source is used. In multiheterodyne spectroscopy, two frequency periodic optical sources with different periodicities are combined in a coupler. After photodetection of this composite signal, the RF signal is analyzed. With careful choice of periodicities for each source, inter-source comb beatings will exhibit themselves in individually unique regions of the RF spectrum corresponding to the frequency difference between the pair of optical components used to produce them. Because the phase of a particular RF heterodyne beat is also determined by the phase difference between the optical pair, an optical waveform can effectively be ‘sampled’ into the RF domain, thereby allowing for spectral phase measurement of a particular source through time domain measurement and

phase unwrapping [38]. The reference also demonstrates passive measurement of relative phase between two signals. This is achieved by correlation of simultaneous multiheterodyne measurements with a common local oscillator. This is beneficial in, for example, measuring the relative phase between input signals at two detectors in a sparse synthetic aperture radar system.

### **1.2.6 Photonic Analog-to-Digital Conversion**

Pulses with ultra-low timing jitter from high-repetition rate mode-locked lasers with ultra-low amplitude and phase noise can be utilized to sample an RF waveform and convert the sampled points into a digital code representing the amplitude at well-defined time intervals such that the analog signal can be reconstructed at a receiver. This is done so that the signal may be transmitted in the digital domain with less loss of fidelity. A schematic of photonic sampling for ADC is shown in Figure 1.6. It becomes apparent from the picture, then, that timing jitter on the input pulses will result in sampling the waveform at the wrong point in time, and associating an incorrect amplitude value with that time bin when reconstructing the signal. Similarly, pulse intensity fluctuations into the modulator with a constant transfer function will be mistaken for an erroneous amplitude value of the signal. A review of photonic ADC can be found in reference [42].

Photonics can also assist in sampling short bursts of signals at higher instantaneous frequencies than conventional electronics by utilizing an optical time-stretched architecture [43, 44]. An example of a semiconductor-based HMLL tailored to this application with low noise and low repetition rate, is presented in references [45-47].

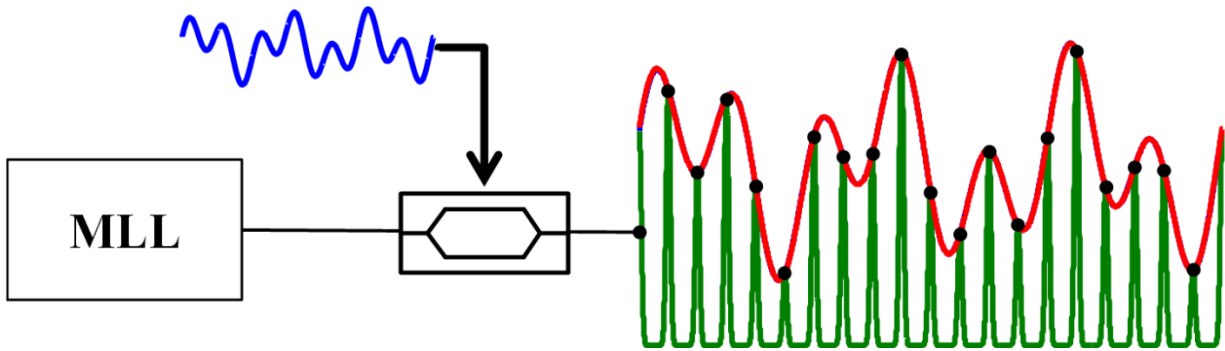


**Figure 1.6** A generalized picture of photonic enabled analog-to-digital conversion wherein mode-locked laser pulses with ultra-low timing jitter and pulse-to-pulse energy fluctuations are modulated using the signal to be converted. Each pulse samples the waveform at a set interval and its amplitude value can then be independently recorded in digital format.

## CHAPTER 2: HARMONICALLY MODE-LOCKED LASERS

In the introduction, several photonic applications were presented which value frequency combs with great stability, narrow optical linewidth, and wide combline spacing and high pulse repetition rates. In order to achieve low optical linewidths ( $\sim 100$ s of kHz) from laser cavities, a long optical storage time is achieved through long fiber cavity lengths. However, high pulse repetition rates are also desirable while maintaining long optical cavities (and therefore a low fundamental cavity frequency,  $\nu_0$ ), necessitating the employment of harmonic mode-locking in laser systems.

### **2.1 Harmonic Mode-Locking Mechanism**

In harmonic mode-locking, a sine wave with frequency equal to an integer multiple of  $\nu_0$  is applied to the mode-locking device,  $\nu_{\text{rep}} = N \cdot \nu_0$ , which is usually a Mach-Zehnder intensity modulator (IM) providing intracavity loss modulation [17, 48]. In the time domain, this means that the modulator transmission window is open several times in one pulse round trip time of the laser, leading to multiple pulses traversing the cavity at any one time. Figure 2.1 shows a representation of pulses within a fundamentally mode-locked cavity (Figure 2.1a) and a HMLL with the same cavity fundamental frequency, and a mode-locking rate of  $3 \cdot \nu_0$  (Figure 2.1b).

In the frequency domain, harmonic mode-locking produces a series of phase locked frequency tones with a spacing equal to the repetition rate ( $\nu_{\text{rep}} = N \cdot \nu_0$ ). However, all cavity modes are allowed to lase, and are also phase locked with modes spaced at the repetition rate. The resultant optical spectrum consists of many cavity mode sets, or supermodes, with spacing  $\nu_{\text{rep}}$ , interleaved with each other. The spacing



between adjacent supermode sets, then, is the fundamental frequency of the cavity,  $\nu_0$ . Figure 2.1c and Figure 2.1d show the frequency domain representation of the optical output of a fundamentally mode-locked laser and a HMLL, both with the same cavity length.

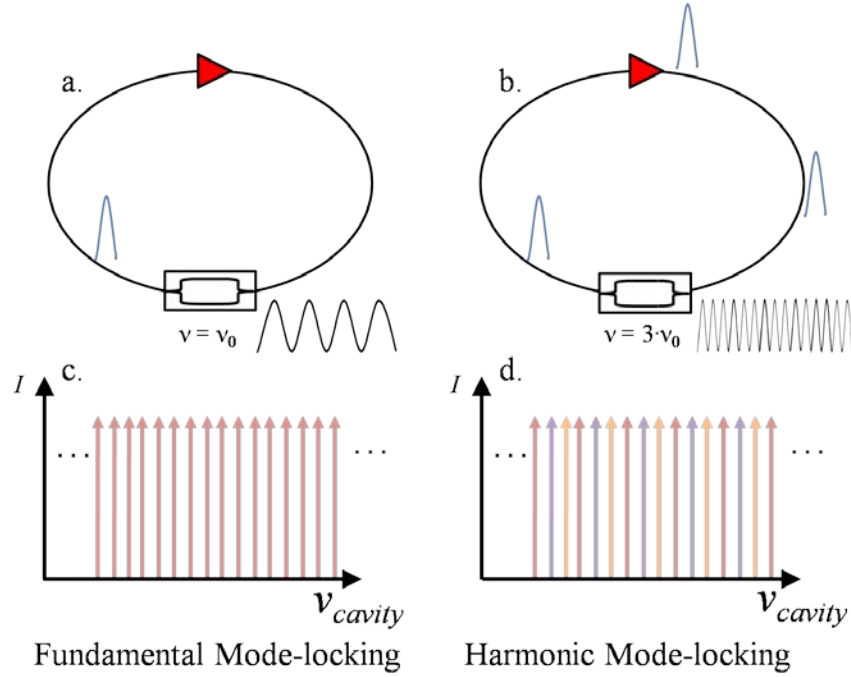


**Figure 2.1** Fundamental (a) versus harmonic (b) mode-locking in the time domain for laser cavities of the same length showing multiple pulses traversing the harmonically mode-locked cavity. Representations of the spectral output in the fundamental (c) and harmonic (d) mode-locking cases showing the presence of optical supermode sets in a HMLL. The Semiconductor Optical Amplifier (SOA) gain media are shown as red triangles and the IMs are shown in the lower part of the cavities, along with the input sine wave to the respective modulators. In this example the HMLL contains three pulses traversing the cavity.

## 2.2 Sources of Noise in Harmonically Mode-Locked Lasers

By its very nature, a laser gain medium can spontaneously emit light which can then be amplified and contribute significantly to the noise of any laser system. In particular, semiconductor gain media have fast electron recombination rates, and laser

noise spectral features due to this effect can occur at frequencies well into the gigahertz [26]. This amplified spontaneous emission (ASE) is also necessary in starting the lasing process, and frequencies of light which are resonant with the cavity constructively interfere and are amplified, regenerating the signal at those frequencies. Long fiber cavities will increase the cavity photon lifetime, narrowing individual resonances and therefore the laser linewidths [49]. This linewidth narrowing has been shown to significantly improve phase and amplitude noise in mode-locked lasers, by reducing the 'knee frequency' of the power spectral density [50], the frequency in a noise power spectral density plot where the noise begins to roll-off precipitously.

One significant noise feature unique to HMLLs is the supermode noise spur (SNS), which occurs due to the beating between adjacent yet uncorrelated laser cavity modes. This lack of correlation is due to the harmonic nature of the intracavity mode-locking mechanism and leads to pulse-to-pulse amplitude fluctuations and timing jitter, both detrimental for the aforementioned applications [50, 51]. This feature is present in RF and noise spectra at multiples of the cavity fundamental frequency up to the repetition rate of the laser system. In order to improve the phase and amplitude noise performance, all supermode sets but one should be suppressed. Two methods are currently employed to achieve this suppression: an intracavity etalon with a free spectral range (FSR) equal to that of the desired repetition rate of the laser [52-55] and single frequency optical injection into the MLL cavity [56-58]. The latter method works by preferentially adding power to one supermode set, while the non-selected supermode sets are deprived due to gain depletion. This work will focus on the latter method.

### CHAPTER 3: INJECTION LOCKING OF OSCILLATORS

Injection locking of an oscillator was first observed by Christian Huygens in 1665. He noticed the synchronization of two pendulum clocks that were hung in close proximity to each other [59, 60]. Since that time, the field of injection locking in oscillators has been more rigorously studied in electrical oscillators [61, 62] and also in laser oscillators [63, 64]. Some basic concepts are summarized here for the benefit of introduction to the research presented.

A laser can be thought of as an amplifying interferometer with regenerative gain. As such, the gain at some frequency offset from a particular optical mode is non-zero. This allows for a weak optical signal coupled into the cavity at a frequency near a resonant optical mode to see gain. When the injected frequency comes close to the center of the resonant cavity mode – within a certain locking range – the cavity begins to lase at the injected frequency, resulting in a ‘frequency pulling’ effect. Figure 3.1 illustrates this frequency range relative to the resonance window of the optical cavity. This effect is due to the injected signal experiencing increasing gain, depriving the previously lasing cavity mode of that gain. In this regime of operation, the laser is said to be *injection locked* [65]. The injected mode now lases exclusively at the injection frequency, maintaining the spectral quality of the injection seed due to gain suppression of other frequencies. In order to maintain this amplification of an off-resonant frequency, the cavity imparts a phase shift on the injected signal, which will be discussed in some detail later. Within the locking range, as depicted in the figure, the amplitude is relatively clamped and roughly equivalent to the sum of the free-running slave laser power and

the injected power. When injecting outside the locking range, both signals will coexist - the master signal may see some gain, and be slightly amplified and may 'pull' the oscillator frequency as described by Razavi [66], but will not overtake the lasing mode, meaning the free-running slave signal magnitude will be mostly unaffected.

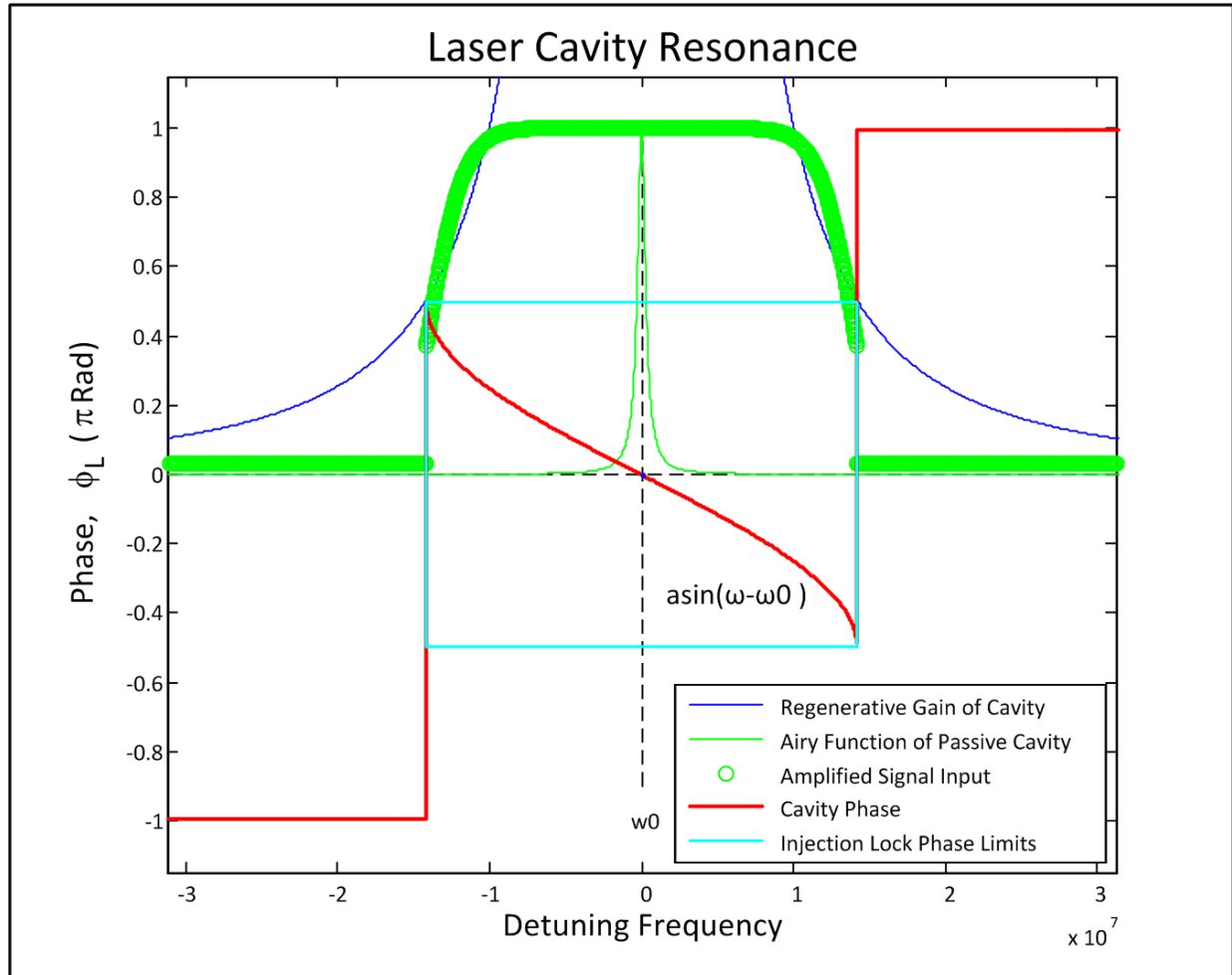


**Figure 3.1.** A slaved cavity resonance and its relevant injection locking properties. The locking range is demonstrated by the vertical cyan lines, as well as the injection lock phase limits of  $\pm \pi/2$ , while the regenerative gain curve of the resonance (solid blue lines) is shown versus optical frequency. Within the locking range, the normalized output power is clamped, approximated by a higher order Gaussian (green circles). The normalized transmission of a passive cavity, defined by the real part of the Airy function, is shown in solid green. The phase shift that an injected tone experiences as it moves across the resonance is shown in red and is shown as an arcsin shape extending from  $\pi/2$  to  $-\pi/2$  over the locking range.

While the phase outside the injection locking range is unknown, it is assumed in this manuscript and in the simulations in later sections to be that of a passive cavity, defined by the Airy function. This assumption is also mitigated by the Airy function having a slowly varying phase at large detuning frequencies away from each resonance.

### **3.1 Applications of Injection Locking**

The injection locking technique is used to synchronize or control the frequency output of a laser [67, 68]. It can be used in power amplifiers to take advantage of high gain in regenerative amplifier systems while maintaining the spectral qualities of a less intense master oscillator. Injection locking is also utilized in optical communication schemes to impart phase-shift keying signals via semiconductor cavities where small changes in the injected current rapidly shift the cavity resonance position relative to a steady injection frequency. This provides advantages in both the necessary peak-to-peak voltage and in modulation frequency, which can reach into the tens of gigahertz.[69-74]. A similar embodiment utilizes the arcsin shaped phase shift characteristic in injection locking (which will be discussed in the next section) within a Mach-Zehnder style modulator for inherently linear intensity modulation [75, 76].

In a multi-wavelength slave laser, injection locking has been shown to lock a mode-locked laser quite effectively, with the output being a set of phase-locked frequency components anchored by the injection frequency [56, 77]. The mode-locking mechanism, whether passive or active, locks the phases of the frequency components,

producing a comb, while injection locking synchronizes the optical frequency to the injection seed frequency, stabilizing the comb.

In HMLLs, injection locking has the added benefit of suppressing the unwanted optical supermodes through gain suppression. This not only stabilizes the optical frequency of the resultant comb output, but also reduces the optical linewidth [78], the relative timing jitter of the laser, as well as the pulse-to-pulse energy fluctuation [57].

### **3.2 Semiconductor Cavity Dynamics of Injection Locking**

As stated earlier, a phase shift is imparted on the injection frequency during injection locking, which is dependent on the detuning frequency from the center of the free-running slave cavity resonance, as depicted in Figure 3.1. Adler first described the behavior of injection locked electrical oscillators and the arcsin shape of the phase imparted on the injection locked output frequency for small injection powers [79]. This phase shift and its resulting affinity for better oscillator injection locking at negative detuning frequencies is described using phasor diagrams [66, 70]. Furthermore, Paciorek [80] explored both the time necessary to achieve injection locking as well as the behavior of the phase across the resonance when the injected power approached that of the free-running slave laser output. In this case, the phase curve can approach arctangent, what one would expect in a cavity with no gain. It is assumed that outside of the locking range, the phase imparted on an injected frequency is also similar to that of the passive cavity, arctangent as a function of detuning frequency, since there is little interaction between the oscillations of the master and free-running slave signals.

Due to fast carrier and gain dynamics in semiconductor lasers, the phase response of a slave laser cavity with semiconductor gain is somewhat more complicated than that of other gain media. Direct electrical pumping creates free carriers (electrons and holes) in the semiconductor material. Due to the availability of these carriers and their affinity for recombination, the index of refraction is heavily dependent on the population of such carriers in the material. Real-time fluctuations in input light intensity will understandably lead to rapid changes in the carrier density and therefore index of refraction. This results in a coupling between intensity and phase noise in semiconductor gain media, first introduced by Henry [81] in 1982. The first indication of this effect was in measuring the linewidth of semiconductor lasers, which did not come close to that predicted by the Schawlow-Townes fundamental limit for laser linewidth [49]. The effect was therefore dubbed the linewidth enhancement factor (LEF), denoted by  $\alpha$  in equations and commonly referred to as the alpha factor.

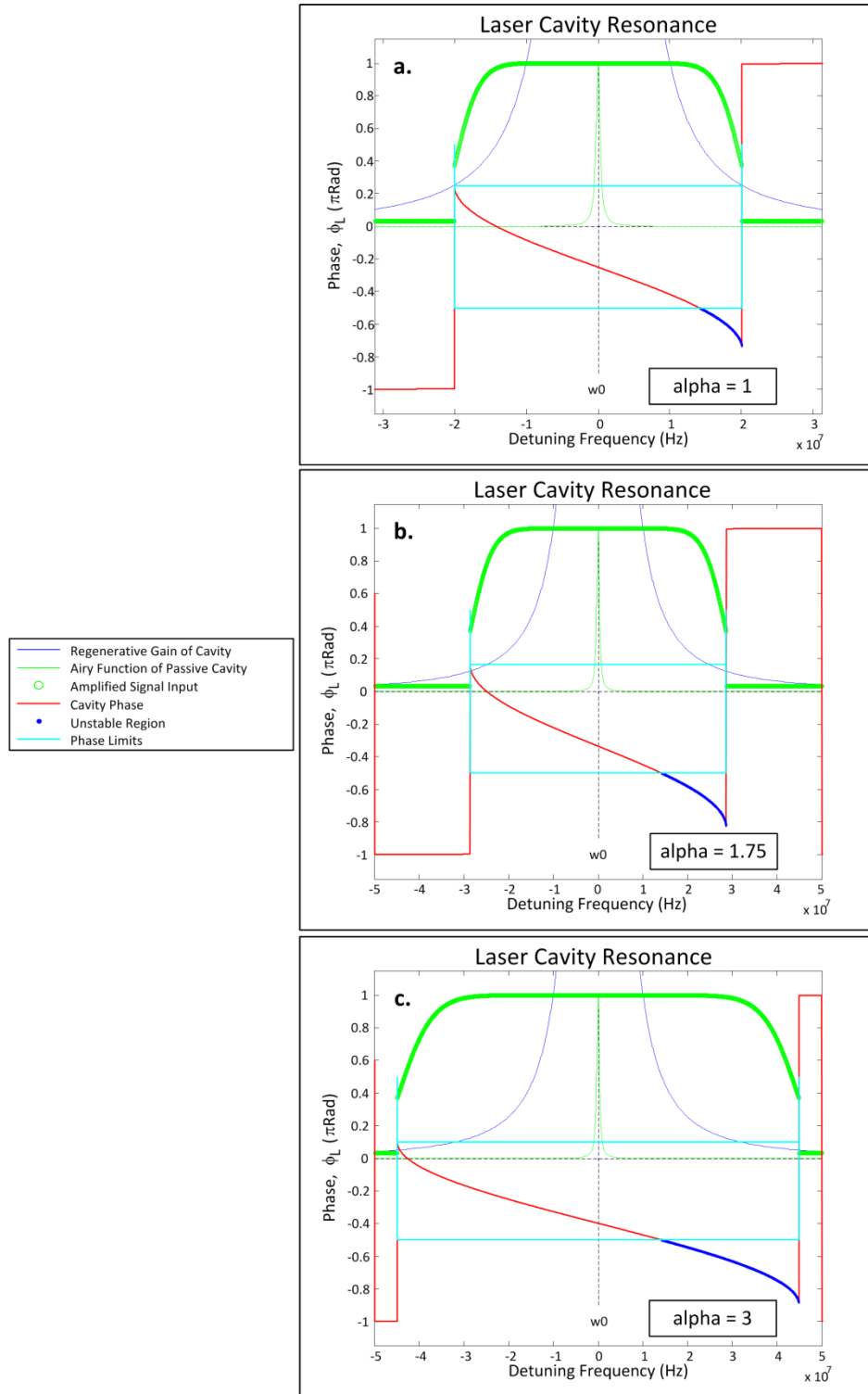


**Figure 3.2.** Semiconductor laser cavity resonances with non-zero  $\alpha$  parameters, shifting resonance phase downward and broadening the injection locking range. Note the difference in frequency scale between figure a) and figures b) and c).



The linewidth enhancement factor effect in semiconductor lasers has since been well studied and several groups have used the model developed by Henry to study various characteristics of injection locking in semiconductor lasers [69-74, 76].

While the LEF was found to increase the natural linewidth of semiconductor lasers by  $(1 + \alpha^2)$ , it also affects the behavior of injection locking in two significant ways. First, the locking range half-width is broadened by the square root of the same factor, resulting in a locking half-width of:

$$\Delta\omega_L = f_D \frac{E_1}{E_0} \sqrt{1 + \alpha^2} \quad (1)$$

where  $\Delta\omega_L$  is the locking half-width,  $f_D$  is the cavity longitudinal mode spacing, and  $E_1/E_0$  is the electric field ratio [82]. This is demonstrated in Figure 3.2a-c for alpha parameters 1, 1.75, and 3. This is in contrast to that of Figure 3.1, where the alpha parameter is set to zero.

Another significant effect of the LEF is a shift in the phase incurred across the injection locking range downward by a factor of  $\text{atan}(\alpha)$ , resulting in the phase across the resonance being defined by the following equation:

$$\varphi_0 = -\text{asin}(\omega - \omega_0) - \text{atan}(\alpha) \quad (2)$$

This is also shown in Figure 3.2a-c for the alpha parameters considered there. As stated earlier, this phase shift is a function of the slaved laser cavity compensating for a lasing mode which is off resonance, and hence the phase at center of the resonance (for zero alpha) is zero. The limit, however, to the ‘tolerance’ of the slaved

laser is when the phase incurred reaches  $\pm \pi/2$ . As shown in the figure, this leads to a portion of the injection locking range with values outside of those limits. In this region, the injection locking dynamics become quite unstable [83]. As the locking range and hence unstable region are dependent on the injection electric field ratio, this region understandably grows with increasing injection power[76, 82]. An intuitive picture of the carrier dynamics involved in this affinity for injection locking at negative detuning frequencies and instability for positively detuned external injection is explained succinctly by Lang in 1982 on page 982 of [83]:

With light injection, the laser output increases in general, and the excited carrier density in the active region decreases correspondingly. Decrease in the carrier density increases the refractive index of the active region which results in the lowering of the cavity resonance frequency. Therefore, the optimum locking can be achieved when the injected light frequency  $\nu$  coincides with the resonance frequency  $\omega$  which is downshifted by the light injection.

A secondary consequence of the LEF affecting both the locking range and stability region is a change in total amplitude of the injection locked frequency across the locking range, as a function of both detuning frequency and injection electric field ratio. While this effect may have significant implications for some injection locking applications [76], such small changes in resultant power are not as important in this work, as the detuning frequency will be stabilized in the final embodiment of the system.

## **CHAPTER 4: LASER CAVITY STABILIZATION VIA POUND-DREVER-HALL METHOD**

### **4.1 Pound-Drever-Hall Cavity Stabilization Overview**

The Pound-Drever-Hall (PDH) method of cavity stabilization is used in many variations to actively long-term stabilize an optical cavity, such as a Fabry-Pérot etalon, relative to a laser frequency or vice versa [84]. Based on previous methods in electrical oscillators [85], the technique exploits the existence of a phase shift across each resonance of the optical cavity, which is, in the classic case, an etalon. By detecting the phase shift of a frequency coupled into the etalon, the frequency offset between the center of the resonance and the injected frequency can be determined, leading to a differential error signal. By actively changing either the injected optical frequency or the absolute position of the etalon cavity resonance, the etalon and injected frequency can be stabilized relative to one another [86].

Continuous wave (CW) injection (CHAPTER 3) will pull the frequency of a laser system when weak injected light is within the locking range of the cavity resonance. Environmental effects cause significant length fluctuations in the long fibers used in external cavity semiconductor lasers. Therefore, a feedback technique becomes necessary to compensate for these fluctuations and keep the injection frequency within the locking range. In the modified PDH method used in this work, the mode-locked laser cavity serves as the optical cavity being probed, as opposed to a passive optical cavity used in the conventional embodiment of the PDH method. A stable, commercially available laser operating at 1550 nm is used as the reference to which the cavity modes

will be locked, while also serving as the injection seed light. The modified PDH method maintains the injection locked state and therefore stabilizes the mode-locked laser output long-term. Similar sideband scheme stabilization has been performed in pulsed lasers [87] and more recently in Q-switched laser designs [88, 89], though the work featured here is the first use for the generation of frequency combs through injection locking of mode-locked oscillators.

Within the locking range, the laser cavity will also impart a phase shift on the injected tone. According to Adler [79], for injection locked oscillating systems with gain, this phase is an arcsin shape, compared to the arctan phase profile of an etalon resonance. The cavity phase shift around a cavity resonance and the locking bandwidth are shown in Figure 3.1.

In order to detect this phase shift, the injection laser, at frequency  $\nu_{inj}$ , is phase modulated to produce sidebands at  $\nu_{inj} \pm \nu_{PM}$  prior to injection into the cavity. Additional injection and lasing of these phase modulation sidebands could result in unwanted spectral components and additional noise in the laser output. Therefore the sidebands are created at such spacing that they will not be resonant with the optical cavity when the injection frequency is within the locking range of a cavity mode. Figure 4.1 shows the relative placement of the phase modulation sidebands when coupled into the harmonically mode-locked cavity.

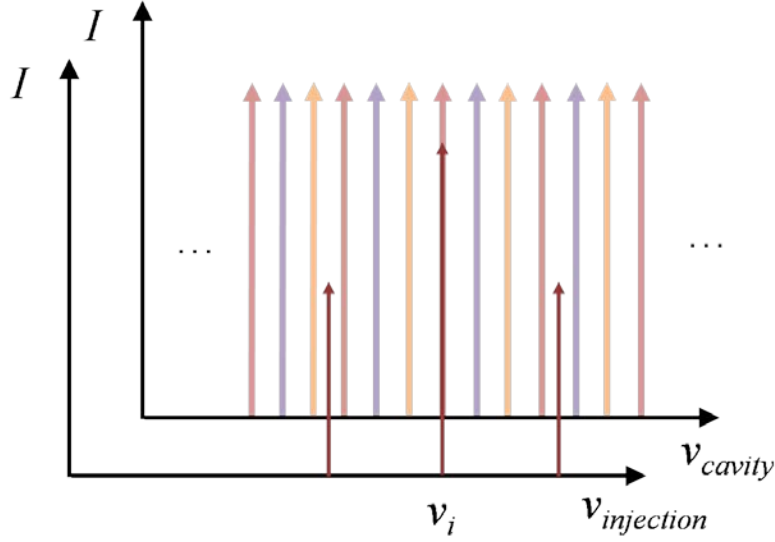


**Figure 4.1.** Representation of the injection seed frequency and phase modulation sidebands injected into a HMLL. Note that the phase modulation sidebands are not resonant with the optical cavity when the injection seed frequency is within a cavity resonance injection locking range.

As the cavity resonance is shifted relative to the three injected tones due to an induced change in optical cavity length, the central tone,  $\nu_{inj}$ , experiences the aforementioned phase shift, while the sidebands do not. By photodetecting the output of the laser with the three tones present in the signal, then mixing the signal with the original phase modulation frequency in quadrature, the sum and difference frequencies are produced. Using a low-pass filter (LPF), the DC signal is isolated and, within the locking range, is a differential signal proportional to the difference between the injected frequency,  $\nu_{inj}$  and the center of the cavity mode resonance,  $\nu_R$ . A proportional-integral controller (PIC) is employed, using the linear portion of the error signal to feed back into an intracavity fiber stretcher, thereby allowing for long-term stabilization of the optical cavity relative to the injection seed frequency.

## **4.2 Modified Pound-Drever-Hall Stabilization Error Signal Simulation**

As will become evident in this and subsequent chapters, the experimentally obtained error signals used to stabilize the injection locked frequency comb source are the result of vastly different phenomena as that of the conventional PDH error signal, starting with an arcsin phase shift across a cavity injection locking range as opposed to arctangent in a passive etalon case. This and other phase and amplitude effects of injection locking are studied and simulated in the following section to further understand the origin of the injection locked modified PDH error signal shape. The PDH error signals for both passive and injection locking cases are simulated in MATLAB simulation software. A version of the programming code can be found in APPENDIX C.

### **4.2.1 Conventional Pound-Drever-Hall Error Signal**

To begin with, a more detailed understanding of the conventional PDH error signal must be presented. As stated in the chapter introduction, PDH stabilization was first proposed by Drever and Hall [84] based on electronic methods by Pound [85]. Yet an excellent review and explanation of the topic is found in a paper by Eric Black [86]. Conventional PDH stabilization exploits the arctangent phase shift across a cavity resonance, shown in Figure 4.2b to detect a frequency detuning between an injected frequency and the resonance center frequency. In order to perform this, PM sidebands are placed on the injected frequency, one sideband having characteristic opposite phase from the other two. This means that when the center, or carrier frequency phase is unchanged, under ideal conditions, photodetection would lead to no signal, as the beating between the positive sideband and the carrier and the negative sideband and

carrier would cancel out each other. These sidebands are placed at a sufficient enough frequency as to lie outside of the cavity resonance while the center frequency is interacting with it, thereby acting as a phase reference in seeing near  $\pm\pi$  phase which is also slowly varying. All three frequencies are injected into the passive optical cavity and the reflection is observed and photodetected. As the carrier frequency sweeps across the resonance, it incurs the arctan phase shift according to the Airy function [86], thereby making the beat signal of all three tones after photodetection nonzero for all nonzero detuning frequencies. At the center of the cavity resonance, zero phase shift and zero amplitude of the injected carrier frequency are seen as it experiences full transmission through the cavity. Furthermore, the sign of the phase incurred flips as it passes from one side of the resonance to the other, and the signal grows as the reflected power of the carrier frequency increases with greater positive or negative detuning. After reflection and photodetection, the phase modified beating at the PM frequency is downconverted to low frequencies (direct current or DC) via mixing with the original PM signal. Typically the two signals are mixed in quadrature, yet different RF phases significantly affect the overall shape of the signal obtained. Higher order terms are low-pass filtered out.

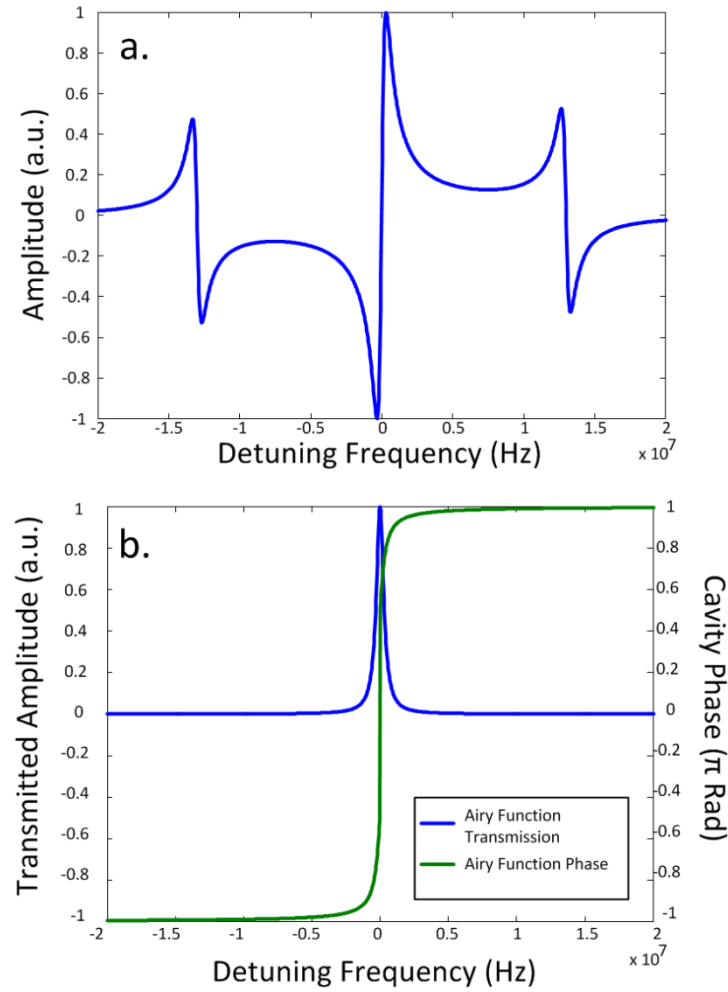


**Figure 4.2.** a) Conventional PDH Error Signal derived from a cavity with  $R = 0.99$  and PM frequency of  $1.13 \times \text{FSR}$ . b) Passive FPE cavity normalized transmission (blue) and phase (green), according to the Airy function governing passive cavity behavior.

As a result of this process, the center region of the conventional PDH error signal results in a differential signal used to stabilize the optical frequency relative to the passive cavity resonance. The entire error signal is shown in Figure 4.2a, where the PM frequency is sufficiently outside of the locking cavity resonance or any other resonance of a periodic optical element such as a Fabry-Pérot Etalon. The large feature in the center of the error signal, as alluded to before, is the result of the carrier frequency



being swept past the cavity resonance. The smaller side features result from the PM sidebands sweeping through the cavity as well, experiencing the same phase shift and beating with the carrier frequency at the PM frequency and being downconverted by the PDH electronics. As the side features are sufficiently distinct from the center feature, yet not completely independent, this type of signal shape is colloquially referred to as the ‘Batman’ error signal for its double spikes just to the left and (reversed) to the right of its center.

#### 4.2.2 Simulated Cavity Resonances

The simulated slaved cavity resonance is similar to that described in CHAPTER 3, yet with multiple resonances separated by an FSR of 100 MHz. In the simulation, an electric field ratio, the ratio of the injected electric field magnitude to that of the naturally occurring electric field in the slave resonance, is specified, as well as a modulation index to determine the power in first order and second order sidebands of the PM signal. Based on these values and equation (1) the locking range is determined for the center resonance as well as two others on either detuning side, as the PM sidebands will injection lock those resonances and hence see similar asin phase shifts, affecting the error signal shape. Equation (2) is used to numerically specify the phase across each resonance. A higher order Gaussian function is used to specify the amplitude response of the cavity within the locking range, such as that in the following equation:

$$y_{Amplitude} = G * e^{\left(-\frac{(\omega-\omega_0)}{\Delta\omega_L}\right)^{Ord}} \quad (3)$$

where  $G$  is the gain of the simulated cavity,  $\omega$  is the detuning frequency,  $\omega_0$  is the cavity resonance center,  $\Delta\omega_L$  is the locking half-width, and  $Ord$  is the Gaussian order. While the conventional PDH relies on the reflection signal of a cavity, which goes to zero at the resonance center, it has been found empirically in the injection locked frequency comb generation system that this is not the case at the ‘reflection’ output used (the previously unused output of the IC), and therefore the amplified transmission from injection locking theory is used in the simulation, which, as stated before, is best approximated by this super-Gaussian function. Various orders between 4 and 60 are used to sharpen the edges of the locking range amplitude. Amplitude and phase characteristics of the relevant optical cavities are shown in Figure 4.3, below.

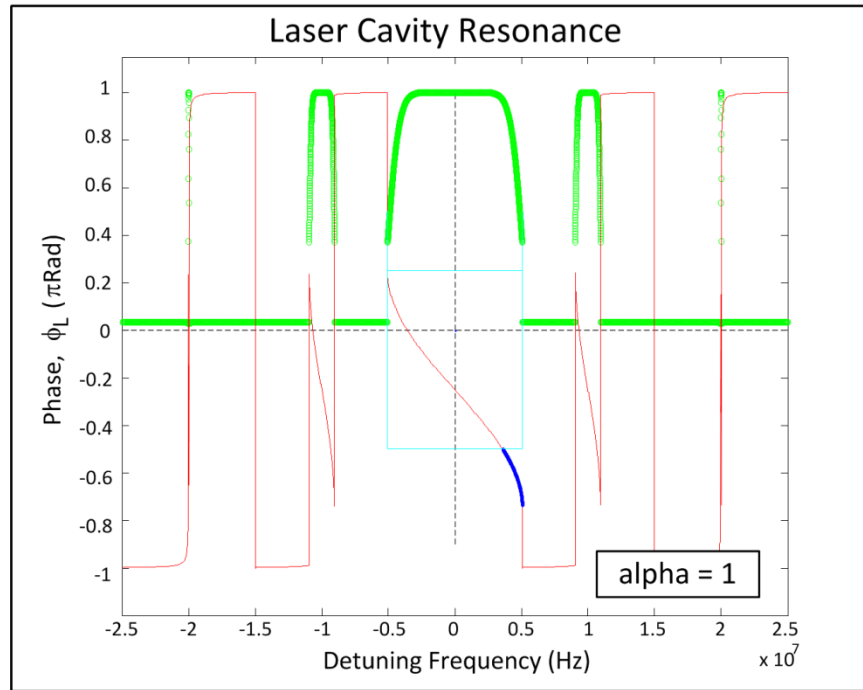


**Figure 4.3.** Cavity amplitude and phase response within injection locking ranges for the center resonance and two nearest neighbor resonances, which PM sidebands interact with while the carrier is near zero detuning.

Outside each resonance, the phase and amplitude are approximated by the passive cavity Airy function:

$$R_{Airy} = \frac{R \cdot e^{\frac{2\pi i(\omega - \omega_0)}{FSR}} - 1}{1 - R^2 \cdot e^{\frac{2\pi i(\omega - \omega_0)}{FSR}}} \quad (4)$$

where R is the mirror reflectivity. While the exact nature of amplitude and phase behavior is not known in this region for the present system, the small amplitudes and slowly varying phases at these large detuning frequencies from each cavity resonance make this an acceptable assumption in the simulation.

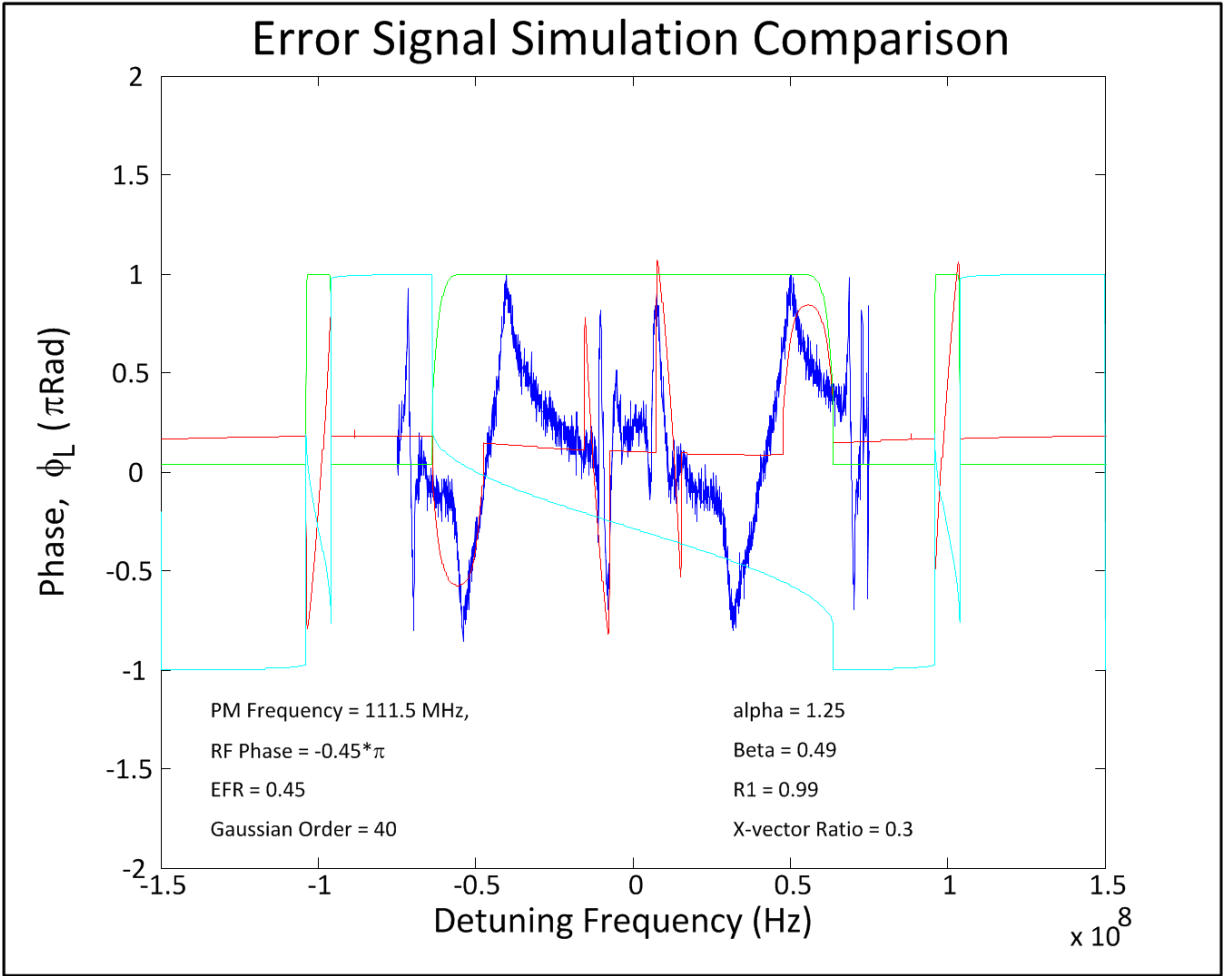
#### 4.2.3 Modified Pound-Drever-Hall Simulations

The simulation then computes PDH error signal for the set of cavities with the injection electric field ratio, phase modulation index, alpha parameter, mirror reflectivity, free spectral range, Gaussian order, and gain parameters specified. Other values in the simulation which are set up to be appropriate fitting parameters for matching simulated signals to experimentally obtained signals are the PM frequency, RF mixing phase in the PDH calculation. It is worth mentioning that previously named injection parameters such as the electric field ratio and phase modulation index which define the amount of injected power, and hence the locking range and phase excursion of each resonance are extremely important in the fitting of the simulated error signals.

Experimentally obtained error signals were chosen to compare to simulation and were plotted with simulated results to obtain a visual fit of the signals while adjusting the aforementioned parameters. The first signal used, shown in Figure 4.4, was chosen for

its clearly discernible features, but is not usable for actual stabilization of the cavity, as a differential feature does not exist at the appropriate locking point. For appropriate context, the same error signal is used for exploration of injection locking qualities in Section 5.2.3. In order to match the simulated and measured error signals, the simulated cavity FSR was maintained at 100 MHz and the experimentally obtained error signal time/frequency scale is adjusted to fit the simulated features that arise, since the measured error signal is arbitrarily based on the magnitude of the cavity sweep at the time it was taken. In addition, the amplitude, vertical offset, and time offset of each signal were adjusted accordingly. Also of note is that the measured error signal is reversed in the horizontal scale, as it was determined that the direction of cavity sweep was such that 'earlier' times on the oscilloscope trace corresponded to positive cavity detuning and 'later' times corresponded to negative frequency detuning from the resonance of concern.

The simulated PM frequency was set at one FSR plus a fraction for ease of comparison and specification in terms of the experimental parameters. Correspondingly, the experimental PM frequency and cavity FSR were noted at ~700 MHz and ~46.9 MHz, respectively, and the ratio calculated between them. The fractional remainder plus one simulation FSR was used as the initializing value for simulating the error signal. The measurement of cavity FSR is based on an estimation between the SNSs in the RF spectrum. As this is representative of the beating of optical cavity modes, which are not evenly spaced across the spectrum, the measurement cannot be exact, and therefore some leeway in the fitting of the PM frequency in the simulation is allowed.



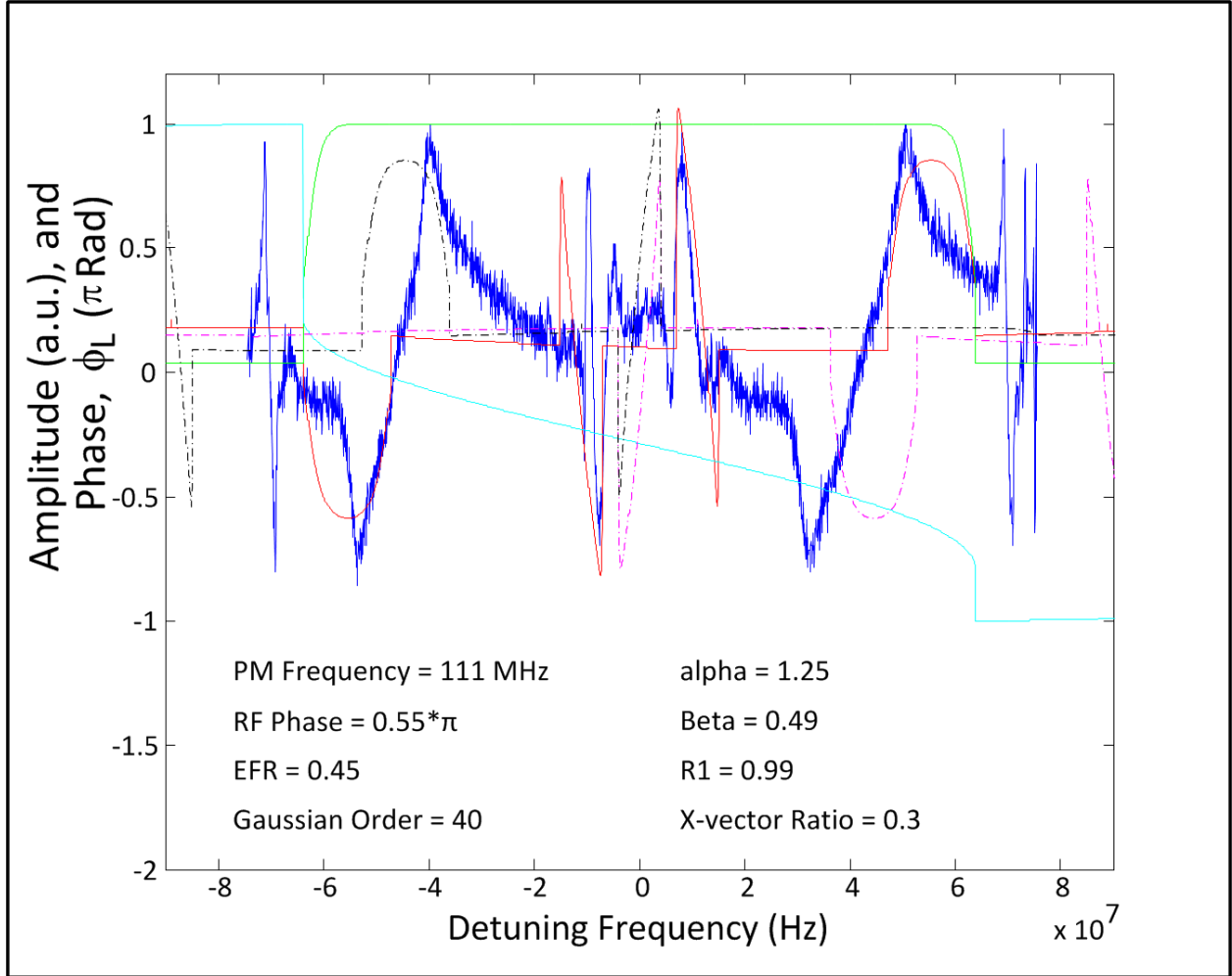
**Figure 4.4.** Comparison of experimentally obtained error signal (blue, PM frequency  $\sim 15.047 \cdot \text{FSR}$ ) to simulated error signal (red) with the parameters shown. The multiple cavity amplitude responses are shown in green, while their phase responses are shown in cyan.

Figure 4.4 shows the best fit for the simulated error signal to the experimentally obtained error signal along with simulation fitting parameters and experimental conditions. As shown, there is good agreement in the middle of the signals, with odd symmetric parabola-like features on either side of the resonance center. This corresponds to the carrier frequency seeing a slowly varying phase in the middle of the shifted asin, while one sideband sees a similar slowly- or non-varying phase while the other first order sideband is quickly swept through the asin phase of its corresponding

resonance. For example, while the carrier is slightly negatively detuned (by exactly the PM frequency from the next positive resonance), it sees the phase displayed at that frequency. Meanwhile the first order negative sideband is far out of its resonance, seeing the slowly varying Airy function phase, and the first order positive sideband is swept through its corresponding resonance, incurring a large and quickly varying phase sweep. The mode beating between the three tones is detected in the PDH scheme, translating into the sharp error signal feature shown at a slight negative detuning from the center. A similar process happens at the same positive detuning frequency, albeit with opposite phase, since the negative sideband has opposite phase as that of the positive from the phase modulation process.

A look at larger detuning frequencies reveals less agreement with the experimental error signal, but some similarities can be identified. For instance, what appears as a single cycle of a triangle waveform with 50% duty cycle appears between subsequent locking signals of the measured error signal. The simulated signal appears to approximate, albeit poorly, half of each of these features, with opposite polarity at positive and negative detuning. However, further analysis reveals that the other polarity of each of these features is contained in the next injection locked resonance's error signal. This is demonstrated in Figure 4.5, where the measured and simulated error signals are plotted, along with a copy of the simulated signal horizontally shifted by one positive FSR and a copy shifted by one negative FSR. Note the position of the largely detuned features relative to one another and, in combination with the original non-

shifted simulated signal, their approximation of the triangle waveform seen in the experimental error signal.



**Figure 4.5.** Comparison of experimentally obtained error signal (blue) to simulated error signal (red), as well as copies of simulated signals shifted by one FSR in the positive detuning direction (pink) and negative detuning direction (black) to illustrate the origin of triangle waveform features between each cavity resonance.

This feature is thought to arise when the carrier is experiencing the rapid phase changes at the edge of the asin curve at the same time that one of the sidebands is experiencing a similar rapid phase shift at the opposite end of the asin curve. Due to the

large injection electric field ratios, the edges of the defined phase within the injection locking bandwidth of the center resonance may not be well approximated, as intimated before. Via Paciorek [80], the edges of the  $\sin$  phase may start to exhibit atan behavior, which could lead to a better approximation of the shape of these largely detuned features.

The necessity of this horizontal shift for visual fitting purposes highlights a weakness of this method of simulating the error signal, namely that it only accounts for the carrier injection locking one particular resonance. As the sweep is applied of the cavity resonance relative to the injection frequency, each resonance it sees is treated as the 'center' resonance for subsequent error signals seen in an oscilloscope trace (not shown in any signals here). When this is considered, it becomes likely that the triangle waveform features could be resulting from independent interleaved features from contiguous error signals. This seems to be confirmed by adjusting the PM frequency and observing each triangle waveform devolve into two separate oppositely-moving features.

A further revelation of these interleaved waveforms and the calculated locking range obtained through the error signal comparisons is that the locking ranges for subsequent resonances are overlapping. This implies that, at the electric field ratios considered, the laser is always within the locking range of at least one cavity resonance, and is therefore always 'injection locked'. However, only certain positions near the center of the unlocked resonance provide sufficient frequency comb bandwidth by



injection locking many modes across the lasing bandwidth via the mode-locking mechanism and spaced at the repetition rate of the HMLL.

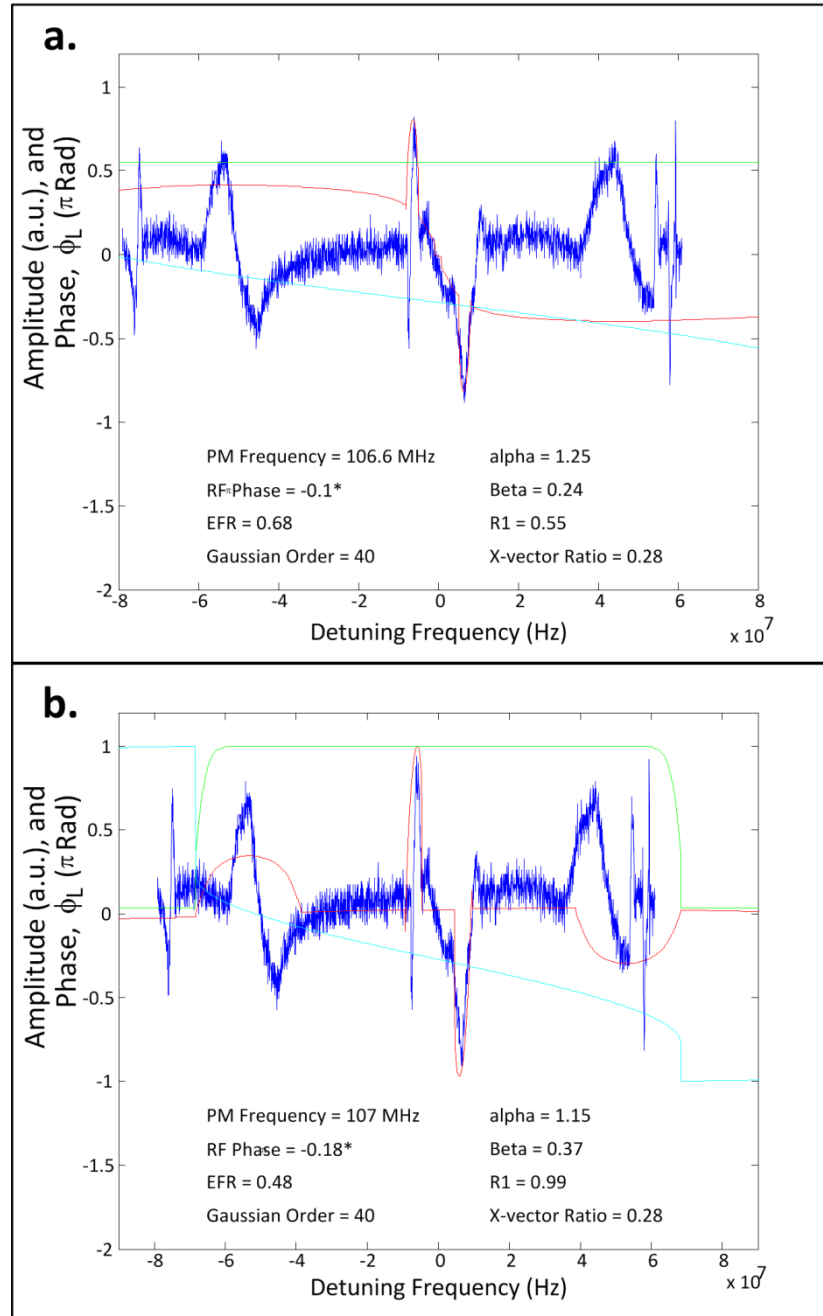


**Figure 4.6.** Comparison of realistic locking signal to simulation results. Visual fitting was able to closely approximate either a) the center features including the differential features used for feedback stabilization, or b) the overall shape of the error signal.

Since the error signal used was configured so as to make it unsuitable for realistic PIC locking (i.e. with a differential signal at the appropriate locking region of the error signal), a second error signal was compared to simulation, and fitting parameters adjusted to approximate the error signal. The result is shown in Figure 4.6a, with good agreement in the center, including both sharp features at small detuning frequencies, as well as the differential portion used to lock the laser, highlighted in the figure, and the slight 'hesitation' feature at zero detuning. However, the largely detuned features show less visual agreement than the previous example. Adjusting the parameters for a better overall fit, however, did not account for the differential signal near zero detuning frequency which is used for feedback stabilization, as shown in Figure 4.6b.

## CHAPTER 5: CW INJECTION LOCKING OF AN ACTIVELY MODE-LOCKED LASER

As an embodiment and test of the principles outlined in the previous chapters, a laser system was constructed to generate a GHz-spaced frequency comb output using an injection locked HMLL. For this particular system, the comb spacing desired was nominally 2.5 GHz.

### 5.1 Actively Mode-Locked Injection Locked Laser Setup

Figure 5.1 shows the setup of the laser system for the injection locking of an actively mode-locked laser with the modified PDH feedback loop [90, 91]. The cavity consists of a semiconductor optical amplifier (SOA) within a fiberized ring cavity. A Mach-Zehnder intensity modulator (IM) is used for mode-locking at 2.5 GHz, the 42<sup>nd</sup> harmonic of the cavity fundamental frequency, ~60 MHz.

A fiber phase shifter is placed in the cavity for fine adjustment of the cavity length, while a free-space variable optical delay allows for course adjustment of the cavity length to directly control the repetition rate. A bandpass filter is utilized to force lasing at the injection seed frequency as well as an isolator to ensure unidirectional light propagation. Polarization controllers and dispersion compensating fiber are included for additional control of the spectral output, and an injection coupler and output coupler are used to couple light in and out of the cavity. The laser system produces 2-3 mW average power with an injection locked pulsewidth of ~22 ps FWHM. The optical cavity is also enclosed within a thermally insulated box to minimize the effects of environmental fluctuations on the cavity length.



employed to control the polarization of the injected light, which is ultimately coupled into the cavity using a 90/10 ratio fiber coupler. A signal near 500 MHz is used for the phase modulation in the PDH feedback scheme, though not at a rate that will produce cavity resonant sidebands.

## **5.2 Laser Preparation for Frequency Comb Generation**

The injection locked frequency comb source is created out of a harmonically mode-locked laser. Therefore, the first operational step in creating the frequency comb is to mode-lock the laser. While specific parameters for mode-locking may be found in other sections, the information is repeated here for a more complete picture of the frequency comb generation procedure.

### **5.2.1 Laser Parameters for Effective Injection Locking**

The actively mode-locked laser system is constructed according to the diagram shown in Figure 5.1 for Pound Drever Hall stabilization and Figure 6.1 for polarization spectroscopy stabilization. Despite the long fiber cavity, and its appearance in Figure 5.1, dispersion compensation has been found experimentally thus far to be detrimental to frequency comb generation through the injection locking method. The cavity fundamental frequency,  $f_0$ , for the examples shown in this section is ~47 MHz (note that this parameter, as well as the repetition rate, may be different throughout this dissertation, and will be specified each time). The semiconductor optical amplifier used is operated with 500 mA of injection current, near the maximum operating current for the device. Voltage is applied to the intracavity IM at the experimentally determined point in the middle of the linear transmission curve, in most cases near 6.35 V. An RF signal of

~20 dBm is then applied to the IM at the desired mode-locking frequency, 10.250984 GHz, a harmonic of  $f_0$ . Due to slight dispersion across the cavity within the SOA bandwidth, slight detuning of the applied frequency from the exact harmonic of  $f_0$  shifts the center wavelength of the mode-locked optical spectrum. Since this cavity dispersion experiences a small change with temperature, the internal temperature of the environmentally isolated laser box can also be adjusted to tune the operating wavelength and consequently must be stable for long term stable injection-locking operation.

### 5.2.2 Injection Locking Procedure

The optical spectrum of a harmonically mode-locked semiconductor laser without dispersion control is shown in Figure 5.2. It contains (ignoring the strong injection power present at 1549 nm) a sharp peak on the long wavelength side of the spectrum with a rolloff extending towards shorter wavelengths due to pulse chirp and semiconductor gain dynamics [92]. Prior to frequency comb generation by injection locking, the mode-locked spectrum must be tuned, via the aforementioned methods, such that the injection frequency on the shorter wavelength side of the spectrum can see enough gain to effectively seed the laser across the entire spectrum, approximately 1/3 of the total bandwidth away from the short wavelength edge, as demonstrated in the figure.

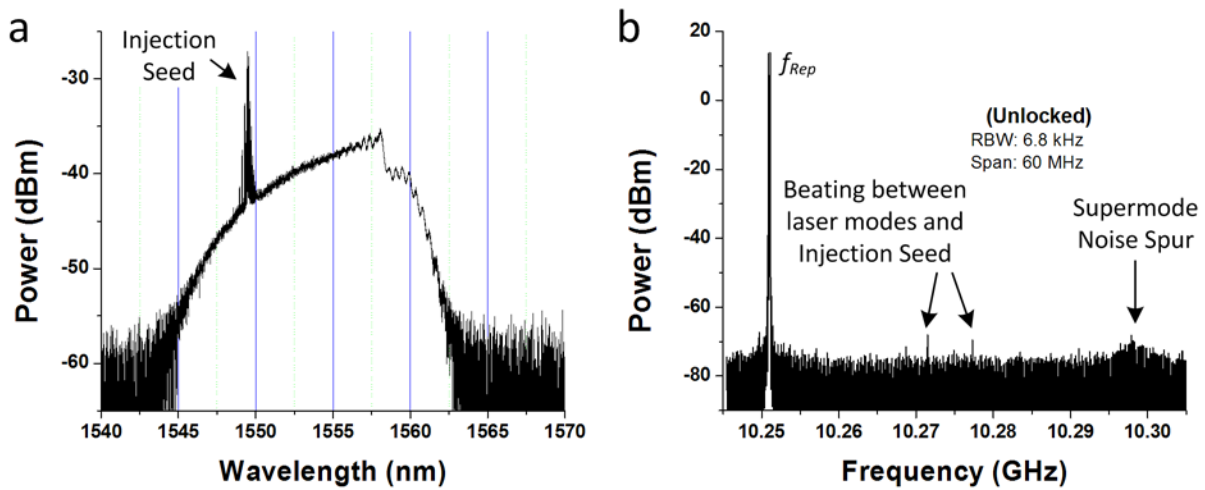


**Figure 5.2.** a) Optical and b) Photodetected RF spectra of a harmonically mode-locked laser with injection from the single frequency injection laser, but not yet injection-locked.

Figure 5.2b shows the photodetected RF spectrum of the unlocked mode-locked laser, with the repetition frequency shown as a near delta function on the left side. The mound of noise on the right protruding above the noise floor is a SNS corresponding to the next harmonic of  $f_0$ , which should be suppressed into the noise floor when the system is injection locked. Viewing the RF spectrum in this way is quite helpful during operation to verify proper mode-locking and as a more responsive method to verify that injection locking has occurred, as the optical spectrum analyzer typically has a much slower response time. Note the existence in Figure 5.2b of two small tones between  $f_{rep}$  and the SNS shown. These tones are RF beat notes between the injection frequency and modes in the laser spectrum. As the cavity length is tuned via the fiber stretcher, the cavity modes shift until one is close enough in frequency to the injection seed for injection locking to occur. As this happens, the small RF beat notes will approach the SNS and the  $f_{rep}$  tone on the RF spectrum. Two complementary beat notes will

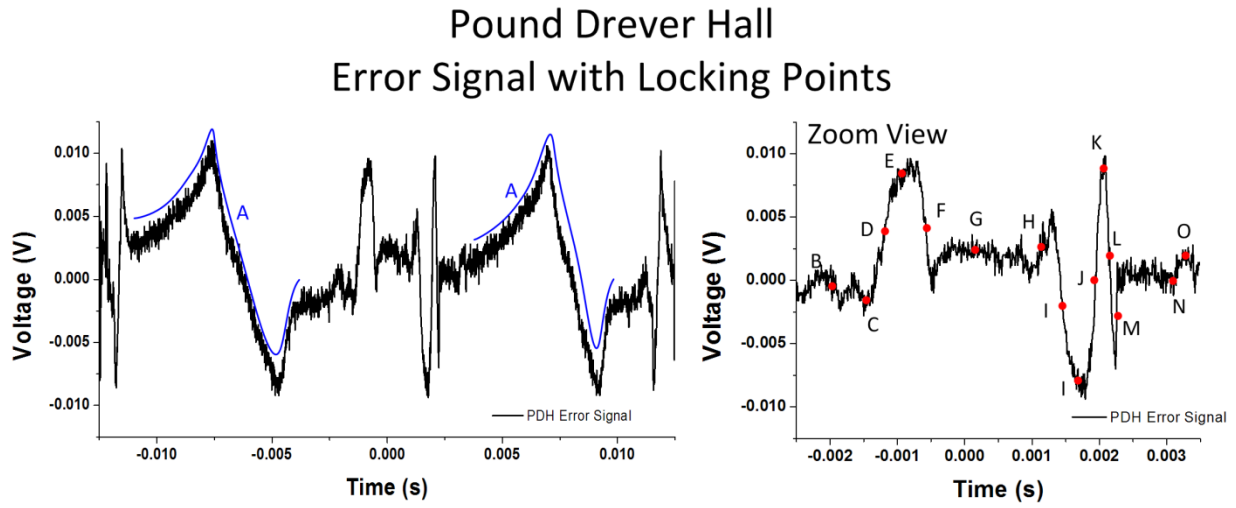
converge on both the SNS and the  $f_{\text{rep}}$  tone from either side of them until the SNS is suppressed and the laser is injection locked.

### 5.2.3 Pound-Drever-Hall Stabilization Error Signal Locking Exploration

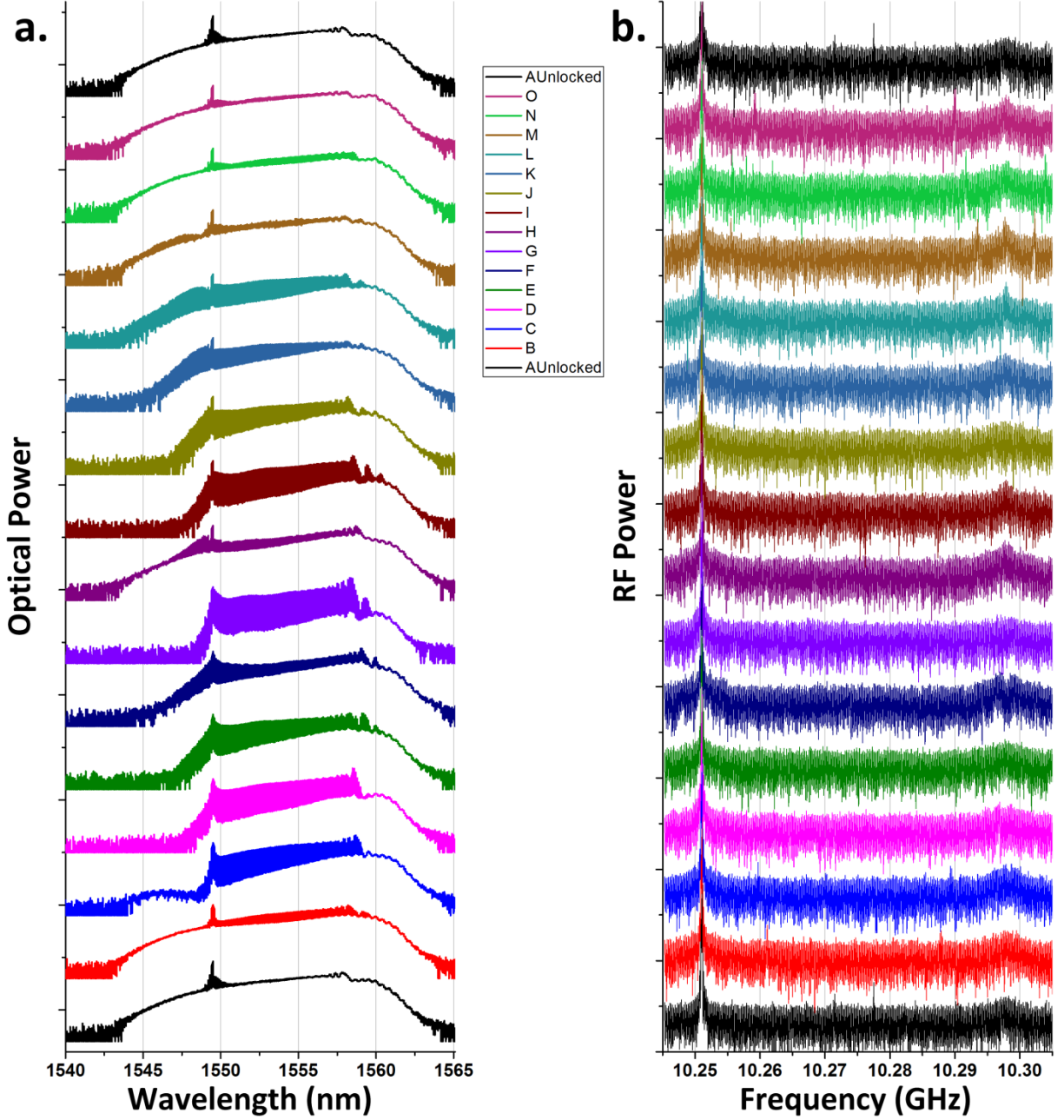
First locking of the system using the modified PDH scheme was performed empirically. In order to further understand the various PDH error signal shapes, and to determine appropriate procedure of locking via the PDH error signal for long-term stabilization of the injection locked frequency comb system, the optical and RF spectra were recorded at various points along an error signal. Experimentally, a sweep was applied to the cavity length (using the intra-cavity piezoelectric fiber stretcher, or fiber phase shifter, FPS) to visualize the error signal, and then the sweep was attenuated in order to fixate on a particular point along the curve while spectra were recorded. While the error signal used, shown in Figure 5.3, is not appropriate for locking the system it was chosen because the central and salient features were well understood at the time of the experiment, as described in a previous section. Many subtle features exist near the center of the locking resonance and were probed for injection locking characteristics. Figure 5.3 shows a detail view of the central features. Optical and RF Spectra results are shown in Figure 5.4. Optimal injection locking occurs at point ‘G,’ near the center between the two prominent up- and down- checkmark curves of Figure 5.3, demonstrated by the optical bandwidth and fringe visibility of the injection locked comb structure, as well as the suppression of the SNS shown near 10.3 GHz in the RF spectra. A reduction in the quality of injection locking is shown for the surrounding points (‘F’ and ‘H’), while a resurgence in fringe visibility is exhibited for other locking



points on or around the aforementioned up- and down- features. As these locations are where a phase modulation sideband from the PDH scheme is sweeping through a neighboring resonance, these regions of quasi-injection locking and comb generation are likely due to injection locking of the sidebands into said resonance.



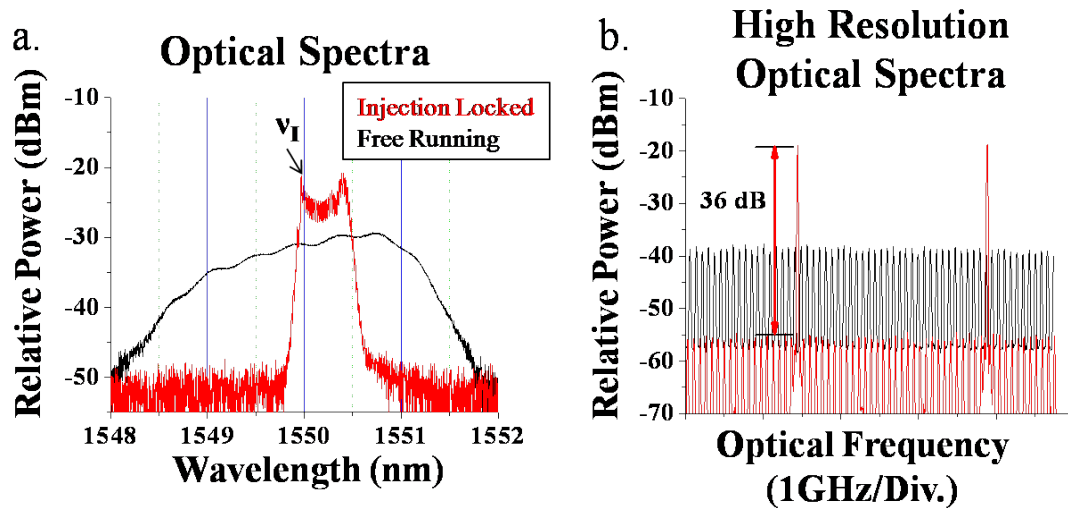
**Figure 5.3.** Error Signal for laser system stabilization via PDH. The system was temporarily stabilized at the labeled points shown for observation of the locking characteristics, shown in the following figure.



**Figure 5.4.** a) Optical (0.05 nm resolution) and b) RF (60 MHz span; 6.8 kHz RBW) spectral observations of injection locking at various points along the PDH error signal, shown in the previous figure. Optimal injection locking was found at point 'G' (light purple). Other injection points of decent quality (points 'D' and 'I') occur where PM sidebands are aligned with other cavity resonances and therefore injection lock them.

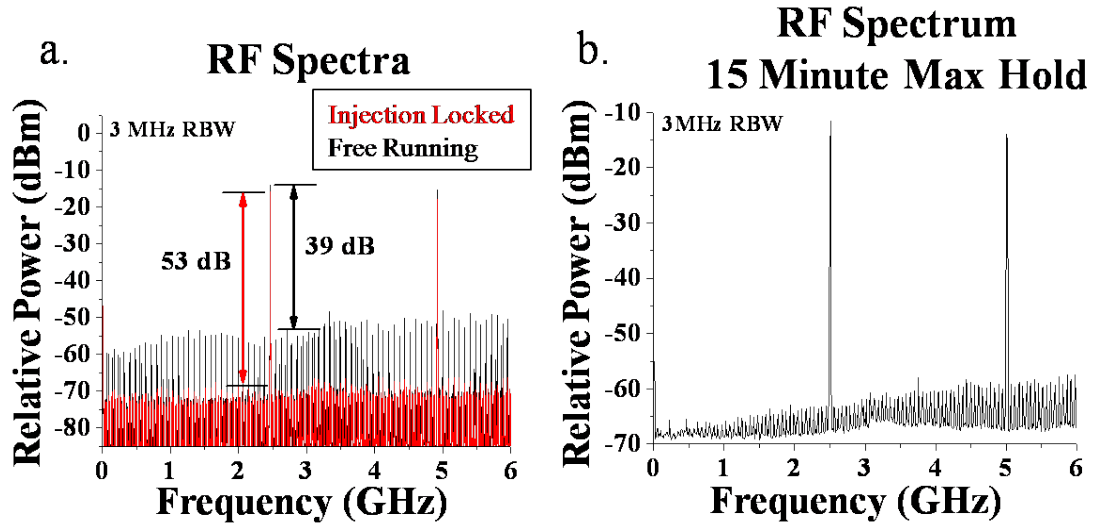
### 5.3 Actively mode-locked injection locked laser results

Figure 5.5a shows the optical spectra of the free running (black, mode-locked but non-injection locked), and injection locked (red) laser system. Before injection, the mode-locked laser bandwidth is near 5 nm, corresponding to the transmission of the intracavity BPF. The injection tone is noted on the figure. After injection, the comb visibility with 2.5 GHz spacing has increased due to the suppression of all other supermode sets in the output spectrum. The bandwidth of the injected spectrum is approximately 0.5 nm, corresponding to around 25 comb lines with 100  $\mu$ W per comb line. The optical sidemode suppression can be seen in Figure 5.5b, a high resolution view of a portion of the optical spectrum taken using a high-resolution optical spectrum analyzer. The optical sidemode suppression of all other non-selected supermodes in the injection locked case is 36 dB.



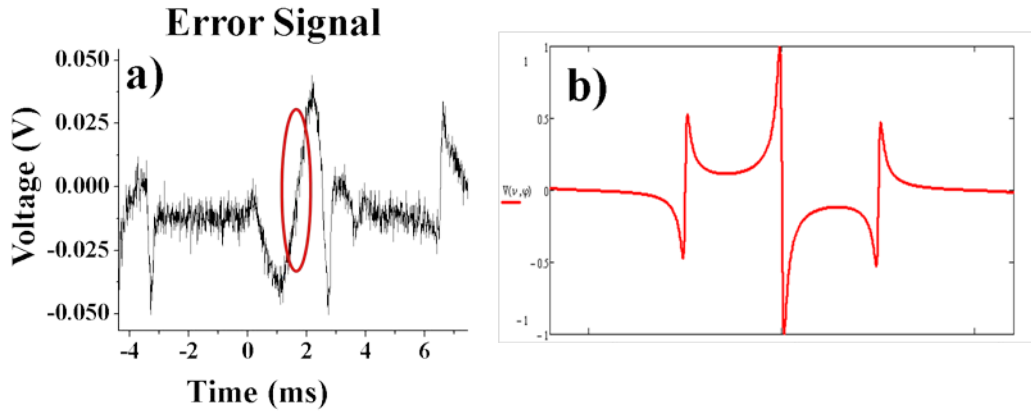
**Figure 5.5.** Optical spectra of the actively mode-locked laser free running, or without optical injection (black) and injection locked (red). (a) shows the entire mode-locked spectrum, while (b) is a high resolution view of a portion of the spectra. Two tones of the injection selected supermode are visible with a spacing of 2.5 GHz, while 36 dB suppression of the unselected supermodes is shown.

Figure 5.6a shows the directly detected RF spectrum of the laser output in the free running and injection locked cases. The photodetected output shows a strong beat note at the repetition rate of the laser, 2.5 GHz, as well as harmonics of this tone from the strong correlation between frequency components within each supermode. In the free running case, RF tones are seen at the cavity fundamental frequency (60 MHz) and its harmonics, corresponding to beating between each longitudinal mode of the laser, or adjacent supermode set beating. In the injection locked case, these SNSs are suppressed by 14 dB, as shown in Figure 5.6a. When employed, the modified PDH feedback loop keeps the laser injection locked long-term. This can be shown by the long-term suppression of the SNSs in the photodetected RF spectrum of the laser output. Figure 5.6b shows this suppression for 15 minutes using the Max Hold feature of an RF Spectrum Analyzer. Injection lock has been seen for greater than an hour and is limited by the dynamic range of the fiber phase shifter used to tune the cavity length.



**Figure 5.6.** RF spectra of the laser system in the free running (black) and injection locked (red) case. (a) shows the suppression of RF supermode noise spurs by 14 dB due to optical injection. In (b) the suppression of RF supermode noise spurs for fifteen minutes is shown while the modified PDH feedback loop is in use.

In the interest of characterization of the laser system, the cavity resonance is swept past the injection seed frequency as the error signal is monitored. A resulting waveform is shown in Figure 5.7a. As explained above, the resulting error signal for this case differs greatly from the classic PDH error signal, shown in Figure 5.7b. This is explained in great detail in CHAPTER 4.



**Figure 5.7.** (a) Modified Pound-Drever-Hall error signal of the injection locked actively mode-locked laser cavity with CW injection. The discriminant portion of the error signal used for locking the cavity is highlighted in red. (b) Ideal Pound-Drever-Hall error signal shape for a passive cavity such as an etalon. The discriminant is the sharp vertical line in the center feature of the signal.

A look at the noise characteristics of the free running and injection locked operation of the laser reveals an improvement in both the timing jitter and pulse-to-pulse energy fluctuation of the laser. Figure 5.8 and Figure 5.9 show the close-in residual phase noise and amplitude noise of the laser system, respectively, normalized to 1 Hz versus offset frequency. The timing jitter and pulse-to-pulse energy fluctuation from 1 Hz to 100 MHz is the respective integrated noise [31, 93]. The free running timing jitter is calculated to be 427 fs. The timing jitter is significantly reduced by optical injection, to 121 fs. Amplitude noise is also measured over the same offset frequency range, and pulse-to-pulse energy fluctuation is found to be 0.61% for the free-running case and reduced to 0.24% via optical injection.

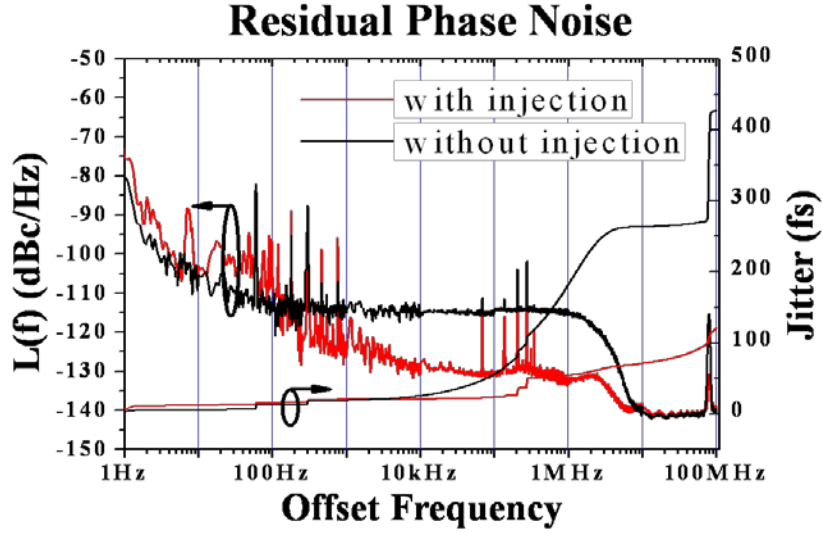


**Figure 5.8.** Residual phase noise of the laser in free running and injection locked states. In free running operation, an integrated timing jitter from 1 Hz to 100 MHz of 427 fs was measured. Optical injection reduced the integrated jitter to 121 fs.

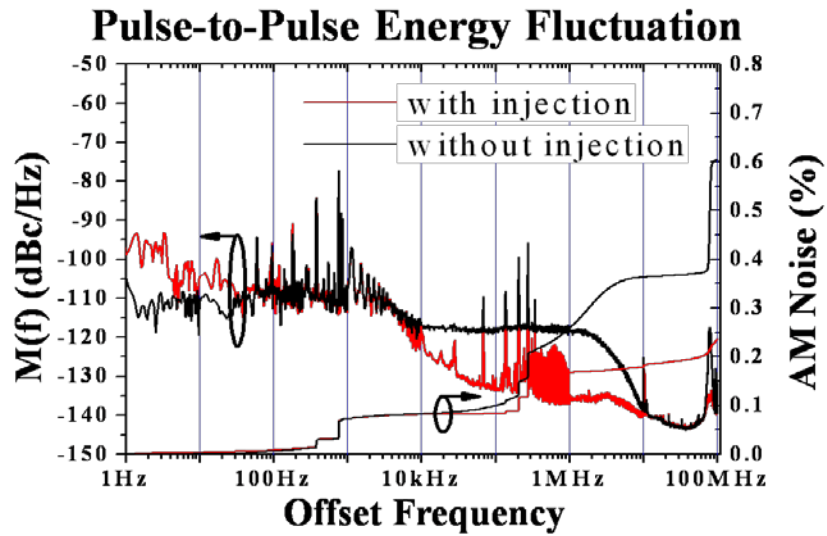


**Figure 5.9.** Pulse-to-pulse energy fluctuation, or amplitude noise of the laser in free running and injection locked states. In free running operation, integrated AM noise from 1 Hz to 100 MHz of 0.61% was measured. Optical injection reduced this integrated AM noise to 0.24%.

## **CHAPTER 6: LASER CAVITY STABILIZATION VIA POLARIZATION SPECTROSCOPY**

The modified Pound-Drever-Hall (PDH) scheme which has been used thus far to stabilize the laser cavity resonance to the injection frequency requires phase modulation of the injection signal before injection [90]. The PM sidebands are inherently injected into the cavity and are then modulated at the repetition rate, producing unwanted carrier sidebands in RF and optical spectra. To reduce these unwanted sidebands a new stabilization method is considered, wherein long-term cavity stabilization is performed with a polarization spectroscopy scheme first put forth by Hänsch and Couillaud (HC) [94]. For that reason, the terms polarization spectroscopy and HC method will be interchangeable within this document. While the PDH method does provide a factor of two improvement in the error signal slope comparatively [89], the HC method features a significant reduction in the complexity of the system while eliminating unwanted optical and RF sidebands inherent in the previous modified PDH stabilization.

Polarization spectroscopy achieves locking to a passive, polarization discriminating cavity such that one polarization state is resonant with and used to probe the cavity, while the orthogonal polarization is fully reflected, and acts as a phase reference. The technique has also been shown in birefringent cavities, utilizing the offset resonances of the orthogonal polarization at the desired locking frequency region to provide a directly reflected beam as a phase reference [95]. While polarization spectroscopy has been previously shown in single frequency laser systems [96], to the authors' knowledge, this is the first use in an injection locked harmonically mode-locked



system for the generation and stabilization of an optical frequency comb, important for multiheterodyne detection. This work was presented at the 2012 Conference on Lasers and Electro-Optics [97].

## 6.1 Polarization Spectroscopy: Introduction and Experimental Setup

A schematic of the laser system is shown in Figure 6.1. The laser consists of a commercially available semiconductor optical amplifier (SOA) in an external fiber ring cavity. A Mach-Zehnder style intensity modulator (IM) is driven at the desired pulse repetition rate and frequency comb spacing, 10.24 GHz with ~20 dBm of RF power. Two couplers are included for a laser output and injection input, in addition to multiple polarization controllers (PC) and an optical isolator (ISO) to ensure unidirectional operation. A CW narrow linewidth (~1 kHz) laser at 1550 nm is used as the injection source, while injection power is controlled using a variable optical attenuator (VOA).

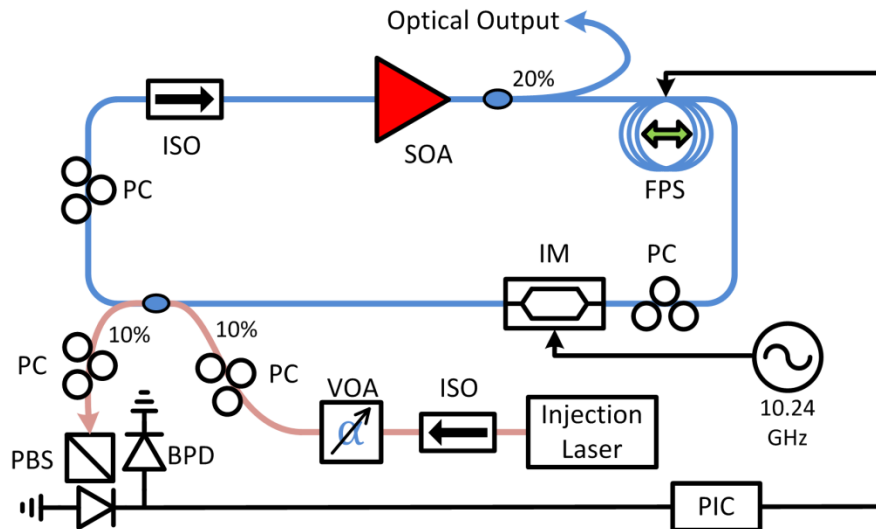


**Figure 6.1.** Schematic of injection locked HMLL with long-term stabilization via polarization spectroscopy.

The injection polarization is adjusted for optimal injection locking. The SOA and IM both act as polarization discriminating devices and the injected tone experiences a phase shift while interacting with the cavity. The detection apparatus is placed at the injection coupler reflection port, where the output signal consists of the preferred injection polarization as well as the orthogonal polarization directly reflected from the cavity. A PC is used to rotate both signals such that they interfere in both outputs of a fiberized polarization beam splitter (PBS). A balanced photodetector (BPD) takes the difference between the two signals to produce an error signal.

#### **6.1.1 Polarization Spectroscopy Error Signal Locking Exploration**

Locking of the injection locked frequency comb generation system via polarization spectroscopy was also performed empirically. Accordingly, a similar experiment as that described in Section 5.2.3 was performed to explore the injection locking qualities at various points along the HC error signal. The error signal derived by sweeping the cavity length, and hence a cavity resonance, past the semi-stable injection seed frequency is shown in Figure 6.2 and is considerably simpler than that derived via PDH stabilization (Figure 5.3). As before, the external cavity sweep was attenuated to ‘zoom into’ a particular point on the HC error signal. Optical and RF spectra were taken at these various points for the same approximate CW injection power as before, ~20 microwatts. The results are shown in Figure 6.3a and Figure 6.3b.

Best injection locking on first pass was found at points ‘E’ (green) and ‘F’ (light purple), shown by high fringe visibility in the optical spectrum, which signifies the existence of a wide, 10 GHz spaced comb structure, and by excellent suppression of

the SNS shown on the right of the RF spectra. These qualities were then optimized and the error signal position recorded at point 'K' (dark blue), hence it's displacement in the alphabetical order. Some allowance for feedback excursion on either side of the locking point on the error signal is necessary for effective stabilization of the system. Therefore, the most effective locking point of the three is at point 'E.' Unlike that of the PDH error signal, a clear roll-off in injection locked comb quality on either side of the optimal locking region is shown. This further highlights an advantage of the HC method over the previous modified PDH method, namely the preclusion of injection locking by the PM sidebands inherent in that method.

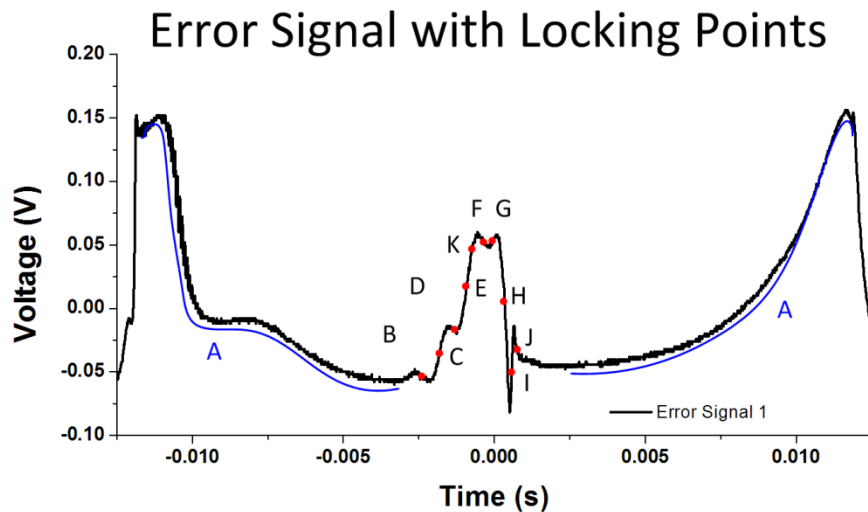


**Figure 6.2.** Error Signal for laser system stabilization via polarization spectroscopy. The system was temporarily stabilized at the labeled points shown for observation of the locking characteristics, shown in the following figure.

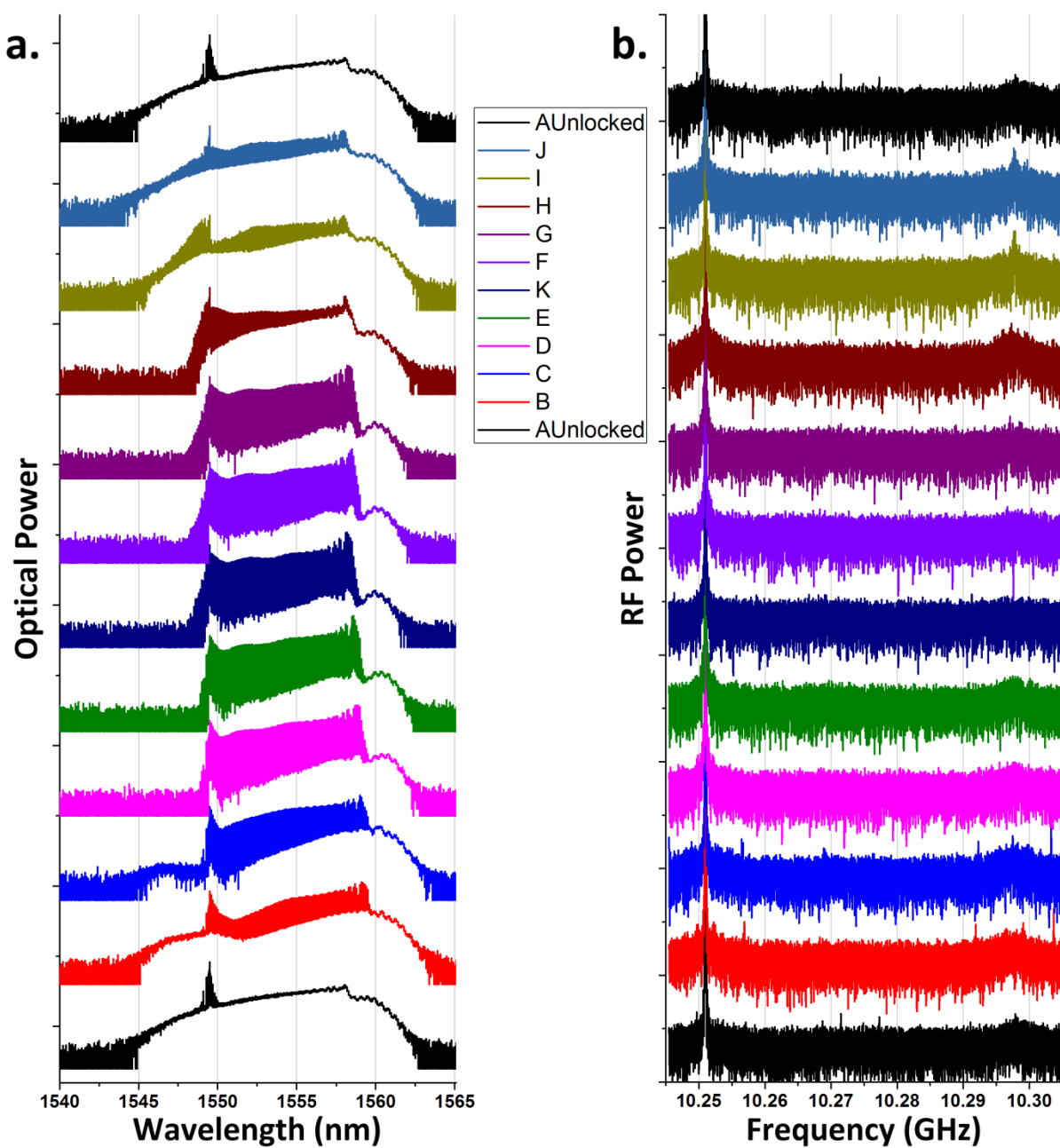


**Figure 6.3.** a) Optical (0.05 nm resolution) and b) RF (60 MHz span; 6.8 kHz RBW) spectral observations of injection locking at various points along the HC error signal, shown in the previous figure. Optimal injection locking was found at point 'K' (dark blue), while best error signal locking was found at point 'E'.

## **6.2 Polarization Spectroscopy Stabilization Error Signal Simulation**

In order to further understand the mechanics of the polarization spectroscopy error signal, the cavity parameters outlined in Section 3.2 are utilized in the simulation of an error signal derived from polarization spectroscopy.

### **6.2.1 Simulated Cavity Resonances**

As explained above, the HC technique exploits the polarization selectivity or birefringence in a cavity being probed. One polarization is resonant and sees a corresponding phase shift while the orthogonal polarization is reflected. In the simulation, one polarization, dubbed the ‘parallel’ polarization, is considered to be resonant with the cavity, and therefore sees gain. The cavity amplitude and phase response is shown in Figure 6.4, and is calculated in the same way as that described in Sections 3.2 and 4.2.2, above. As the interaction of multiple cavity resonances is not necessary in HC due to the lack of PM sidebands, those cavities, while being redefined in the same way in this simulation as that of the zero-detuned resonance, are ultimately inconsequential. In order to maintain uniformity and flexibility to assume birefringence, the orthogonal polarization (‘perpendicular’) is defined as an Airy reflection function, where center resonance is detuned from that of the ‘parallel’ beam. The HC error signal is then calculated via the intensity equation in reference [94]:

$$Error = \frac{1}{2}c\epsilon * \left[ \left| \frac{1}{2} \left( E_{par}^{(r)} + iE_{perp}^{(r)} \right) \right|^2 - \left| \frac{1}{2} \left( E_{par}^{(r)} - iE_{perp}^{(r)} \right) \right|^2 \right] \quad (5)$$

where  $c$  is the speed of light,  $\epsilon$  is the absolute permittivity, and the remaining are the reflected ‘parallel’ and ‘perpendicular’ electric fields of the injected signal.

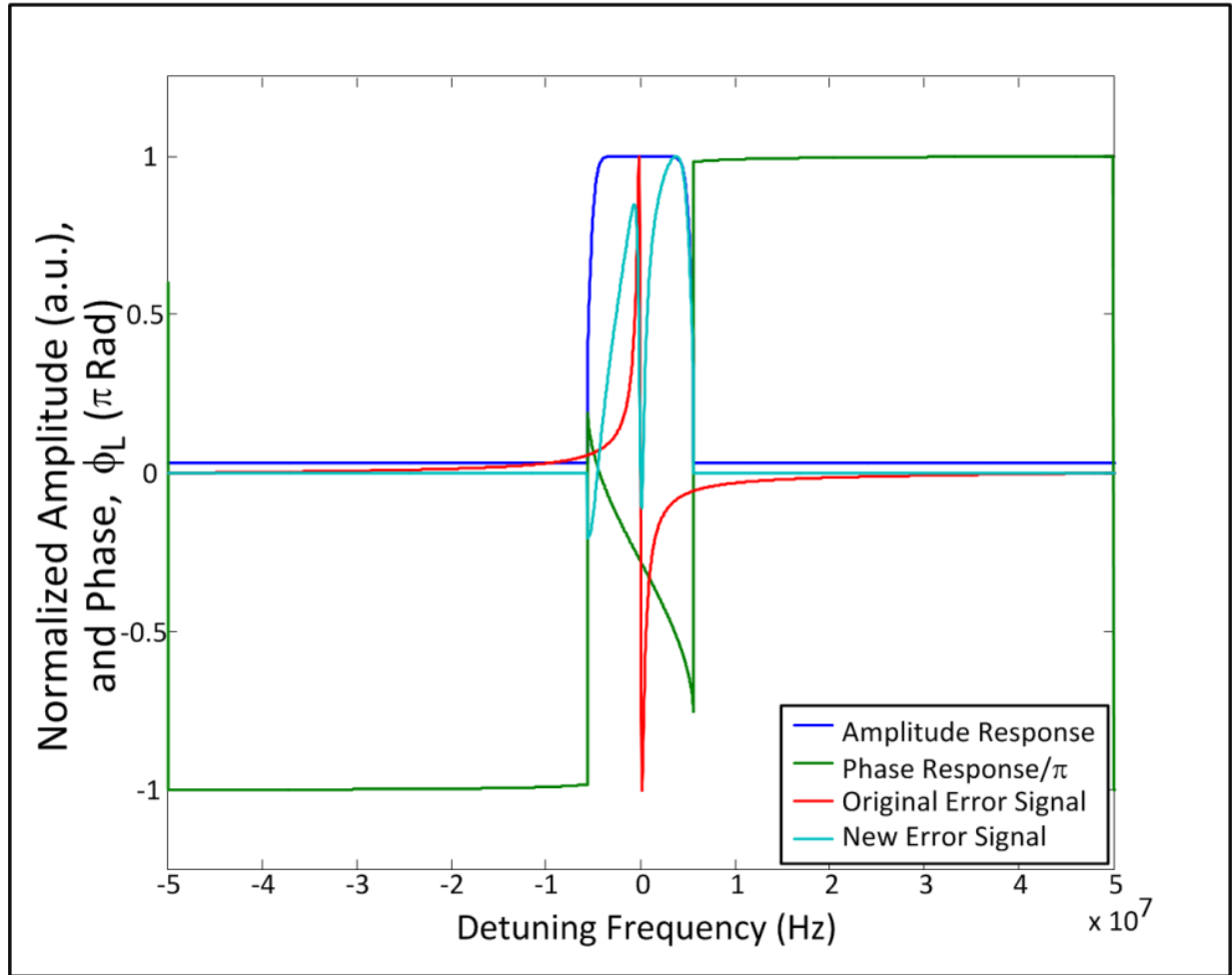


**Figure 6.4.** Amplitude (blue) and phase (green) response of slaved cavity resonance with gain, as well as original HC error signal (red) and signal of the HC technique applied to a semiconductor cavity with gain (teal).

The error signal for the HC locking technique with both a passive cavity and a cavity with gain are also plotted in Figure 6.4. The injection locked error signal is also shown in Figure 6.5, as well as the experimentally obtained error signal for comparison, taken with 20  $\mu\text{W}$  in injection power. The center of the error signal shows qualitative similarity between them, with two upward loops and two downward spikes. Disagreement at the edges of the error signal feature, occurring at  $-0.5 \times 10^7$  and  $+1 \times 10^7$  Hz detuning frequency is possibly the result of divergence from ideal asin resonance phase

and could be accounted for as described in Section 4.2.3. The HC simulation fit is achieved with a similar alpha parameter as that of the PDH simulation comparison.

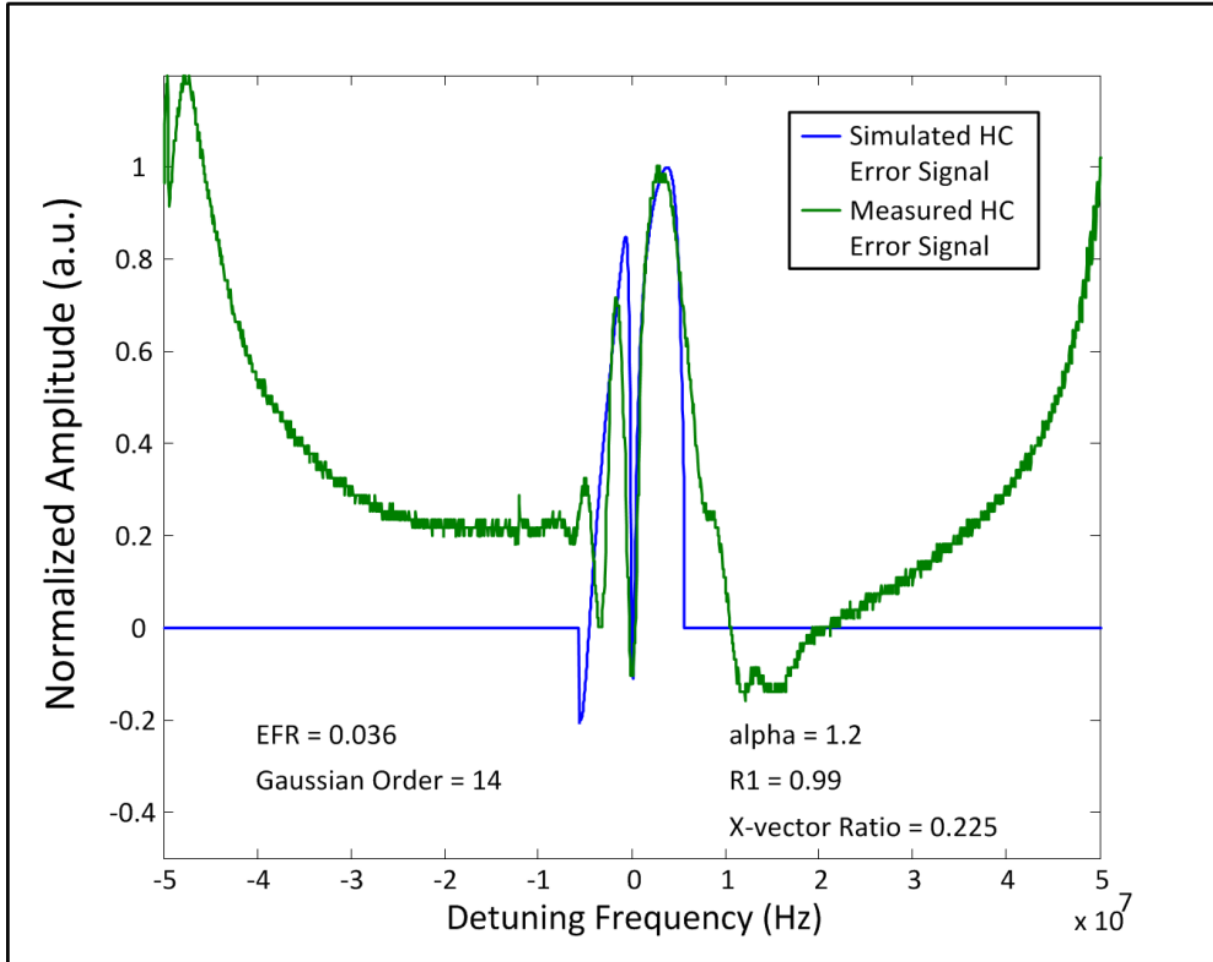


**Figure 6.5.** Experimentally obtained polarization spectroscopy error signal (green) comparison to simulated (blue).

Further exploration is needed to match the measured error signal shape further and to understand the mechanisms behind it, in particular the difference between injection electric field ratios used for the PDH and HC error signal simulations.

### 6.3 Stabilization via Polarization Spectroscopy: Results and Conclusion

Figure 6.6a shows the optical spectrum without injection, as well as the full optical bandwidth achieved by the injection locked system, which has been observed to be constant for times greater than 20 minutes.

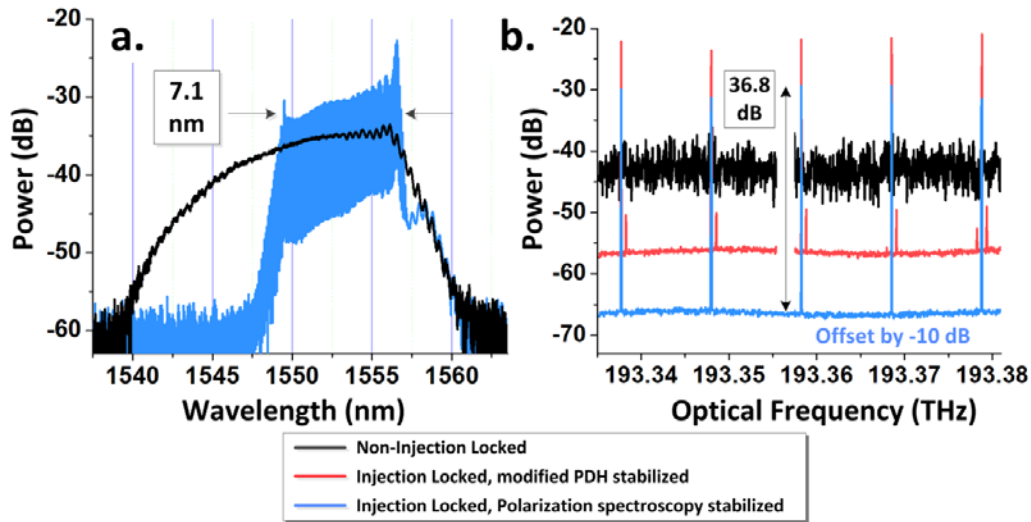


**Figure 6.6.** (a) Optical spectra of HMLL not subject to optical injection (black) and injection locked and stabilized via polarization spectroscopy (blue). (b) High resolution optical spectra of HMLL output showing frequency comb generation under optical injection with high OSNR. The latter curve was artificially offset by -10 dB to illustrate the absence of PM sidebands on each combline.

Figure 6.6b shows the high resolution optical spectra of the HMLL system centered 50 GHz below the injection frequency. When not injection locked (black), multiple axial mode groups are allowed to lase, resulting in a seemingly continuous spectrum due to the resolution of the optical spectrum analyzer ( $\sim 100$  MHz). When injection locked, a high quality comb is generated at the repetition frequency. When the cavity is stabilized using the modified PDH scheme (red), sidebands from phase modulation (550 MHz) of the injection seed laser also appear on other combines of the optical spectrum due to modulation by the intracavity IM, visible in Figure 6.7b.



Accordingly, RF spurs appear 20 dB above the noise floor at offsets from the carrier frequency in the photodetected RF spectrum, shown in Figure 6.7. When stabilized using polarization spectroscopy (blue in Figure 6.6b), the high resolution optical spectrum shows a sideband-free optical frequency comb with greater than 35 dB OSNR. The elimination of phase modulation in the detection scheme produces a sideband-free RF spectrum with SNR of 72 dB.

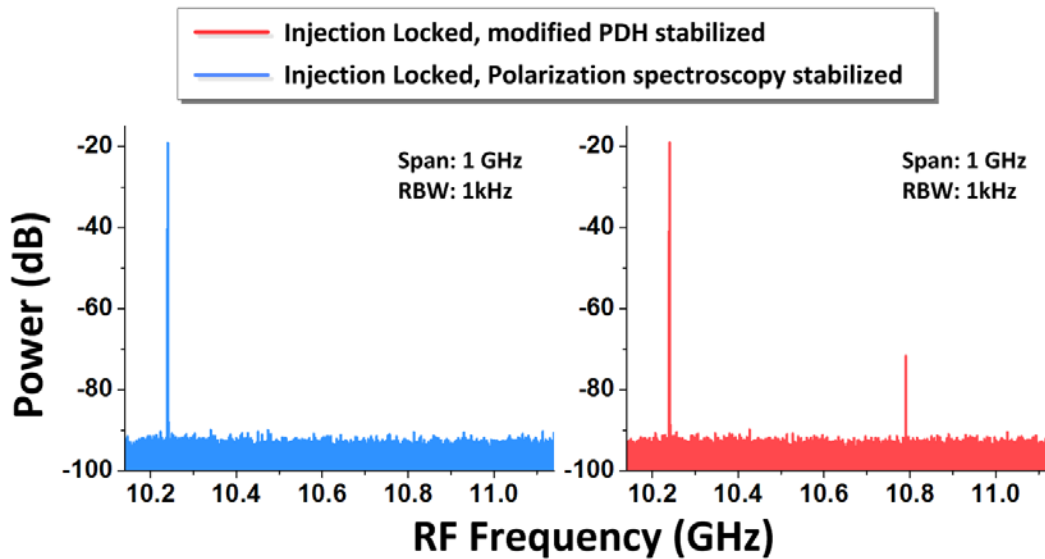


**Figure 6.7.** Photodetected RF spectra of the injection locked laser stabilized via the two methods. Note the absence of an RF sideband 550 MHz offset from the 10.24 GHz carrier for the HC stabilization method.

In conclusion, stabilization via polarization spectroscopy of an injection locked, HMLL is demonstrated for the generation of 10.24 GHz-spaced optical frequency comb. Injection locking is maintained for greater than 20 minutes with an OSNR of greater than 35 dB and sideband-free photodetected RF SNR of 72 dB. Widely spaced optical frequency combs with easily tunable spacing from this injection locked laser system are ideal for use in the field of multiheterodyne spectroscopy (Section 1.2.5).

## **CHAPTER 7: CW INJECTION LOCKING OF A COUPLED OPTO-ELECTRONIC OSCILLATOR**

Additional features that are desirable in frequency comb sources are low cost and portability. To that end, the removal of the external RF source used to drive the laser intensity modulator (IM) is paramount to the creation of a stand-alone optical frequency comb source. One method to achieve this is regenerative mode-locking. In this section, a CW injection locked Coupled Opto-Electronic Oscillator (COEO) is presented with a 10.24 GHz spaced optical frequency comb output as well as a low noise RF output. A modified Pound-Drever-Hall scheme is employed to ensure long-term stability of the injection lock. This is achieved by using a fiber stretcher to adjust the cavity length. The slaved cavity resonance position shifts accordingly to compensate for cavity resonance drifts relative to the injection seed frequency. High optical signal-to-noise ratio of ~35 dB is demonstrated with >20 comb lines of useable bandwidth. The optical linewidth, in agreement with injection locking theory, reduces to that of the injection seed frequency, <5 kHz. Low amplitude and absolute phase noise are presented from the optical output of the laser system. The integrated pulse-to-pulse energy fluctuation is found to be reduced by up to a factor of two due to optical injection. Additional decreases were shown for varying injection powers. This work has been presented in references [98-101].

Excellent absolute RF phase noise has been reported in the literature using the COEO configuration [102, 103]. These sources are erbium fiber gain-based, harmonically mode-locked, and are used primarily for their low-noise RF output and

soliton-induced short optical pulses. In contrast, the current work utilizes semiconductor gain media and offers a stabilized frequency comb output which is useful in the previously outlined applications (Section 1.2), especially in the burgeoning field of multiheterodyne detection. This application can often place stringent requirements on the comb-line spacing of multiple frequency comb sources. While another COEO design offers a frequency comb output referenced to an intracavity etalon [104], stable frequency combs with easily tunable comb-line spacing generated using a CW tone are particularly advantageous for applications such as multiheterodyne detection. This section features such a source in the form of an optically injection locked COEO. An extensive characterization of noise properties, including high resolution optical spectra, RF supermode noise spur suppression, amplitude noise, absolute phase noise, and Allan deviation, is presented.

## **7.1 Regenerative Mode-Locking**

Without a mode-locking signal applied to the intracavity IM, all laser modes are free to lase independently, meaning they do not have a fixed phase relationship. Upon photodetection, a small RF beating between adjacent cavity modes will be detected at the cavity fundamental frequency,  $\nu_0$ , as well as  $2*\nu_0$ ,  $3*\nu_0$ , and so on up to the bandwidth of the photodetector. One of these small amplitude RF beats could be selected by an RF filter, amplified, and applied to the intracavity IM to achieve mode-locking using the laser's own photodetected output, as shown in the simple schematic in Figure 7.1. This mechanism is called regenerative mode-locking, and the resulting system is referred to as a COEO [105].

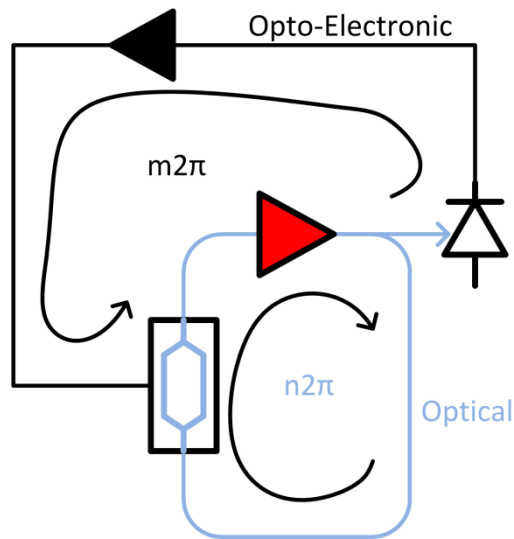


**Figure 7.1** Schematic of a typical Coupled Opto-Electronic Oscillator. The optical cavity is shown in blue, with gain (red triangle) and intensity modulator (left). The electronic part of the opto-electronic cavity is shown in black, where the output is photodetected (right), filtered (not shown for simplicity), amplified (black triangle) and fed back into the intensity modulator.

The optical output of a COEO is much like that of a HMLL, yet several attractive and interesting features result from this configuration. First, the COEO is a stand-alone oscillator, eschewing the need for an electrical frequency synthesizer, and improving portability. Secondly, this oscillator system offers both an optical and RF output, which could be useful for applications requiring precise triggering relative to the pulse timing. Additionally, since it is no longer slaved to an RF oscillator, interesting challenges arise in improving the stability of both the optical frequencies and the repetition rate.

Note in Figure 7.1 that the COEO consists of two coupled cavities, a purely optical one, and a combined opto-electronic one, which shares a portion of the optical cavity. While it is apparent that laser modes must accumulate a total round-trip phase of multiples of  $2\pi$  in order to undergo constructive interference and therefore survive in the cavity, the same is also true of the RF tone traveling through the opto-electronic loop.

The particular radio frequency travelling through the opto-electronic loop and used for mode-locking is ultimately determined by the optical cavity mode spacing. Therefore, in order to properly achieve mode-locking after an RF tone has been chosen by the optical cavity, its phase must be adjusted via an RF phase shifter to satisfy the  $2\pi$  condition stated above.

## **7.2 Injection Locked COEO Experimental Setup**

Figure 7.2 shows the laser system setup with the feedback loop. Optical gain is supplied inside the optical cavity via a commercially available semiconductor optical amplifier (Covega BOA1004) with gain in the 1550 nm spectral region and a saturation power of 16.5 dBm. Two optical couplers are used to couple light out of the optical cavity and couple the injection seed into the cavity. A Mach-Zehnder IM is employed to actively mode-lock via loss modulation. Approximately 1.3 m of dispersion compensating fiber ( $D \sim -169$  ps/nm·km) is used to balance the anomalous dispersion of the ~18 m long optical cavity, comprised primarily of standard single-mode fiber ( $D \sim 17$  ps/nm·km). This corresponds to a cavity fundamental frequency of ~11 MHz and an estimated total dispersion of 0.0732 ps/nm for the fiber components of the cavity, not counting the modulator crystal and the semiconductor gain medium. An optical isolator is used to ensure unidirectional light propagation in the cavity. The optical cavity is contained in an insulated enclosure to minimize the effect of environmental factors on the setup.

The opto-electronic loop components are shown in the top right of Figure 7.2. Part of the light from the output coupler of the optical cavity is photodetected, and the

RF tone at the desired repetition rate of the laser, i.e. 10.24 GHz, is bandpass-filtered, amplified and applied to the intracavity IM to regeneratively mode-lock the laser. The RF bandpass filter (16 MHz FWHM) determines the repetition rate of the COEO system, and can be swapped out for simple and expedient tuning of the comb-line spacing. An RF phase shifter ensures synchronization of the RF signal with the optical pulses. A low noise RF output is available by splitting the signal before the IM, an important feature of the COEO design.

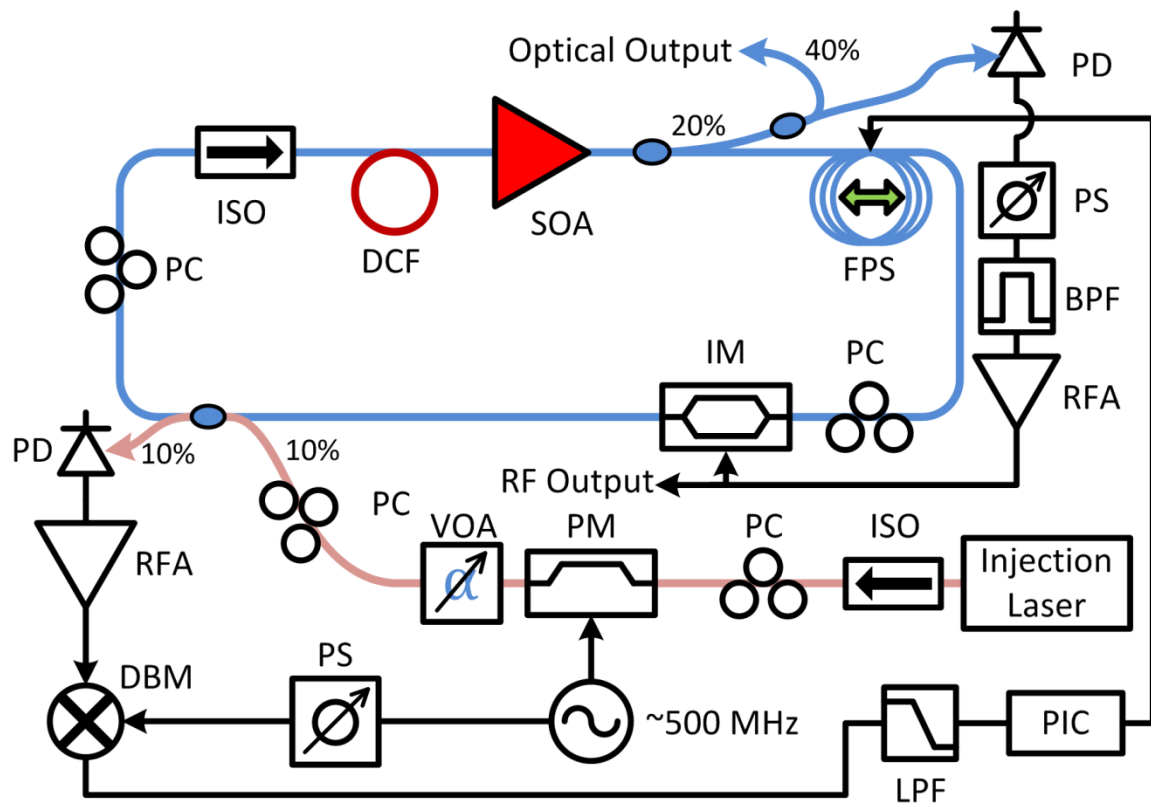


**Figure 7.2** Injection Locked COEO system schematic. BPF, Bandpass Filter; DBM, Double Balanced Mixer; DCF, Dispersion Compensating Fiber; FPS, Fiber Phase Shifter; IC, Injection Coupler; IM, Intensity Modulator; ISL, Injection Seed Laser; ISO, Isolator; LPF, Lowpass Filter; OC, Output Coupler; PC, Polarization Controller; PD, Photodetector; PIC, Proportional-Integral Controller; PM, Phase Modulator; PS, Phase Shifter; RFA, RF Amplifier; SOA, Semiconductor Optical Amplifier.

The injection arm consists of a commercially available CW laser at 1550 nm and a phase modulator (PM) for the Pound-Drever-Hall feedback loop. The CW laser has a linewidth of <5 kHz and a drift of <300 kHz over 30 s.

The feedback loop for stabilizing a cavity resonance to the stable injection seed frequency uses an RF frequency of ~500 MHz to drive the PM. The signal on the other side of the injection port, which has interacted with the optical cavity, is photodetected, amplified, and mixed in a double balanced RF mixer with the original signal, producing the sum and difference of the two frequencies. An RF phase shifter is employed in the reference arm to ensure the two signals are in quadrature. This signal is then lowpass-filtered to yield a differential error signal, which is used by a servo controller to align a cavity resonance with the injection seed frequency via an intra-cavity fiber phase shifter.

## **7.3 Injection Locked COEO Results**

### **7.3.1 Optical, RF Spectra and Time Domain Traces**

Figure 7.3 shows optical spectra of the COEO in both the free-running and injection-locked states. When free-running, the COEO spectrum appears broad and continuous, spanning the 30 nm shown in Figure 7.3a. Individual comb lines are not resolvable due to the close spacing of resonant laser modes comprising the competing axial mode groups. The power of each mode is relatively low, and the spectrum is identical to that of a HMLL. The injection locked spectrum looks markedly different, with a narrowing of the spectrum to 2.3 nm at -10 dB. Individual optical modes of the COEO system are also now clearly visible. The selection of a single axial mode group with locked phase, and the suppression of all other groups are shown by the increase in

mode contrast of the 10.24 GHz spaced modes. The suppression of the other supermodes, coupled with the phase-locking of the 10.24 GHz spaced modes produces the desired frequency comb output of the laser system. Power per combline in the resulting frequency comb is higher such that the total average power output of the laser system is relatively unchanged between the free-running and injection-locked states.

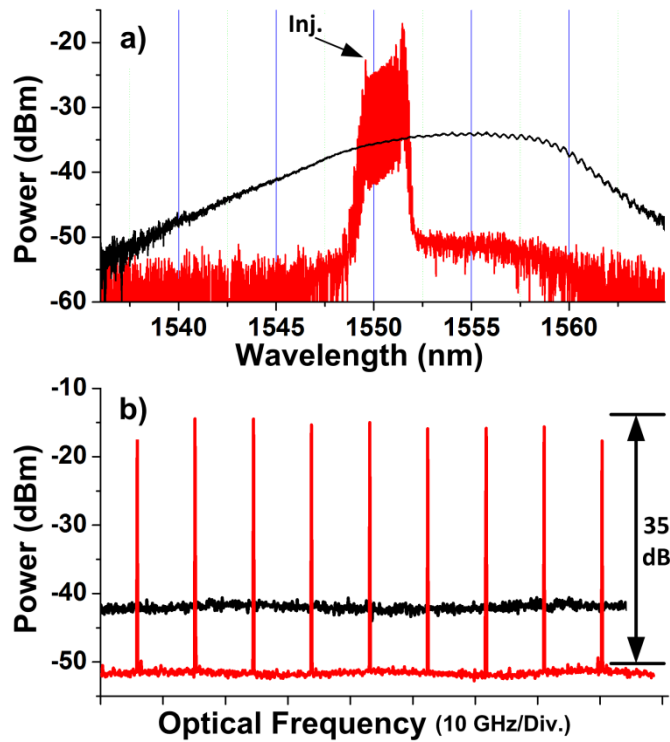


**Figure 7.3** (a) Optical spectra of the free-running (black) and injection-locked (red) states. The injection seed frequency is denoted by a black arrow. (b) High resolution optical spectra (100 MHz resolution). The optical modes in free-running operation (black) are too closely spaced (11 MHz) for the instrument to resolve.

The comb expands primarily to the longer wavelength side due to the ability of the injection seed to deplete gain from the higher energy transitions within the semiconductor, but not from lower energy transitions. This allows comb generation in the COEO at wavelengths longer than the injection seed. Optical comb generation is



confirmed in Figure 7.3b by measuring the optical spectrum with a high resolution optical spectrum analyzer. Once again, the free-running (black) trace appears continuous, since the individual laser modes are not resolvable by the instrument. In the injection-locked spectrum, 10.24 GHz spaced individual modes are clearly seen. A suppression of the unwanted axial modes of at least 35 dB is observed from the selected axial mode group. In separate tests, the optical linewidth of an injection locked laser system reduces to that of the injection frequency,  $< 5$  kHz.

Figure 7.4a shows the photodetected output of the injection-locked COEO system. The large tone on the left is the RF carrier frequency near 10.24 GHz. On the right, the nearest supermode noise spur is seen at an 11 MHz offset, representing the beating between adjacent optical axial mode groups. The injection-locked spectrum shows suppression of the spur into the noise floor,  $>15$  dB, corresponding to the suppression of all axial groups but one. Figure 7.4b details the RF carrier tone in a smaller span, showing significant RF noise reduction in the wings of the spectrum due to injection locking. This is due to increased correlation among optical frequencies contributing to the RF carrier frequency after injection locking. Long-term operation has been observed for longer than 15 minutes, proving the viability of the feedback mechanism. Recall that a  $\sim 500$  MHz frequency is used in the modified Pound-Drever-Hall scheme for the creation of phase modulation sidebands. Since all three frequencies are injected into the cavity, the sidebands could inject into other cavity resonances and appear in the RF signature of the system. This effect is suppressed by careful tuning of the phase modulation frequency along with the phase in the optoelectronic loop (which

strongly affects the repetition rate). The stabilization tone in the photodetected output was observed to be 54 dB below the carrier, when measured at 500 MHz offset.

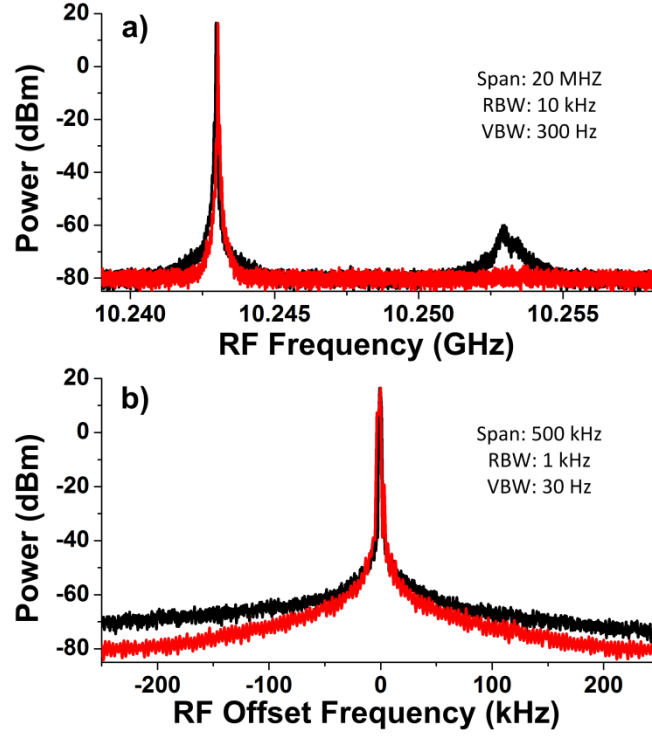


**Figure 7.4** (a) RF power spectrum of the photodetected COEO optical output, free-running (black) and injection-locked (red) with fundamental RF tone and one supermode noise spur, suppressed via injection locking. (b) Zoomed view of fundamental RF tones at ~10.24 GHz.

Figure 7.5 shows the photodetected time domain output of the COEO system in both the injection locked and free-running cases. Figure 7.5a shows the pulse train with a ~100 ps period, measured with a photodetector bandwidth of 16 GHz and a sampling oscilloscope. Note the improved uniformity in pulse amplitude in the injection locked pulse train (red). This amplitude noise improvement is further quantified below by extensive amplitude noise analysis.

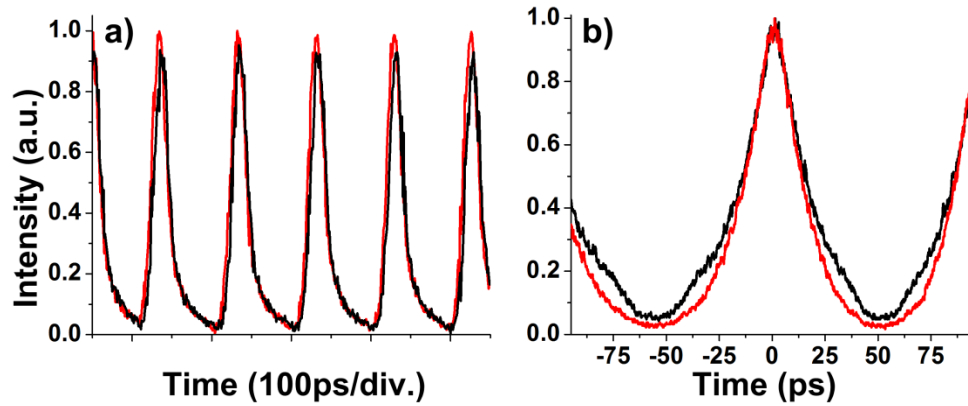


**Figure 7.5** Time domain normalized (a) sampling scope and (b) autocorrelation traces of the COEO output in both free-running (black) and injection-locked (red) cases.

In Figure 7.5b, autocorrelation traces show a 30 ps autocorrelation full-width at half maximum (FWHM) of pulses directly from the laser system with an average optical power of  $\sim 5$  mW. The wings of the injection locked trace appear less noisy. This is due to the increased correlation of modes in the optical spectrum after suppression of all but one axial mode group. Pulses directly from the injection locked COEO system are not transform limited for the optical bandwidth shown, as expected. Semiconductor lasers do not typically emit transform-limited pulses directly from the laser due to large nonlinearities in the gain dynamics causing strong linear chirp [92]. Since many of the intended applications of the system (e.g. optical arbitrary waveform generation, metrology, multiheterodyne detection) are not concerned with pulsewidth, compression of the pulse was not explored for the scope of this chapter. However, for applications where short optical pulses are of particular benefit, pulses from semiconductor lasers have been shown to be externally compressible to near the transform-limit pulsewidth [92].

### 7.3.2 Amplitude and Phase Noise

The amplitude noise of the optical output from the injection locked COEO is measured for varying injection powers using a commercial carrier noise test set, and the integrated pulse-to-pulse energy fluctuation from 1 Hz to 100 MHz offset was calculated for each. The power spectral density (PSD) results are shown in Figure 7.6. With the employment of injection locking, the supermode amplitude noise spurs are greatly suppressed. At 9  $\mu\text{W}$  of injection power, the integrated amplitude noise was found to be 0.0116%, nearly a factor of two improvement over the free-running case at 0.0196%. A definite but lesser improvement was seen with greater injection power, with  $\sim 14$  and  $\sim 20$   $\mu\text{W}$  resulting in 0.0113% and 0.0111% integrated noise, respectively.

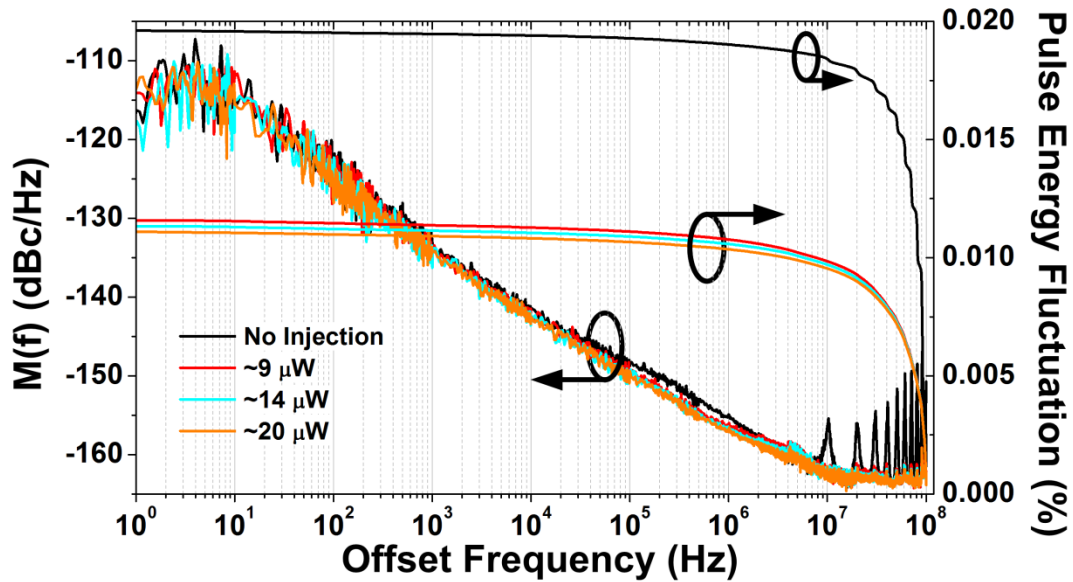


**Figure 7.6** Power spectral density of the amplitude noise of the injection-locked COEO for various injection powers: black, free-running; red,  $\sim 9$   $\mu\text{W}$ ; cyan, 14  $\mu\text{W}$ ; orange, 20  $\mu\text{W}$ . Pulse-to-pulse energy fluctuation for each case, integrated from higher to lower offset frequencies.

Due to the logarithmic method in which PSD data is plotted, the majority of the contribution to the reduction in noise comes from the suppression of the supermode noise in the last (highest frequency) decade. This distribution of noise contribution to the integrated pulse amplitude fluctuation is also demonstrated by the integration curves from higher to lower offsets. This measurement was taken with similar optical spectral bandwidth for all injection-locked cases. Higher injection powers were not tested since the useable spectral bandwidth decreases with increased injection power.

Applications for RF sources and optical frequency combs benefit from low timing jitter in the frequency range from the inverse of the measurement time (typically on the order of 100 Hz) to the Nyquist frequency at half the repetition rate. The COEO output pulse train resembles that of a HMLL. It should be noted that in HMLLs without a supermode noise spur suppressing mechanism, the influence of these spurs dominates the amplitude and phase noise integrated out to  $f_{Nyquist}$ .

For this reason, phase noise measurements of the COEO system are focused on observing the suppression of the supermode noise spurs present at multiples of  $1/T_{cavity}$ , the fundamental frequency of the cavity. The phase noise of the injection-locked COEO is measured using the frequency discriminator technique with  $\sim 15 \mu\text{W}$  of injection power [106]. Since the COEO acts as a stand-alone RF oscillator, the output is compared to its own delayed signal in order to measure phase noise power spectral density. This results in an absolute phase noise measurement, which is modulated by the frequency discriminator envelope due to the relative delay of each RF frequency between the laser output and its delayed equivalent:

$$TF(f) = 1 - \cos(2\pi f \tau_{delay}) \quad (6)$$

Division by this transfer function yields the absolute noise, with the exception of the null locations of the cosine transfer function. At these points, the phase noise measurement is divided by values approaching zero, leading to spurious features. Figure 7.7 shows the single-sideband absolute phase noise power spectral density,  $S_{\phi}(f)$ , of the injection-locked and free-running COEO system from 2 MHz to 300 MHz offset from the 10.24 GHz carrier, corrected according to equation (6), with  $\tau_{delay} = 27$  ns.

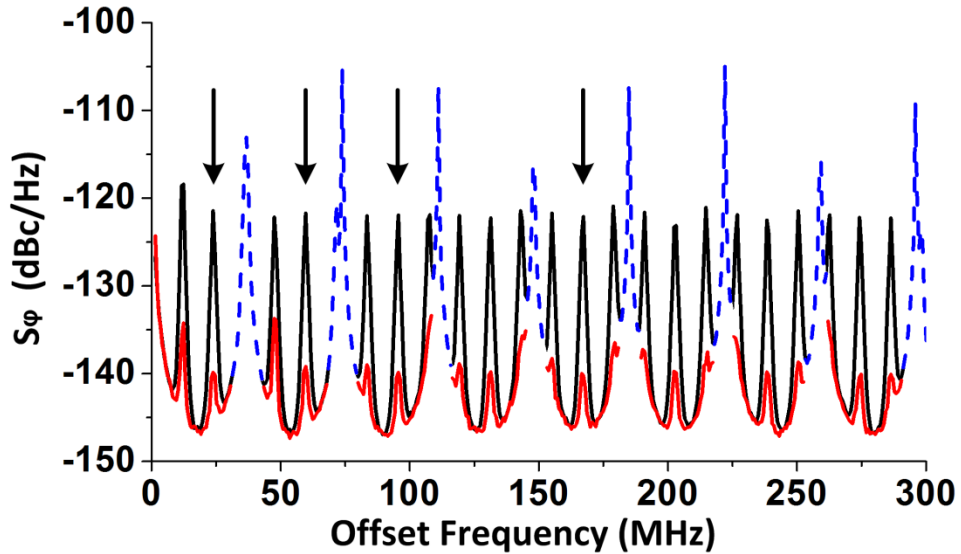


**Figure 7.7** Supermode noise spur detail of the absolute phase noise power spectral density of the COEO system in the free-running (black) and injection-locked (red) cases. Blue dashed peaks are spurious results of the frequency discriminator measurement. Offset frequency is shown in linear scale to highlight the suppression of supermode noise spurs at higher offsets. Arrows indicate modes used in timing jitter estimation.

The figure is deliberately shown in linear frequency scale so as to detail the supermode noise spur suppression achieved by the injection locking of the system, found to be ~18 dB by comparing the peak power of the spurs in the free-running case with their counterparts in the injection-locked case. Noise values significantly affected by the transfer function are set apart from the rest of the measurement by blue dashed lines.

Supermode noise spurs in HMLL noise spectra arise from a lack of correlation between pulses separated by less than the round trip time of the cavity [17]. Multiple pulses simultaneously traversing the cavity experience different spontaneous emission influences. The presence of these interleaved, uncorrelated pulse trains leads to periodicity in the noise spectrum at multiples of  $1/T_{cavity}$ . This implies that a rough estimate of the timing jitter integrated to Nyquist can be made via integration/timing jitter calculation of one period (i.e. one supermode noise spur) and multiplying by  $\sqrt{N/2}$  where N is the number of supermode noise spurs present, calculated by  $N=f_{rep}/f_{cavity}$ . The timing jitter over a specific range of the single sideband phase noise,  $L(f)$ , is given by [93]:

$$\sigma_J = \frac{T_{Rep}}{2\pi} \sqrt{\int_{f_{lower}}^{f_{upper}} L(f) df} \quad (7)$$

Estimations of the timing jitter were made via this method from four different peaks within the phase noise spectra, indicated by arrows in Figure 7.7. Where the ‘valleys’ between measurements are made uneven by transfer function influences, a half integration was performed from the lower valley and multiplied by two. Estimations

of the absolute timing jitter integrated to Nyquist for the free-running COEO yielded a median value of  $\sim 420 \pm 20$  fs. When injection locked, this value dropped significantly to  $\sim 115 \pm 15$  fs. In all cases, timing jitter was suppressed using injection locking by a factor of at least 3.

Phase noise at low offset frequencies was not measured, but has been shown in the actively mode-locked case to be greatly influenced by the injection seed. A reduction in optical linewidth in HMLLs is correlated with a reduction in the ‘knee’ frequency [50]. This strongly influences timing jitter integration, both at low offsets and in the supermode noise spurs, since the phase noise plot is periodic at  $1/T_{cavity}$ . Optical injection locking leads to a reduction in output optical linewidth to that of the injection seed, and therefore should reduce low-offset phase noise [58]. However, long-term instabilities in the injection seed frequency will translate to instabilities in the RF output, as discussed below, and therefore an increase in noise at very low-offset frequencies. This has also been shown in actively mode-locked injection locked lasers [58, 107].

### 7.3.3 Allan Deviation

A more common metric for measuring the long-term stability of an RF signal is the Allan Deviation (ADEV) of an oscillator [108, 109]. An extensive explanation of ADEV can be found in APPENDIX A. The ADEV of the injection locked COEO was measured for the photodetected optical output in both free running and injection locked states for time intervals from 100 ns to 1 s. The results are shown in Figure 7.8. Multiple frequency measurements are taken at a specific time interval using a Pendulum CNT-91 frequency counter with zero dead time, and their two-sample variance is calculated.



The square root of this is the deviation, yielding each point in the plot. This is then the degree to which the frequency value in a particular time interval is replicated in the next measurement of that time interval.

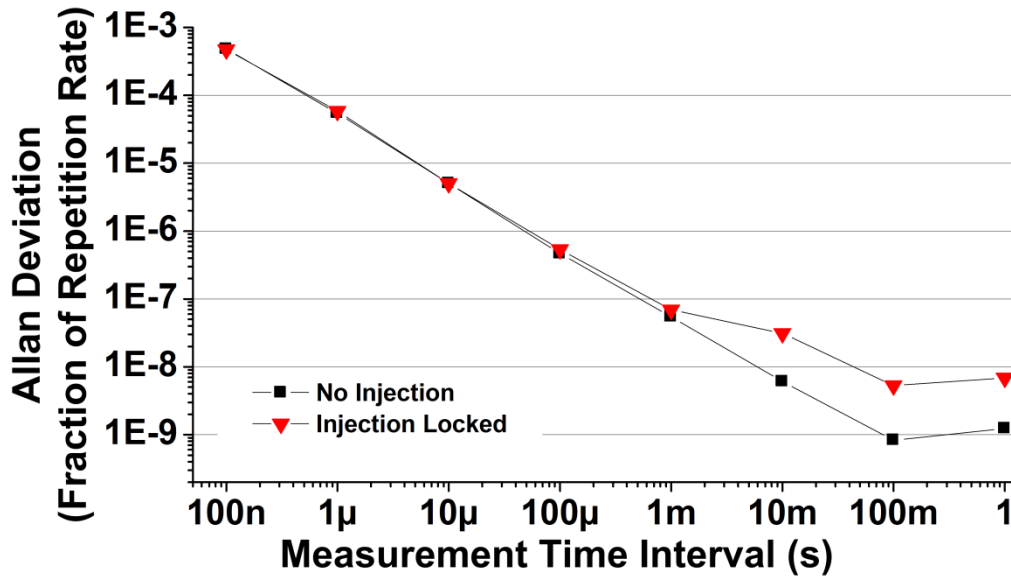


**Figure 7.8** Allan Deviation measurements of the Injection Locked COEO from the photodetected optical output for both injection locked (red triangle) and free-running (black) states.

The traces in the ADEV measurement follow typical trends for measurements of stand-alone oscillators, decreasing in fractional deviation of the repetition rate to a certain point, beyond which it begins to increase in value again, a result of long-term drift [110]. The ADEV of the free-running oscillator reaches a minimum value of  $10^{-9}$  at 100 ms. The RF (not shown) and optical outputs of the system in each case present similar values for the ADEV measurement, as expected, since the RF output contains little difference in carrier frequency from the optical output, apart from amplifier phase noise and filtering from the RF filter.

The injection locked case, however, shows significant divergence at longer time intervals from the non-injection locked case, reaching a minimum value just below  $10^{-8}$  at 100 ms – almost a full decade higher than in the free-running case. This is believed to be due primarily to the instability of the injection seed frequency. In an injection locked laser with feedback, the cavity length is actively changed to position one particular resonance at the same frequency as the injection seed. This change in cavity length invariably changes the position of all other laser resonances and, more importantly, their spacing. In an actively mode-locked laser, this slight change in spacing will affect the phase that each optical tone accumulates as it travels around the cavity, as long as it is still within a resonance to some degree (and therefore doesn't experience significant destructive interference). The frequency of the optical tone will not be affected, as it is built up from the intensity modulator creating sidebands on each pre-existing optical mode at a frequency spacing determined by the frequency synthesizer used to mode-lock.

In a regeneratively mode-locked laser, however, this change in cavity length, and hence in optical mode spacing, is what ultimately determines the repetition rate of the system as a whole. For example, while a particular RF frequency is fed into the intensity modulator and the cavity length is tuned to accommodate a perturbation in injection seed frequency, the optical tones quickly accumulate a different phase than in the previous steady state. This change in optical phase leads to a different phase and amplitude (but not yet frequency) of the resulting RF beat at the mode-locking frequency. As this RF signal travels through the opto-electronic loop, it must also shift

frequency slightly in order to maintain a  $2\pi$  phase shift. In essence, a change in optical injection frequency leads to a change in the output RF frequency of the injection locked COEO. Instabilities in the CW laser frequency used to inject therefore lead to higher ADEV at long time intervals compared to the free-running COEO. The free-running COEO will experience the same effect due to normal cavity drift, but at longer time scales than that of a COEO slaved to a drifting CW laser frequency. This result could be improved by improving the long-term stability of the injection seed frequency.

#### **7.4 RF Frequency dependence on Injected Optical Frequency of Injection Locked COEO**

For various applications of mode-locked laser sources and frequency combs, stability of the comb spacing, and hence the RF tone produced by photodetection, is of particular importance. In a COEO, the stability of this tone is greatly influenced by the optical cavity length as well as the phase drift (also a cavity length change) in the opto-electronic loop. In previous experiments (Section 7.3.3), the stability of the injection frequency has also been shown to influence the RF stability of the COEO output. This section explores this relationship in greater detail and has been presented at the IEEE Photonics Conference in 2011 [111].

A schematic of the injection locked COEO used is shown in Figure 7.9a and is much the same as that shown in Figure 7.2. The optical cavity is shown in blue, while RF links are shown in black and the injection arm is shown in red. The CW lasers used to injection lock (Orbits Lightwave ETH-1550; Koheras BME 15ThAl) are commercially



### 7.4.1 Experimental Results

ADEV measurements were taken of the 10.25 GHz<sup>1</sup> RF output of the free-running COEO (without optical injection) and when injection locked with two different CW lasers with different ADEV signatures. Additionally, the ADEV of heterodyne beat tones between the CW injection seed lasers and the reference frequency comb were also measured. All measurements were normalized to their respective nominal ADEV measurement frequencies (~10.25 GHz for RF, 1.93E14 Hz for Orbits, 1.9478E14 Hz for Koheras) and are plotted in Figure 7.10a. For measurement times up to 1 ms, the COEO in both the free-running and injection locked states demonstrate the same stability. However, in both injection locked cases, the ADEV increased for measurement times greater than 1 ms, mimicking the shape of the respective injection laser's ADEV measurement, as shown in Figure 7.10a. This is believed to be due to the instabilities of the injection seed frequency transferring into RF frequency instability.

---

<sup>1</sup> Due to the nature of the COEO system and the configuration of this particular optical cavity, the repetition rate for the RF instability transfer experiments was 10.25 GHz. Repeatability at other repetition rates is assumed based on empirical evidence.

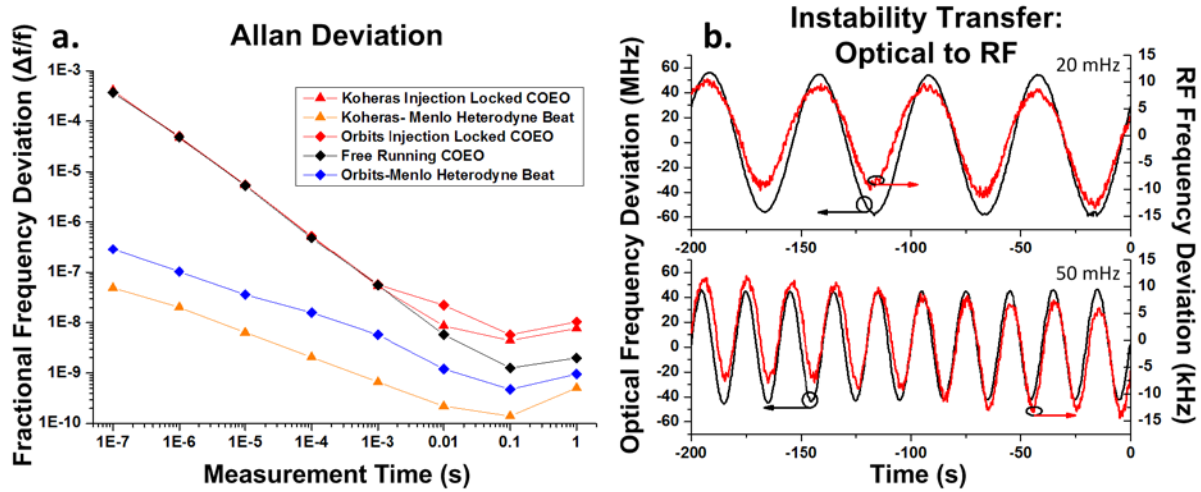


**Figure 7.10** (a) Allan Deviation measurements of the free-running and injection locked COEO, as well as of heterodyne beat signals between the injection seed lasers and an optical frequency reference. (b) Instability transfer from the optical injection frequency to the COEO RF output via sinusoidal modulation of the injection seed frequency.

An experiment was designed to test the optical-to-RF transfer of instability and is shown in Figure 7.9b. The CW laser (Orbits Lightwave ETH-10-1550) is used to injection lock and is slowly modulated using a sine wave at frequencies below 1 Hz (due to a built-in low-pass filter in the Orbits module). The optical frequency shift is detected using a heterodyne beat with a carrier-envelope-phase stabilized optical frequency comb (Menlo FC-1550). A spectrogram trace was taken via Real-Time RF Spectrum Analyzer. Simultaneously, the CW laser was used to injection lock the COEO and a feedback loop was employed to maintain an injection-locked state. The RF frequency of the injection locked COEO was then monitored using an RF frequency counter. The

results are shown in Figure 7.10b, where a clear transfer of instability from the injection optical frequency to the output RF frequency of the injection locked COEO is demonstrated. Various modulation rates and amplitudes of the optical frequency were measured yielding values of the ratio of optical-to-RF frequency change between 4800 and 8700 Hz/Hz.

#### **7.4.2 Discussion and Conclusion**

With the modified PDH stabilization utilized in the injection locked COEO, the laser cavity is adjusted such that the slaved cavity resonance follows the injection seed frequency. Since the exact RF frequency at the appropriate mode-locking harmonic is determined from the laser cavity itself in a regeneratively mode-locked system, changes in cavity length result in changes in repetition rate and hence output RF frequency from the COEO. Therefore, instabilities in the injected optical frequency will cause degradation in the long-term stability of the injection locked COEO as an RF oscillator. This has been demonstrated by a change in ADEV of the injection locked COEO for measurement times longer than 1 ms—both relative to a free-running COEO and when slaved to two different injection lasers with unique ADEV curves. Direct transfer of the optical injection frequency instability to the output RF frequency is also demonstrated via frequency counter measurements while the injection seed frequency is modulated. Further investigation of the origins of this RF instability will lead to better injection locked stand-alone oscillators providing both low-noise RF and high quality optical frequency comb outputs for photonic applications.

## CHAPTER 8: CONCLUSION

Stabilized, high repetition rate, semiconductor-based mode-locked lasers and frequency comb sources have a variety of potential uses in coherent communications, signal processing, optical clocking, and frequency metrology. Low noise operation is necessary for these applications, and the potential of a source sans any external microwave reference is appealing. In particular, the generation of widely tunable frequency combs with these qualities would be advantageous in various applications and measurements such as multiheterodyne spectroscopy. Single frequency injection locking of harmonically mode-locked semiconductor lasers is demonstrated to be effective in reduction of phase and amplitude noise and suppression of unwanted optical supermode groups so as to create an optical frequency comb with wide (GHz) comb spacing. Due to the harmonic nature of the mode-locking mechanism, the frequency comb spacing is also widely tunable. Long-term stabilization of this injection locked state can be achieved by either Pound-Drever-Hall frequency locking or polarization spectroscopy of the active laser cavity. Simulation and analysis of both error signal techniques as applied to active cavities with semiconductor gain is presented, incorporating amplification through gain and an arcsin phase profile adjusted as per the linewidth enhancement factor. Suppression of unwanted optical modes of 36 dB and supermode noise spur suppression of 14 dB is achieved. Injection locking of a regeneratively mode-locked system is demonstrated, obviating the need for a frequency synthesizer, and resulting in a stand-alone frequency comb source. Extensive characterization of the stand-alone frequency comb source is also presented.



**APPENDIX A:**  
**ALLAN DEVIATION MEASUREMENT**

A widely accepted measurement of the stability of an oscillator about a particular frequency is the Allan Deviation (ADEV) [108, 109]. The square of this is also sometimes used, and is referred to as the Allan Variance. ADEV is calculated using various time scales, as will be discussed later, and is normalized to a nominal frequency and presented as a spectrum of fractional unit values along an axis of measurement times. This appendix will serve to explain how ADEV is calculated, its usefulness in measuring oscillator stability relative to the well-known standard deviation, as well as how it is experimentally measured. In addition to the two seminal references included above and in the text of section 7.3.3, references [112-115] are extremely useful in gaining a greater understanding of the concept and were used in part to compile this appendix. Allan [116] and Rubiola [110] have also outlined the specific conversion relationships between laser phase noise and ADEV measurements.

Mathematical Deviations are useful in analysis of data to quantify and represent, within a particular dataset, variations from a standard value in a way that is easily comparable to other datasets from separate measurements. The well-known Standard Deviation (STDEV) compares values within a dataset to the mean of the same dataset, as shown by the STDEV equation given in Eq. ( 8 ). It should be noted that the dataset values are resulting from independent trials with ostensibly the same conditions, and the resulting STDEV is a single representative value. If the spread of values within the dataset is quite large, then the value of the STDEV will be high, and the converse is true if all values within the set are within a narrow range about the mean. This type of deviation is quite useful for distilling the characteristic variation down to a single value

which can be compared to the next dataset when the variation of values follows a “Normal Distribution” about the mean, which arises in many situations described above, where independent trials with the same conditions exist. When the dataset is a representative sample of a larger population, it is often used to infer the distribution of the larger population as well.

$$\sigma = \sqrt{\frac{1}{N} \sum [x_k - \bar{x}]^2} \quad (8)$$

A unique challenge is presented when applying a deviation to a set of values that are not independently determined from similar circumstances, such as a set of scores on a test, but are derived from the previous value with some additional influences, like the cumulative distance traveled in a car at any given point in time. The car’s position from the origin at the end of hour  $x$  depends greatly on its position at the end of hour  $x-1$ , as well as its average speed over that hour. Such is the case in the wandering frequency emitted from an oscillator. Many sources of noise affect the frequency of the signal, on a variety of timescales. In other words, there are slow and fast fluctuations of the instantaneous frequency. Given these many timescales, calculating a single representative value based purely on the ‘mean’ value of the signal is not only meaningless, but nonsensical, as the value of the mean will continue to change with measurement time.

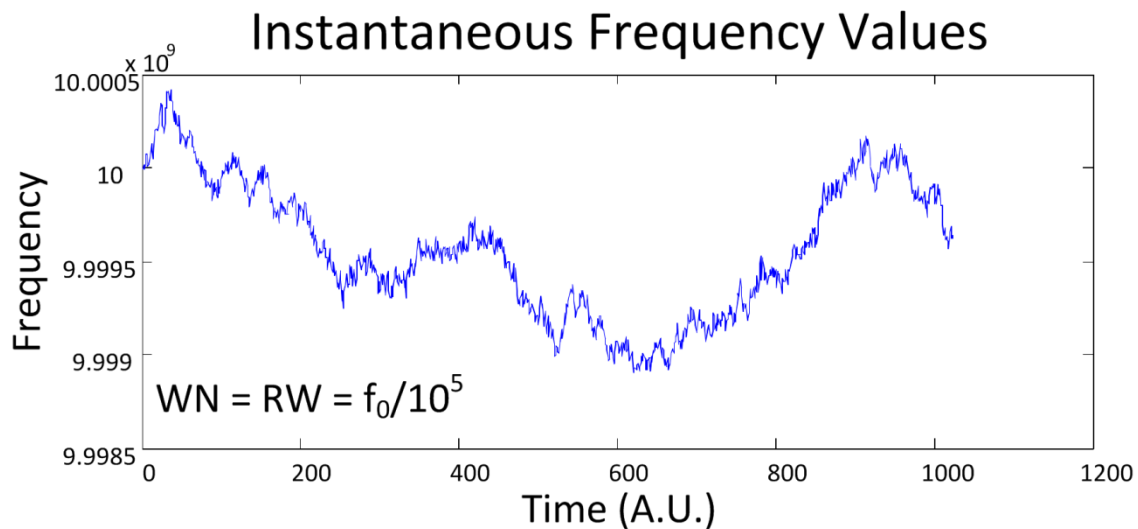


**Figure A.1** Simulated instantaneous frequency values of a non-stable signal at a starting frequency of 10 GHz.

Consider the signal in Figure A.1, where the instantaneous frequency is fluctuating randomly on a very short time scale, but is also slowly wandering with larger amplitude. Any STDEV calculated from a subset of values must be representative of the whole ‘population,’ but calculating based on the first 200 values would not account for the large variation from that mean happening in values after that. Using a larger ‘representative’ dataset would result in large deviations, considering at a glance how many values are far away from the middle or ‘nominal’ frequency, as well as gloss over the small amplitude fluctuations happening on small time scales. Therefore, a deviation that is useful in describing such contiguous wandering in a value with variations on many time scales must differ from the STDEV in at least two ways: 1) it must be a spectrum, representative of the many time scales on which variations can happen and 2) it must not be based upon a ‘global’ mean or average, since this average could be vastly different for each subset of values attempting to represent the global

characteristics, which would greatly affect the measurement. ADEV measurements are designed to accomplish both of these by taking many averages over the same time period, resulting in a single statistical deviation for that time period. The measurement and calculation is then repeated for other measurement time periods, with each deviation being plotted along the measurement time axis, as shown in the ADEV example graph in Figure A.2. The resulting curve is representative of the frequency stability of the oscillator under test.

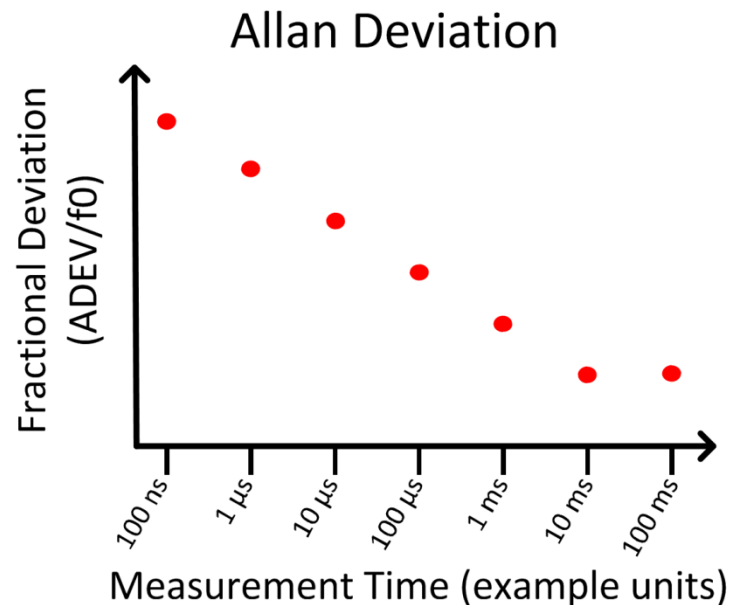


**Figure A.2** Typical Allan Deviation plot showing calculated fractional deviation values for increasing measurement times.

### **Equation and its Explanation**

The equation for ADEV ( $\sigma_y$ ) is given by Eq. ( 9 ), and differs from the Allan Variance (AVAR) only by the square root. The differences between averages is taken for the entire dataset, then individually squared and an expectation value is calculated

before taking the square root to yield the deviation – in other words, the root mean square of the differences in subsequent average frequencies.

$$\sigma_y(\tau) = \sqrt{\mathbf{E}\left\{\frac{1}{2}[\bar{f}_{k+1} - \bar{f}_k]\right\}^2} = \sqrt{\frac{1}{2(N-1)} \sum_{k=1}^{N-1} [\bar{f}_{k+1} - \bar{f}_k]^2} \quad (9)$$

ADEV for a particular measurement time is then the square root of the expected value of the square of differences between consecutive average frequencies of a time-domain signal. In practice, the expected value reduces to be the average of all the squared differences, or the number of averages, N, minus 1. A factor of ½ is included to normalize the statistical deviation to values commensurate with the real magnitude of deviations in the signal. An ADEV value is calculated for each measurement time, tau, divided by the nominal oscillator frequency to produce a fractional deviation, producing the curve shown in Figure A.2, above. In the equation,  $\bar{f}_k$  and  $\bar{f}_{k+1}$  are average frequency values of the k and the k+1 time bin. Note that these values are nearest-neighbors with no dead-time between average frequency measurements.

## **Experimental Measurement**

In the measurement of real frequency signals in a lab setting, ADEV is primarily performed with the assistance of a frequency counter. All ADEV measurements presented in this dissertation were performed using a Pendulum CNT-91 frequency counter. Important parameters for counters include input frequency bandwidth relative to the nominal frequency being measured, number of digits of resolution, and dead time. Dead-time, the amount of time between the end of one average measurement and the beginning of the next one, is a particularly important feature for ease of use. While

correction factors do exist for non-zero dead time while performing ADEV measurements, a zero dead-time frequency counter (such as the one used) makes this additional calculation unnecessary. In addition, a reference clock is necessary, either internal or from an external input. In either mode, reasonable confidence should exist that the reference clock is of better or similar stability as the oscillator under test. To this end, for state of the art ADEV measurements demonstrating record low instability, two identical oscillator systems are often compared against one another.

The frequency counter works by counting the number of zero crossings of the oscillating electrical signal for a particular time interval based on the reference clock. Many features exist in frequency counters to condition a noisy signal for proper measurement, and each counter's manual should be consulted for these features. Only the basics will be addressed here for the sake of understanding the process.

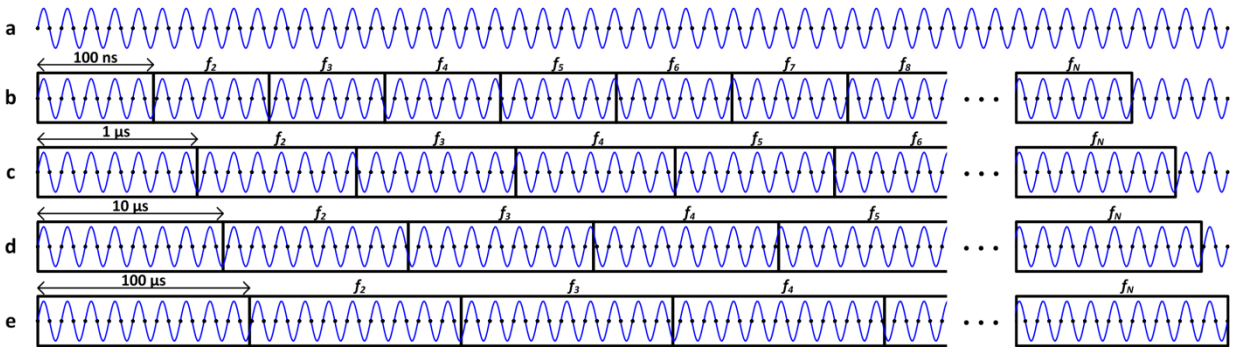


**Figure A.3** a) Oscillating signal of interest in blue with zero crossings shown by black dots. Boxes shown represent average frequency measurement times of b) 100 ns, c) 1  $\mu$ s, d) 10  $\mu$ s, and e) 100  $\mu$ s.

Figure A.3 illustrates an oscillating voltage signal (blue). As implied above, the counter is able to detect when the voltage passes between positive and negative (zero crossings, shown as black dots on the blue signal), and uses the number of these

crossings to determine the average frequency within a particular time interval. This is shown in Figure A.3b by the black boxes, each being its own frequency average measurement. Note that the boxes are contiguous, signifying the lack of dead-time between frequency measurements. Once ADEV is calculated for a particular timescale, e.g. 100 ns, another set of frequency averages are measured using progressively larger averaging times (Figure A.3c –Figure A.3e). The resulting ADEV values form the representative curve, an example of which is shown in Figure A.2.

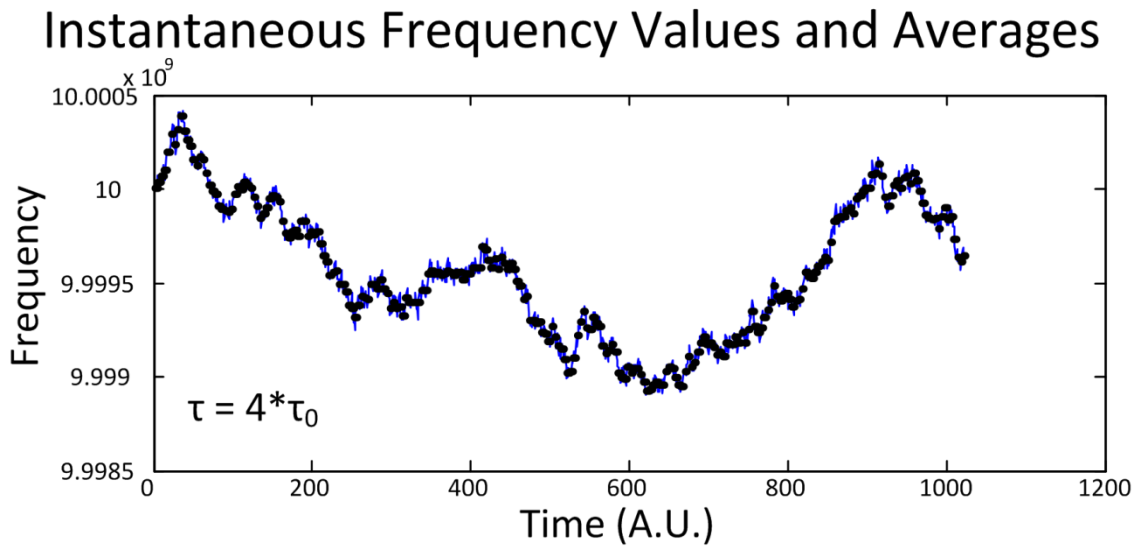
## **Simulation**

To illustrate the measurement, a simulation was designed to perform an ADEV calculation on a set of instantaneous frequency values with a nominal frequency on the same order of that of interest in our ADEV experiments – 10 GHz. The simulation was performed in Matlab, and the code is included in APPENDIX C. The instantaneous frequency dataset is generated by starting at the nominal frequency and adding a cumulative sum of two types of noise of interest to us: white noise (WN) and random walk (RW). Each value, therefore, is produced from the previous value plus an amount of each type of noise. The noise magnitudes can be specified and are defined in the frequency domain and relative to  $f_0$ , the nominal frequency.

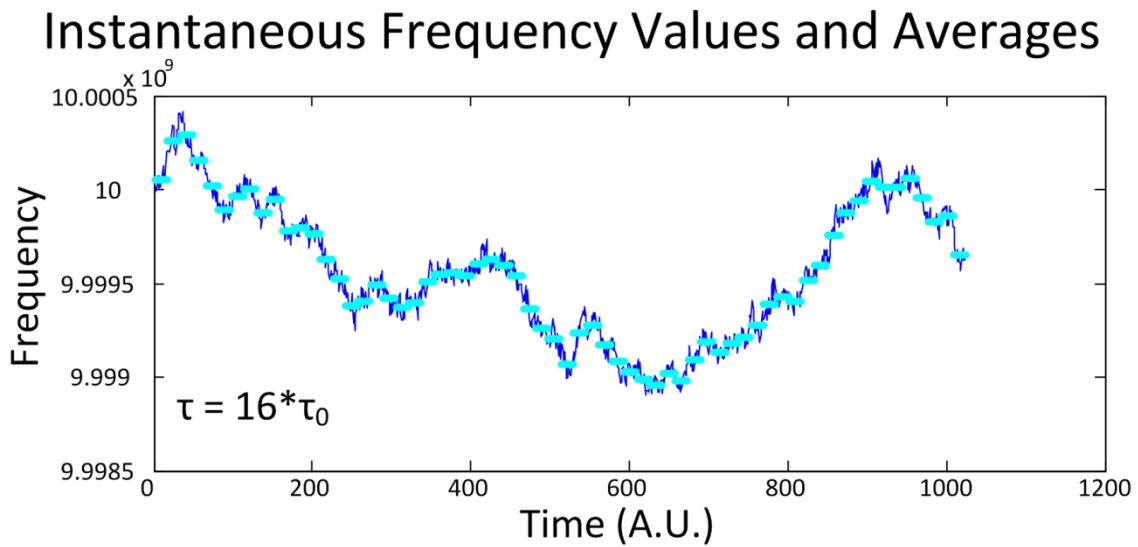
The instantaneous values, shown in Figure A.1, above, are defined on an arbitrary timescale, such that, while they can be considered ‘instantaneous’ in a broad descriptive sense, they can also be used as frequency averages of the signal on the smallest measurement time in the ADEV spectrum of values. Therefore, all other measurement times are specified in terms of this smallest time, tau. With this first set of



‘averages,’ the ADEV calculation is performed for measurement time  $\tau$  and divided by  $f_0$ . Averages of these values are then taken with measurement times of  $2^M * \tau$ , and the ADEV calculation performed. Figure A.4- Figure A.8, below, illustrate this averaging.

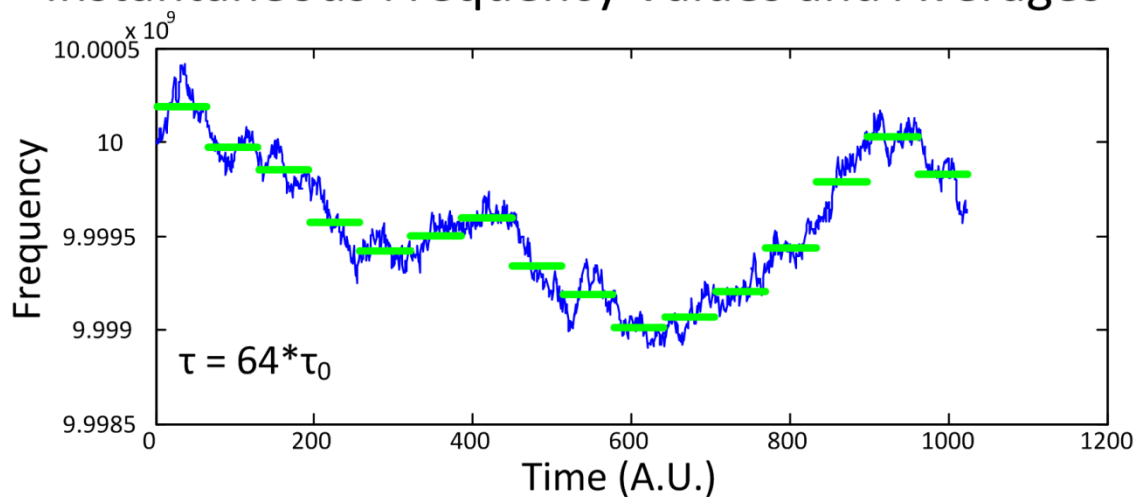


**Figure A.4** Instantaneous frequency values (blue) and averages (black) over four instantaneous time increments.



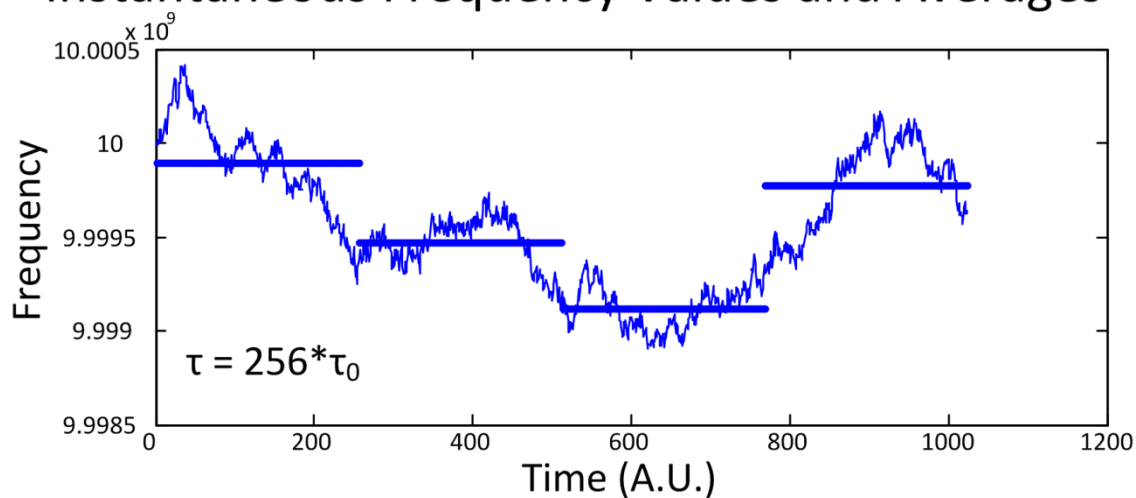
**Figure A.5** Instantaneous frequency values (blue) and averages (light blue) over 16 instantaneous time increments.

## Instantaneous Frequency Values and Averages



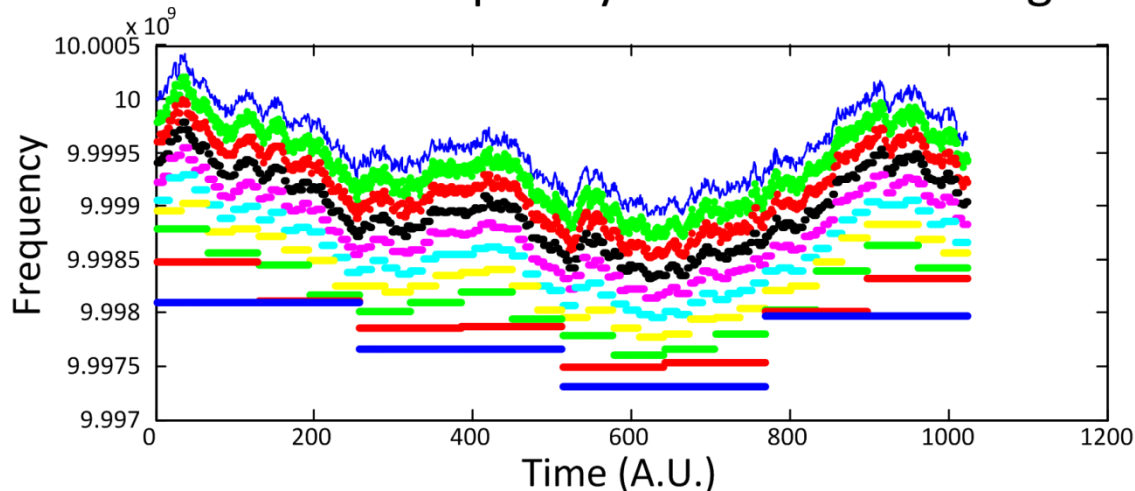
**Figure A.6** Instantaneous frequency values (blue) and averages (green) over 64 instantaneous time increments.

## Instantaneous Frequency Values and Averages



**Figure A.7** Instantaneous frequency values (blue) and averages (blue straight lines) over 256 instantaneous time increments.

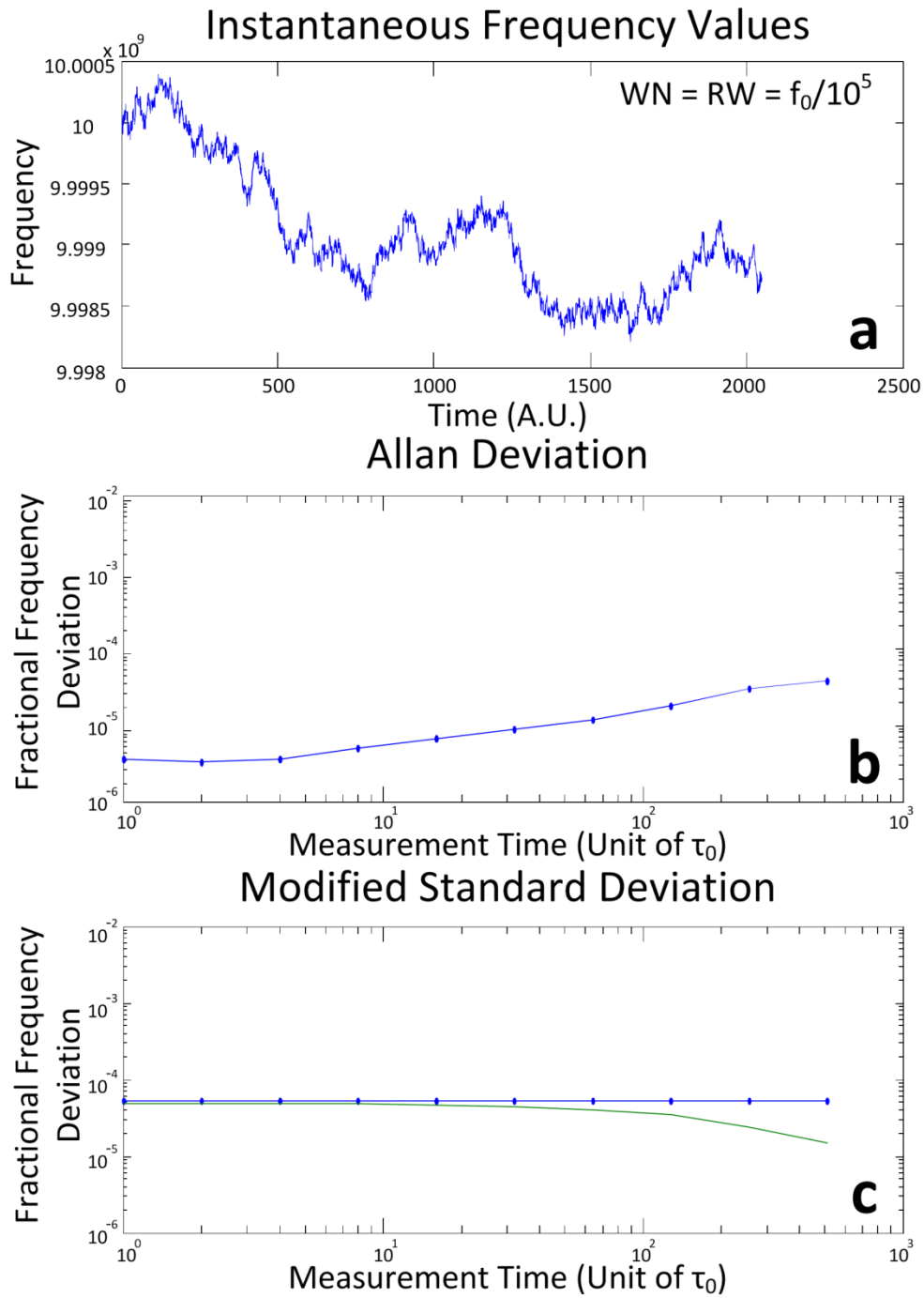
## Instantaneous Frequency Values and Averages



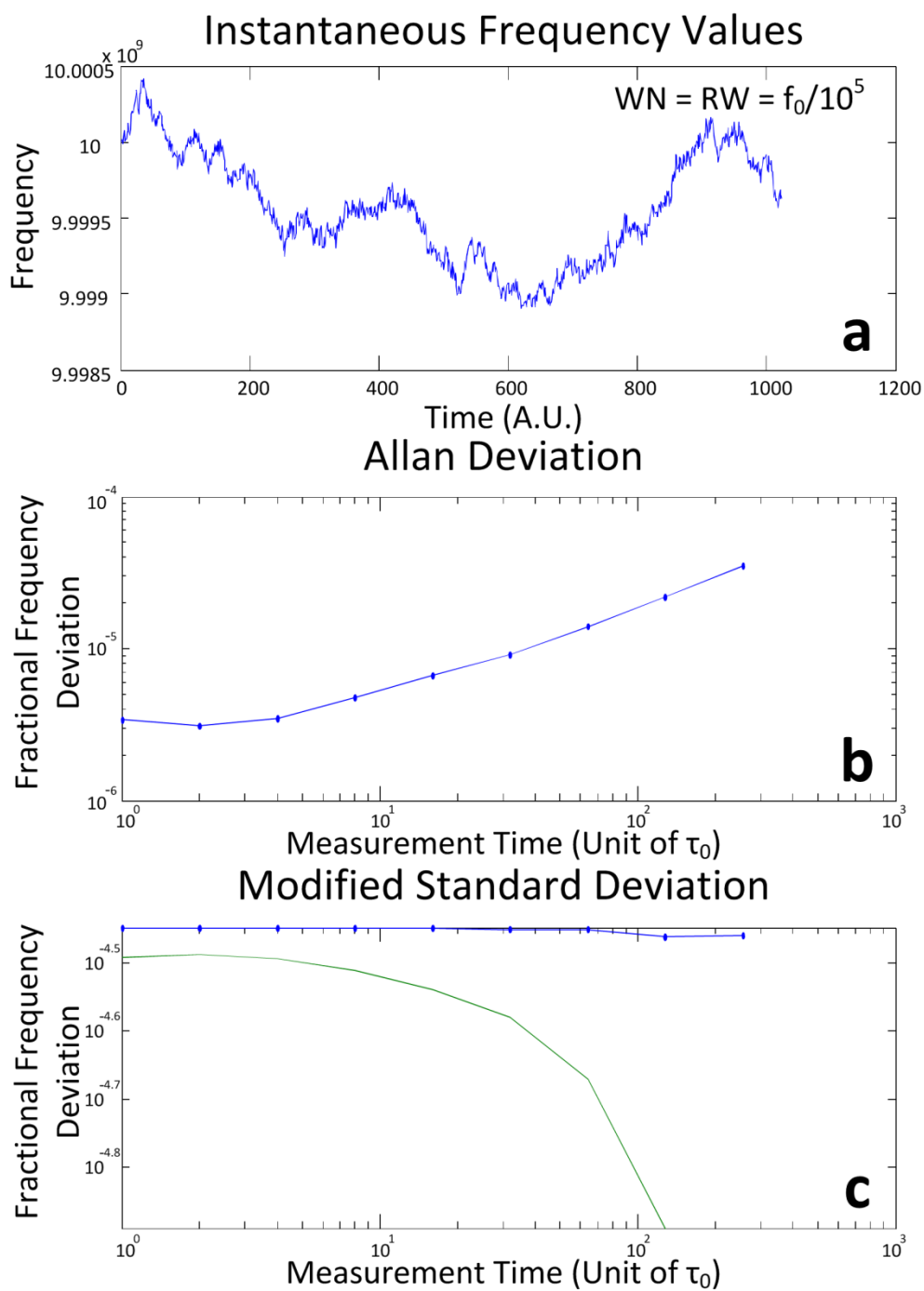
**Figure A.8** Instantaneous frequency values (top, blue) and averages over several instantaneous time increments.

### Examples and Explanations

A similar set of values (arrived at with the same amount of WN and RW) and its associated ADEV curve are shown in Figure A.9a and Figure A.9b. Note that the ADEV reaches a minimum value at  $2 \cdot \tau$  and begins to rise in instability for greater measurement times due to the small effect of white noise on the signal and the large, visible effect of random walk. Figure A.9c shows an associated variation on the STDEV of the signal, substituting the local average for the global average, an admittedly flawed method allowing for a deviation similar to that of STDEV to be calculated over a series of measurement times. Note that the value of STDEV remains a relatively constant value, obscuring any information on variations happening at different timescales. The difference between the ADEV and associated modified STDEV is shown (green curve) for clarity. A second example with similar parameters is shown in Figure A.10.

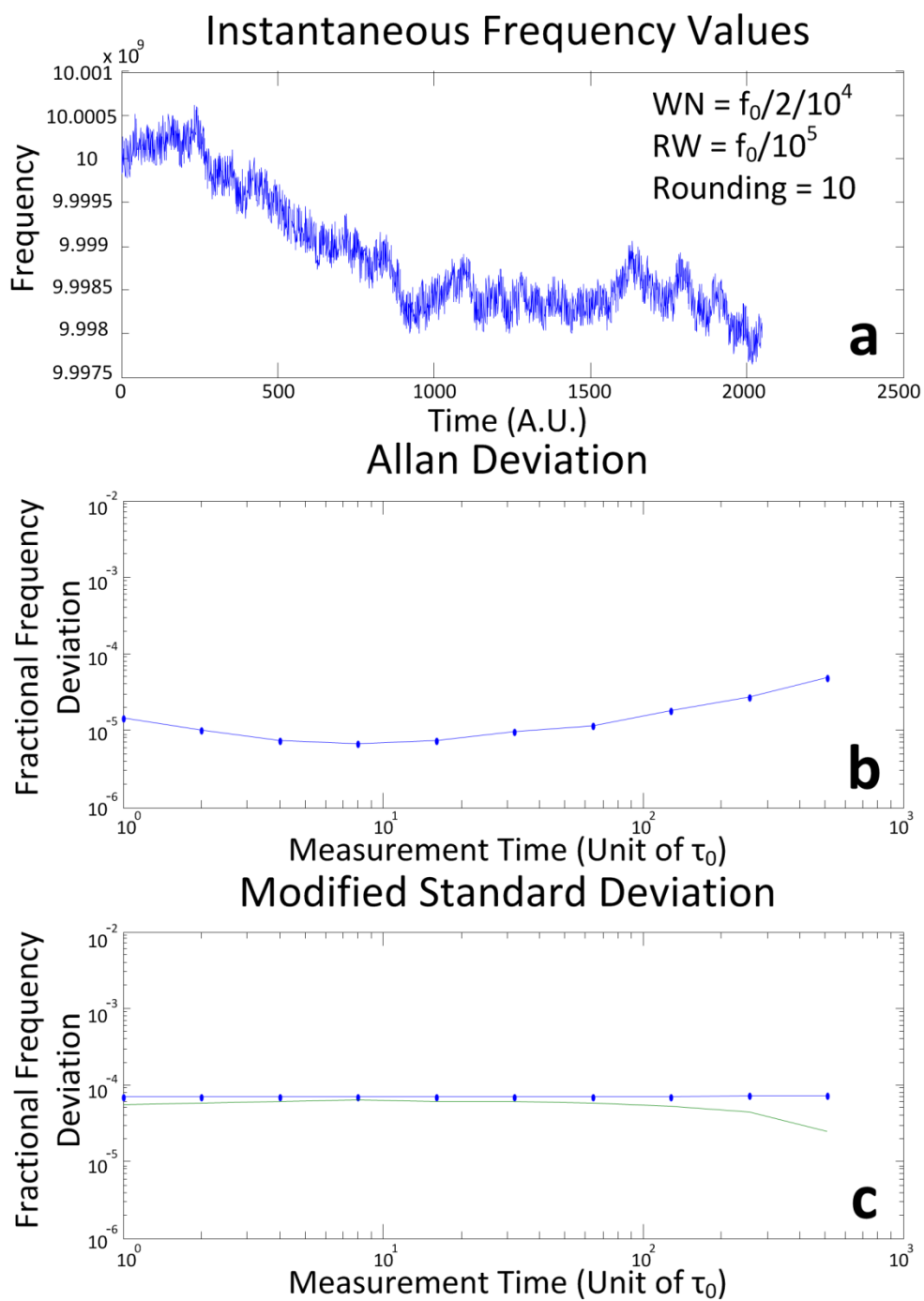


**Figure A.9** a) Instantaneous frequency values starting at 10 GHz and calculated with equal parts white noise and random walk. b) ADEV curve of the frequency values. c) Modified STDEV curve (blue) and difference between ADEV and STDEV (green) illustrating a lack of information given by such a measurement.



**Figure A.10** a) A second example of instantaneous frequency values starting at 10 GHz and calculated with equal parts white noise and random walk. b) ADEV curve of the frequency values. c) Modified STDEV curve (blue) and difference between ADEV and STDEV (green).

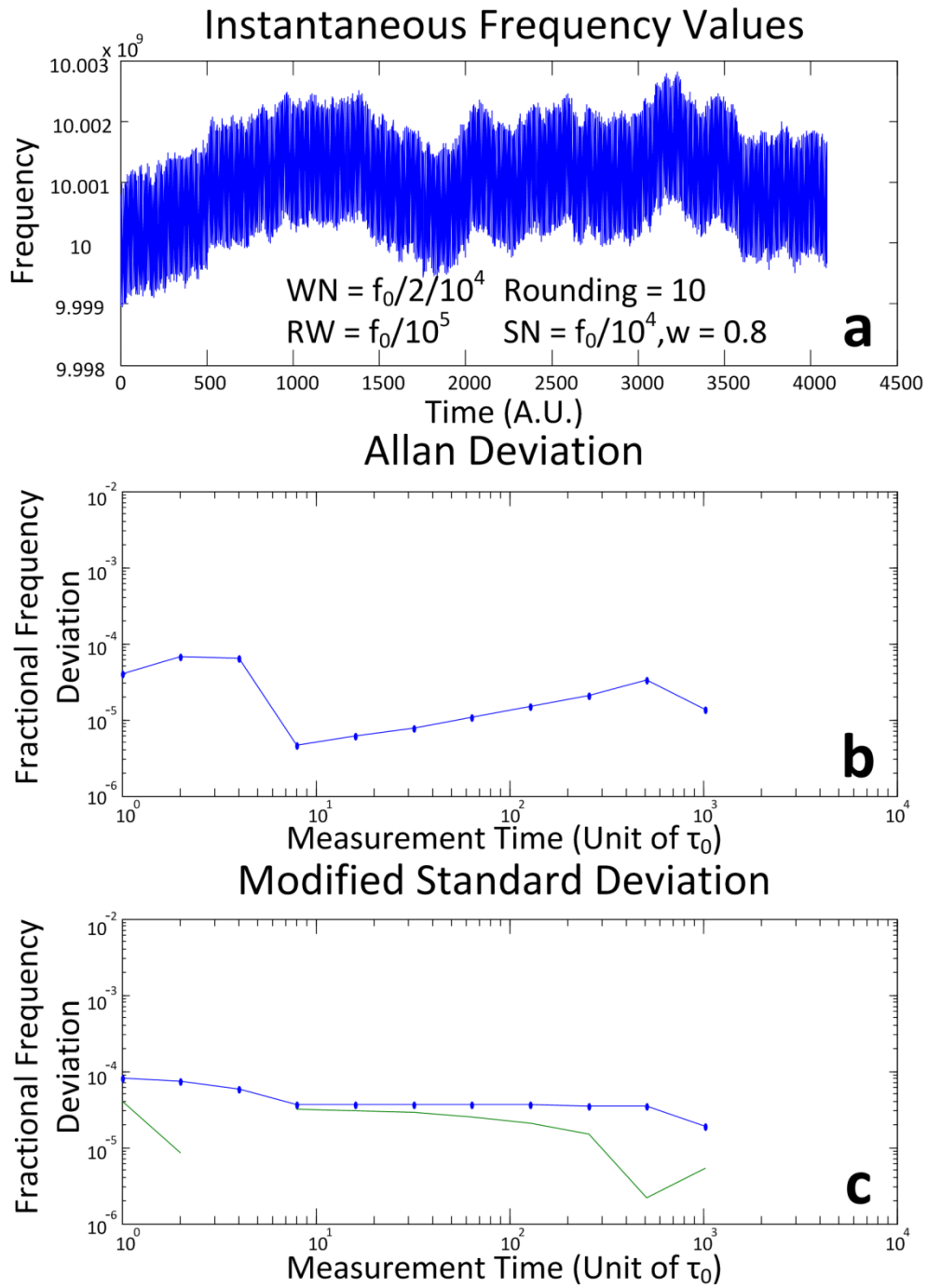
Figure A.11a-c show another example of a set of instantaneous frequency values defined with a half order of magnitude more white noise, along with the corresponding ADEV and STDEV curves. Note that the inclusion of more white noise prevents the ADEV from converging and reaching minimum instability until the  $8 \cdot \tau$  measurement time, while the STDEV is still a constant value.



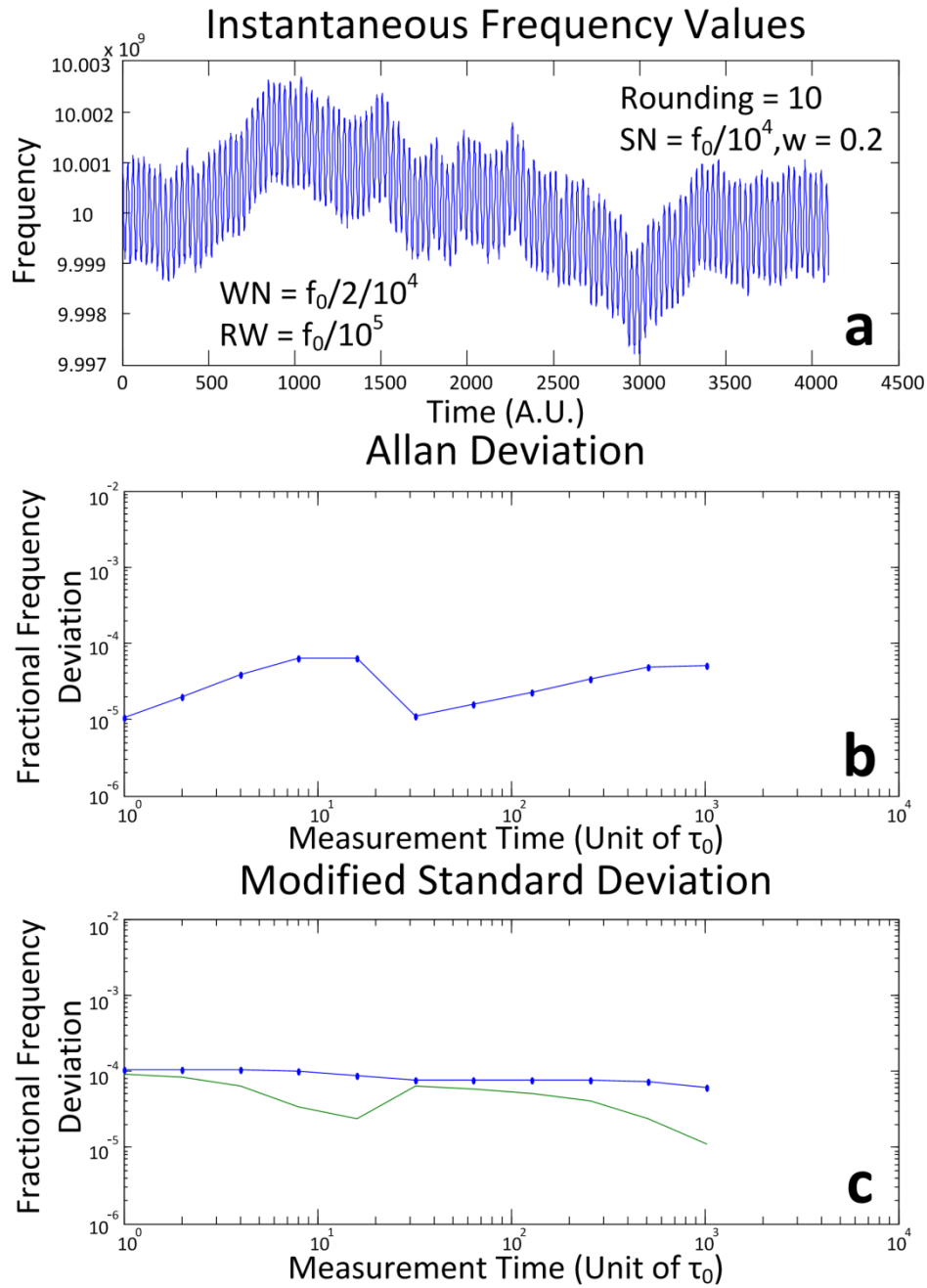
**Figure A.11** a) Instantaneous frequency values starting at 10 GHz and calculated with five times more white noise than random walk. b) ADEV curve of the frequency values. c) Modified STDEV curve (blue) and difference between ADEV and STDEV (green).

Figure A.12a and b and Figure A.13a and b illustrate an intriguing yet very small limitation of the ADEV measurement method. In the definition of the instantaneous frequency values, a sinusoidal modulation is included with a magnitude on the same order as that of the white noise. The ADEV curve is significantly affected by this modulation, as seen in Figure A.12b and Figure A.13b by the existence of a bump for short timescales followed by a sharp dip in the curve.





**Figure A.12** a) Instantaneous frequency values starting at 10 GHz and calculated with five times more white noise than random walk, as well as a rounding error and sinusoidal modulation introduced onto the signal. b) ADEV curve of the frequency values. Note the effect of the modulation on the curve shape at  $8 \cdot \tau_0$ . c) Modified STDEV curve (blue) and difference between ADEV and STDEV (green).



5

**Figure A.13** a) A second example of instantaneous frequency values starting at 10 GHz and calculated with five times more white noise than random walk, as well as a rounding error and sinusoidal modulation introduced onto the signal. b) ADEV curve of the frequency values. Note that the modulation is at a quarter of the frequency of the previous figure, and the associated anomaly in the ADEV curve is at  $32 \cdot \tau_0$ , four times that of the previous example. c) Modified STDEV curve (blue) and difference between ADEV and STDEV (green).

The reasoning for this is illustrated by Figure A.14, where an instantaneous frequency dataset which has been modulated with a low frequency sin wave and the corresponding ADEV averages are shown. The averages have been offset in the vertical direction for easier visualization. For timescales much shorter than the period of the sin modulation (green, red, and black at the top), nearest neighbor averages are quite different from each other, resulting in an increase in instability similar to the effect of random walk. As the averaging time begins to approach half the period of the modulation (teal, yellow, and green in the middle), the large fluctuations due to the modulation begin to be washed out and differences between nearest neighbor averages are much lower, leading to an abrupt reduction in the calculated ADEV instability (occurring at  $32 \cdot \tau$  in the example in Figure A.13). At larger timescales than this, the modulation is, for the most part, averaged out and the residual instability of the oscillator begins to dominate the ADEV measurement curve. This effect can happen in real oscillator ADEV measurements and should be watched out for.

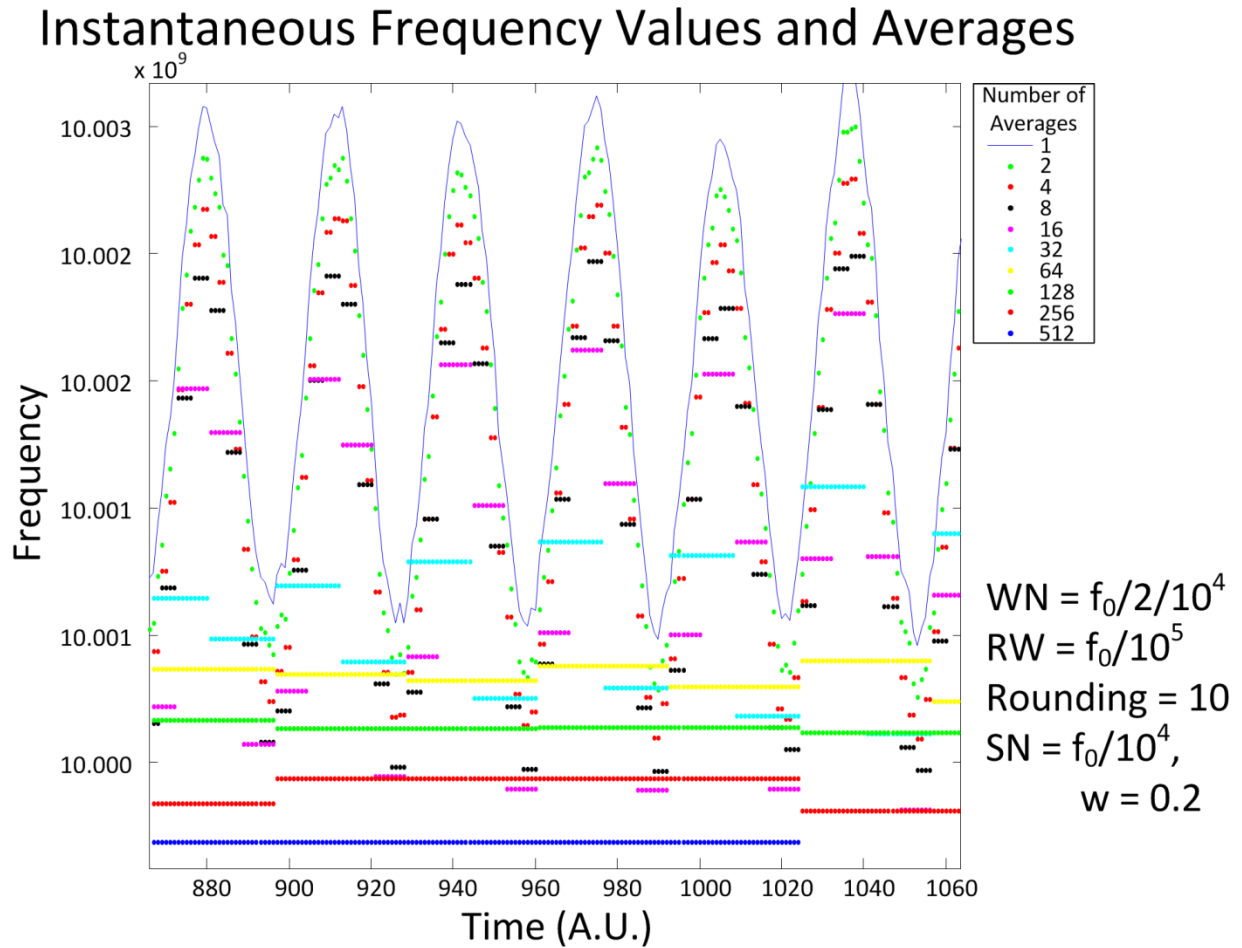


**Figure A.14** A subset of the instantaneous frequency values from last example along with measurement time averages used to calculate the ADEV curve.

An additional consideration in performing ADEV measurements is quantization error, where the fluctuations in frequency happen at magnitudes smaller than the resolution of the frequency counter used. In this case, the small fluctuations are rounded up to larger values with less variation, resulting in lower calculated instability than actually exists in the oscillator. This can be prevented with careful consideration of frequency counter model and measurement setup.

**APPENDIX B:**  
**LIST OF PUBLICATIONS AND CONFERENCES**

## **Primary Author**

C. G. Williams, F. Quinlan, and P. J. Delfyett Jr., "Injection Locked Mode-Locked Laser with Long-Term Feedback Stabilization," in Conference on Lasers and Electro-Optics/Quantum Electronics and Laser Science Conference and Photonic Applications Systems Technologies, 2008, p. CThP5.

C. Williams and P. J. Delfyett, "CW Injection Locking of Oscillators for Long-Term Stability of Frequency Combs," presented at the International OSA Network of Students (IONS) - North America, College Park, MD, 2009.

C. Williams, F. Quinlan, J. Davila-Rodriguez, and P. J. Delfyett Jr., "Optical Injection Locking of a Coupled Opto-Electronic Oscillator," in Conference on Lasers and Electro-Optics/International Quantum Electronics Conference and Photonic Applications Systems Technologies, 2009, p. CThF3.

C. Williams, F. Quinlan, J. Davila-Rodriguez, D. Mandridis, and P. J. Delfyett, "Injection Locked Coupled Optoelectronic Oscillator with Long-Term Feedback Stabilization," in Frontiers in Optics, 2009, p. FMD2.

C. Williams, F. Quinlan, and P. J. Delfyett, "CW injection locking for long-term stability of frequency combs," in Enabling Photonics Technologies for Defense, Security, and Aerospace Applications V, Orlando, FL, USA, 2009, pp. 733903-10.

C. Williams, F. Quinlan, and P. J. Delfyett, "Injection Locked Mode-Locked Laser with Long-Term Feedback Stabilization," presented at the International OSA Network of Students (IONS) - 5 Barcelona, Sp, 2009.

C. Williams, F. Quinlan, and P. J. Delfyett, "Injection-Locked Mode-Locked Laser With Long-Term Stabilization and High Power-per-Combine," IEEE Photonics Technology Letters, vol. 21, pp. 94-96, Jan-Feb 2009.

C. Williams, D. Mandridis, J. Davila-Rodriguez, and P. J. Delfyett, "Injection locked coupled opto-electronic oscillator for optical frequency comb generation," in SPIE Defense, Security, and Sensing, Orlando, FL, 2011.

C. Williams, J. Davila-Rodriguez, D. Mandridis, and P. J. Delfyett, "Noise Characterization of an Injection-Locked COEO With Long-Term Stabilization," Lightwave Technology, Journal of, vol. 29, pp. 2906-2912, 2011.

C. Williams, D. Mandridis, J. Davila-Rodriguez, A. Klee, and P. J. Delfyett, "Dependence of RF frequency on injected optical frequency of an injection locked coupled opto-electronic oscillator," in Photonics Conference (PHO), 2011 IEEE, 2011, pp. 477-478.

C. Williams, J. Davila-Rodriguez, K. Bagnell, and P. J. Delfyett Jr., "Stabilization of an Injection Locked Harmonically Mode-Locked Laser via Polarization Spectroscopy for Frequency Comb Generation," in *Lasers and Electro-Optics (CLEO), 2012 Conference on*, San Jose, CA, 2012, p. JTh2A.50

C. Williams, J. Davila-Rodriguez, K. Bagnell, and P. J. Delfyett, "Tunable frequency combs for photonic applications," in *Avionics, Fiber- Optics and Photonics Technology Conference (AVFOP), 2012 IEEE*, 2012, pp. 7-8.

## **Secondary Author**

F. Quinlan, C. Williams, S. Ozharar, and P. J. Delfyett, "Measurement of the comb dynamics for feedback control of an etalon-based coupled optoelectronic oscillator," *Optics Letters*, vol. 33, pp. 1422-1424, Jul 1 2008.

F. Quinlan, C. Williams, S. Ozharar, and P. J. Delfyett, "Fixed-point frequency measurements of an intracavity etalon-based coupled optoelectronic oscillator," in *IEEE Lasers and Electro-Optics Society, 2008. LEOS 2008. 21st Annual Meeting of the*, 2008, pp. 628-629.

F. J. Quinlan, C. Williams, S. Ozharar, and P. J. Delfyett, "Self-Stabilization of the Optical Frequencies and Pulse Repetition Rate in a Coupled Optoelectronic Oscillator," in *Conference on Lasers and Electro-Optics/Quantum Electronics and Laser Science Conference and Photonic Applications Systems Technologies*, 2008, p. CTuM3.

F. Quinlan, C. Williams, S. Ozharar, S. Gee, and P. J. Delfyett, "Self-Stabilization of the Optical Frequencies and the Pulse Repetition Rate in a Coupled Optoelectronic Oscillator," *Journal of Lightwave Technology*, vol. 26, pp. 2571-2577, Jul-Aug 2008.

J. Davila-Rodriguez, M. Akbulut, C. Williams, and P. J. Delfyett, "Multi-heterodyne mixing of frequency stabilized combs for ultrafast signal processing," in *SPIE Defense, Security, and Sensing*, 2010.

J. Davila-Rodriguez, I. Ozdur, C. Williams, and P. J. Delfyett, "A Frequency Stabilized Semiconductor Mode-Locked Laser with a Phase Modulator and an Intra-Cavity Etalon," in *Lasers and Electro-Optics (CLEO) and Quantum Electronics and Laser Science Conference (QELS), 2010 Conference on*, 2010, p. CWJ5.

J. Davila-Rodriguez, I. Ozdur, C. Williams, and P. J. Delfyett, "A semiconductor-based, frequency-stabilized mode-locked laser using a phase modulator and an intracavity etalon," *Opt. Lett.*, vol. 35, pp. 4130-4132, 2010.

J. Davila-Rodriguez, C. Williams, M. Akbulut, and P. J. Delfyett, "Multi-heterodyne characterization of multi-gigahertz spaced optical frequency comb sources," in *Lasers and Electro-Optics (CLEO) and Quantum Electronics and Laser Science Conference (QELS), 2010 Conference on*, 2010, pp. 1-2.

D. Mandridis, I. Ozdur, C. Williams, and P. J. Delfyett, "100 MHz chirped pulse and frequency comb laser source using an intra-cavity etalon and long-term stabilization," in IEEE Photonics Society, 2010 23rd Annual Meeting of the, 2010, pp. 301-302.

M. Bagnell, J. Davila-Rodriguez, C. Williams, and P. J. Delfyett, "White light sampling and cross-correlation via multi-heterodyne detection with an optical frequency comb," in Lasers and Electro-Optics (CLEO), 2011 Conference on, 2011, pp. 1-2.

J. Davila-Rodriguez, M. Bagnell, C. Williams, and P. J. Delfyett, "Multiheterodyne Detection for Spectral Compression and Downconversion of Arbitrary Periodic Optical Signals," *Lightwave Technology, Journal of*, vol. 29, pp. 3091-3098, 2011.

J. Davila-Rodriguez, I. Ozdur, C. Williams, D. Mandridis, P. J. Delfyett, J. J. Plant, and P. W. Juodawlkis, "Ultralow noise, etalon stabilized, 10 GHz optical frequency comb based on a Slab-Coupled Waveguide Amplifier," in Lasers and Electro-Optics (CLEO), 2011 Conference on, 2011, pp. 1-2.

J. Davila-Rodriguez, C. Williams, M. Bagnell, and P. J. Delfyett, "Frequency combs with multi-gigahertz spacing from semiconductor mode-locked lasers and applications in multiheterodyne detection for the measurement of arbitrary optical waveforms," in International Summer Session: Lasers and Their Applications, Changchun, China, 2011, p. Tu11.

P. J. Delfyett, D. Mandridis, C. Williams, I. Ozdur, M. Bagnell, and A. Klee. (2011, 23 March 2011). Diode laser produces low-noise chirped pulses. SPIE Newsroom. Available: <http://spie.org/x47376.xml>

D. Mandridis, C. Williams, I. Ozdur, and P. J. Delfyett, "Low noise stabilized chirped pulse Theta laser for photonic ADC," in Lasers and Electro-Optics (CLEO), 2011 Conference on, 2011, pp. 1-2.

D. Mandridis, C. Williams, I. Ozdur, and P. J. Delfyett, "Low noise chirped pulse mode-locked laser using an intra-cavity Fabry-Pérot etalon," *Opt. Express*, vol. 19, pp. 8994-8999, 2011.

D. Mandridis, C. Williams, I. Ozdur, A. Klee, and P. J. Delfyett, "Semiconductor-based low-noise 100 MHz chirped pulse laser source based on a theta cavity design with an intra-cavity etalon and long-term stabilization (Invited)," in SPIE Defense, Security, and Sensing, Orlando, FL, 2011.

A. Klee, D. Mandridis, C. Williams, and P. J. Delfyett, "Direct Comparison of Semiconductor and Erbium-Based Frequency Stabilized Harmonically Mode-Locked Lasers," in IEEE Photonics Conference, 2011, Arlington, VA, 2011, pp. 887-888.

J. Davila-Rodriguez, M. Bagnell, C. Williams, P. J. Delfyett, J. J. Plant, and P. W. Juodawlkis, "An all-diode ultralow noise 10 GHz frequency comb and MOPA system with 0.39 W output power based on Slab-Coupled Optical Waveguide Amplifiers," in Lasers and Electro-Optics (CLEO), 2012 Conference on, 2012, pp. 1-2.



- M. D. Weed, C. Williams, P. J. Delfyett, and W. V. Schoenfeld, "Feedback in coupled-resonance optical waveguides," in Lasers and Electro-Optics (CLEO), 2012 Conference on, 2012, pp. 1-2.
- P. J. Delfyett, M. Bagnell, S. Bhoopapur, J. Davila-Rodriguez, N. Hoghooghi, I. Ozdur, M. Piracha, and C. Williams, "Coherent optical signal processing using optical frequency combs," in Avionics, Fiber- Optics and Photonics Technology Conference (AVFOP), 2012 IEEE, 2012, pp. 22-23.
- J. Davila-Rodriguez, C. Williams, P. J. Delfyett, J. J. Plant, and P. W. Juodawlkis, "All-diode generation and amplification of 10 GHz pulse-trains from coupled-cavity mode-locked lasers using Slab-Coupled Waveguide Amplifiers," in Avionics, Fiber- Optics and Photonics Technology Conference (AVFOP), 2012 IEEE, 2012, pp. 70-71.
- A. C. Klee, J. Davila-Rodriguez, M. Bagnell, and P. J. Delfyett, "Multiheterodyne detection for self-referenced characterization of complex arbitrary waveforms from largely detuned optical frequency combs," in Avionics, Fiber- Optics and Photonics Technology Conference (AVFOP), 2012 IEEE, 2012, pp. 102-103.
- A. Klee, J. Davila-Rodriguez, M. Bagnell, and P. J. Delfyett, "Self-referenced spectral phase retrieval of dissimilar optical frequency combs via multiheterodyne detection," in *Photonics Conference (IPC)*, 2012 IEEE, 2012, pp. 491-492.
- A. Klee, J. Davila-Rodriguez, C. Williams, and P. Delfyett, "Characterization of semiconductor-based optical frequency comb sources using generalized multi-heterodyne detection," *Selected Topics in Quantum Electronics*, IEEE Journal of, vol. PP, pp. 1-1, 2013.
- M. D. Weed, C. G. Williams, P. J. Delfyett, and W. V. Schoenfeld, "Coupling to Coupled-Resonator Optical Waveguide Loops," *IEEE Journal of Lightwave Technology*, 2013 (accepted).
- A. Klee, J. Davila-Rodriguez, C. Williams, and P. Delfyett, "Generalized Spectral Magnitude and Phase Retrieval Algorithm for Self-Referenced Multiheterodyne Detection," *J. Lightw. Technol.*, vol. PP, 2013 (submitted).

**APPENDIX C:**  
**MATLAB CODE USED FOR SIMULATIONS**

## **Pound Drever Hall and Polarization Spectroscopy Error Signal**

```
% Initialization
clear all; clc
l = 2.5e8; %Calculating Window Half-Width
FSR = 100e6; % FSR
w0=0; % Center Frequency
points = 2^14;
ff = linspace(w0-l,w0+l,points); %Frequency Vector
% Load Measured Error Signals for Comparison
lexp = .33*l;offset = -0.9e6;% Define x offset and stretch ratio for ExpErr
ffexp = linspace(w0-lexp+offset,w0+lexp+offset,2500);%Measured ErrSig freq
load ExperErrFeb2013;% Plot 2nd col for 2 spike ErrSig, col4 for lock ErrSig
R1 = 0.99; % Reflectivity of Cavity
O=1.115*FSR; % Phase Modulation Frequency
Airy =@(w) (R1*(exp(1i.*2*pi*(w-w0)/FSR)-1)./(1-R1^2*exp(1i.*2*pi*(w-
w0)/FSR)));
EFR=.45;%Defining Electric field ratio, must be <= 1;ideal was .12
% % --> .2057 results in .12 carrier power, below; Common values: 37 48
beta=.50;%Depth of Phase Modulation; Common Values: 53 69
order =36;factor = 1;% Parameters for choosing resonance window gaussian
amplitude
Phase = .45*pi;%-.45RF Phase, pi/2 yields proper signal
alpha =1.20;tauR = 1/FSR;Gain = 30;% Cavity Parameters
RG = .99;%Regenerative Gain defined between 0 and 1, where 1 is lase thresh
% % Define regenerative gain curve of cavity resonance (center only, for
figures)
gg = @(w) ((1-R1)./(1-RG+1i.*RG*tauR.*(w-w0)));
% % Define PM sideband magnitudes via bessel functions
P0 = EFR;
Pc=besselj(0,beta)^2*P0;%Define input carrier power as 1
Ps=besselj(1,beta)^2*P0; %Powers in Carrier and Sidebands
Ps2=besselj(2,beta)^2*P0;%Powers in 2nd order Carrier and Sidebands
% Cavity resonance position and locking range determination
del_wl = (Pc/tauR)*sqrt(1+alpha^2);%Locking range half-width
wplus = w0+FSR;wminus = w0-FSR;%Defines first order sideband resonance
del_SB = (Ps/tauR)*sqrt(1+alpha^2);
wplus2 = w0+2*FSR;wminus2 = w0-2*FSR;%Defines second order sideband resonance
del_SB2 = (Ps2/tauR)*sqrt(1+alpha^2);
% Amplitudes and phases (External: Airy from above)
yPhi =@(w) -asin((w-w0)./del_wl) - atan(alpha);
yPhiplus =@(w) -asin((w-wplus)./del_SB) - atan(alpha);
yPhiminus =@(w) -asin((w-wminus)./del_SB) - atan(alpha);
yPhiplus2 =@(w) -asin((w-wplus2)./del_SB2) - atan(alpha);
yPhiminus2 =@(w) -asin((w-wminus2)./del_SB2) - atan(alpha);
yAmp =@(w) Gain*exp(-(w-w0)/del_wl).^order);
yAmpplus =@(w) Gain*exp(-(w-wplus)/del_SB).^order);
yAmpminus =@(w) Gain*exp(-(w-wminus)/del_SB).^order);
yAmpplus2 =@(w) Gain*exp(-(w-wplus2)/del_SB2).^order);
yAmpminus2 =@(w) Gain*exp(-(w-wminus2)/del_SB2).^order);
% Finds the limit of unlocked region in w0 resonance
limit = find(yPhi(ff)<-pi/2);
if isempty(limit) == 1; limit = length(yPhi(ff));end
begin = find(abs(ff - (w0+del_wl)) < (ff(2)-ff(1)));begin = begin(1);
```

```

% % To Define Unstable region as zero phase
% yPhi =@(w) yPhi(w).*((ff(begin)) <= w | w <= ff(limit(1)));
% Putting them together
y=@(w) Airy(w).*(w < (wminus2-del_SB2*factor))...%Outside minus2 resonance
+ (yAmpminus2(w).*exp(1i.*yPhiminus2(w))).*...
((wminus2-del_SB2*factor) <= w & w <= (wminus2+del_SB2*factor))... %
Minus2 Sideband Resonance
+ Airy(w).*...
((wminus2+del_SB2*factor) <= w & w <= (wminus-del_SB*factor))... %
Between-1 & -2 resonance
+ (yAmpminus(w).*exp(1i.*yPhiminus(w))).*...
((wminus-del_SB*factor) <= w & w <= (wminus+del_SB*factor))... % Minus
Sideband Resonance
+ Airy(w).*...
((wminus+del_SB*factor) <= w & w <= (w0-del_wl*factor))... % Between Minus
and Carrier Resonance
+ (yAmp(w).*exp(1i.*yPhi(w))).*...
((w0-del_wl*factor) <= w & w <= (w0+del_wl*factor))... % Carrier Resonance
+ Airy(w).*...
((w0+del_wl*factor) <= w & w <= (wplus-del_SB*factor))+... % Between
Carrier and Plus resonance
+ (yAmpplus(w).*exp(1i.*yPhiplus(w))).*...
((wplus-del_SB*factor) <= w & w <= (wplus+del_SB*factor))... % Plus
sideband resonance
+ Airy(w).*...
((wplus+del_SB*factor) <= w & w <= (wplus2-del_SB2*factor))+... % Between
Carrier and Plus resonance
+ (yAmpplus2(w).*exp(1i.*yPhiplus2(w))).*...
((wplus2-del_SB2*factor) <= w & w <= (wplus2+del_SB2*factor))... % Minus2
Sideband Resonance
+ Airy(w).*(w > (wplus2+del_SB2*factor)); %Outside plus2 resonance

%% Plot Passive and Active Cavity Amplitudes and Phases
figure(100);set(gcf,'name','Cavity Response Window');
subplot(2,1,1);plot(ff,abs(Airy(ff)),'.',ff,angle(Airy(ff))/pi);xlim([w0-
1e8,w0+1e8])
ylim([-1.2,1.2])
title('Etalon Response'); legend('Airy Reflection Amplitude','Phase')
ylabel({'Transmission (A.U.)',' and Phase (\pi Rad)'});xlabel('Detuning
Frequency')
subplot(2,1,2);plot(ff,abs(y(ff))/max(abs(y(ff))),ff,angle(y(ff))/pi);xlim([w
0-1e8,w0+1e8])
ylim([-1.2,1.2])
title('Cavity with Gain Response');legend ('Injection Transmission','Phase')
ylabel({'Transmission (A.U.)',' and Phase (\pi Rad)'});xlabel('Detuning
Frequency')

%% Cavity Resonance Figure with bells and whistles for Publishing
figure(500);set(gcf,'name','Cavity Response Window');clf
hh = plot(...
[w0-del_wl*5,w0+del_wl*5],[0,0],'--k',[w0,w0],[-.9,1],'--k',... %Plot axes
1&2
ff,(100*abs(gg(ff)).^2),'b',...%Plot Regenerative Gain 3
ff,Airy(ff)+1,'g',ff,abs(y(ff))/30,'og',ff,angle(y(ff))/pi,'r',...% Plot all
phase and amplitude functions 4,5,6

```

```

ff(limit(1:(begin-limit(1))))),angle(y(ff(limit(1:(begin-
limit(1))))))/pi, '.b',... %unstable region 7
[w0-del_wl,w0+del_wl],[acot(alpha)/pi,acot(alpha)/pi], 'c',...% Plot upper
(y) phase limit 8
[w0-del_wl,w0+del_wl],[-pi/2/pi,-pi/2/pi], 'c',...% Plot lower (y) phase
limit 9
[w0-del_wl,w0-del_wl],[-0.5,0.5], 'c',[w0+del_wl,w0+del_wl],[-
0.5,0.5], 'c',...%Plot x Limits on locking range 10&11
[0,0],[0,0];%End plot, to be able to mix and match above plot commands
ylim([-1.2,1.15]);
kk=1;xlim([w0-1/kk,w0+1/kk]);
% want legend for 4,5,6,7,8
for ij = [1,2,9,10,11,12]

set(get(get(hh(ij), 'Annotation'), 'LegendInformation'), 'IconDisplayStyle', 'off
');
end
text(-.1e8,-1, 'w0')
text(0.25e8,-1.11,['alpha = ',num2str(alpha)])
set(gca, 'xticklabel', {[[]}])
set(gca, 'yticklabel', {[[]}])
legend({'Regenerative Gain of Cavity', 'Airy Function of Passive Cavity',...
'Amplified Signal Input', 'Cavity Phase', 'Unstable Region',...
'Phase Limits'}, 'Location', 'SouthEast');
title('Laser Cavity Resonance');
ylabel('Phase,\phi_{L} (\pi Rad)');xlabel('Detuning Frequency')

%% Plot Cavity Response Detail of w0 Resonance
figure(101);set(gcf, 'name', 'Cavity Response Detail'); clf
% h =
plot(ff(limit(begin:limit(end))),angle(y(ff(limit(begin:limit(end))))))/pi, '.b
',...
h = plot(ff(limit),angle(y(ff(limit)))/pi, '.b',...
[w0-del_wl,w0+del_wl],...
[acot(alpha)/pi,acot(alpha)/pi], 'c',...% Plot upper phase limit
[w0-del_wl,w0+del_wl],[-pi/2/pi,-pi/2/pi], 'c',...% Plot lower phase limit
[w0-del_wl,w0-del_wl],[-0.5,0.5], 'c',...
[w0+del_wl,w0+del_wl],[-0.5,0.5], 'c',...%Plot x Limits on locking range
ff,Airy(ff)+1, 'g',ff,abs(y(ff))/30, 'og',...
ff,angle(y(ff))/pi, 'r',... % Plot all phase and amplitude functions
[w0-del_wl*5,w0+del_wl*5],[0,0], '--k',[w0,w0],[-1,1], '--k');%Plot axes
ylim([-1.25,1.25]);
k=1;xlim([w0-1/k,w0+1/k]);
title('Laser Cavity Resonance');
ylabel('Phase,\phi_{L} (\pi Rad)');xlabel('Detuning Frequency')
% Delete values from legend:
for ij = [3,4,5,9,10]
set(get(get(h(ij), 'Annotation'), 'LegendInformation'))...
, 'IconDisplayStyle', 'off');
end
legend({'Unstable Region', 'Injection Lock Phase Limits',...
'Airy Amplitude', 'Cavity Amplitude Response',...
'Complete Phase Response'}, 'Location', 'SouthEast')

%% PDH Error Signal Calculation

```

```

% ****RF Phase is specified in initialization, above ****
% % Conventional Error Signal
G=@(w) (Airy(w).*conj(Airy(w+O))-conj(Airy(w)).*Airy(w-O))*exp(1i*Phase);
% % Modified PDH Error Signal
Gy=@(w) (Y(w).*conj(Y(w+O))-conj(Y(w)).*Y(w-O))*exp(1i*Phase);

%% Initial plotting of PDH Error Signals for comparison
figure(102); clf; hold on; j=1.5; xlim([w0-1/j,w0+1/j])
plot(-ff,G(ff),-ff,Gy(ff)/60,'g');
set(gcf,'name','Error Signal Comparison - Wide View')
title('Error Signal Comparison');
legend('Error Signal','Injection Locked Error Signal');
ylabel('Arbitrary Units'); xlabel('Detuning Frequency')
text(0.18e8,1,['PM Frequency = ',num2str(O/1e6),' MHz'])
text(0.18e8,2,['RF Phase = ',num2str(Phase/pi),'*\pi'])

%% Plot Error signal on top of Cavity Resonance
figure(101); hold on;
% plot(ff,Gy(ff)/abs(max(Gy(ff))),'.k')
xpos = 0.18e8; ypos = -0.2;
text(xpos,ypos,['PM Frequency = ',num2str(O/1e6),' MHz'])
text(xpos,ypos-0.1,['RF Phase = ',num2str(Phase/pi),'*\pi'])
text(xpos,ypos-0.2,['EFR = ',num2str(EFR)])
text(xpos,ypos-0.3,['Gaussian Order = ',num2str(order)])
text(xpos,ypos-0.4,['alpha = ',num2str(alpha)])

%% Plot 101 with Measured Error Signal for comparison
figure(107); clf
plot(-ffexp,ExperErr(:,2)-.23,ff,(+Gy(ff)/max(abs(Gy(ff)))), 'r');
hold on; plot(ff,abs(Y(ff))/max(abs(Y(ff))), 'g', ff, ...
    angle(Y(ff))/max(angle(Y(ff))), 'c')
ylim([-2,1.2]); xlim([-0.8e8,.8e8]);
xpos1 = 0.7e8; xpos2 = 0.2e8; ypos = -1.2;
text(-xpos1,ypos,['PM Frequency = ',num2str(O/1e6),' MHz'])
text(-xpos1,ypos-0.2,['RF Phase = ',num2str(Phase/pi),'*\pi'])
text(-xpos1,ypos-0.4,['EFR = ',num2str(EFR)])
text(-xpos1,ypos-0.6,['Gaussian Order = ',num2str(order)])
text(xpos2,ypos,['alpha = ',num2str(alpha)])
text(xpos2,ypos-0.2,['Beta = ',num2str(beta)])
text(xpos2,ypos-0.4,['R1 = ',num2str(R1)])
text(xpos2,ypos-0.6,['X-vector Ratio = ',num2str(lexp/1)])

%% Produce frequency shifted copies of error signal
ESig = +Gy(ff)/max(abs(Gy(ff)));
ESigTot = +Gy(ff)/max(abs(Gy(ff)))...
    +circshift(ESig,([0 ceil((FSR/(2*1))*points)]))...
    +.15+circshift(ESig,([0 -ceil((FSR/(2*1))*points)]))+.15;
figure(107); hold on;
plot(ff,circshift(ESig,([0 ceil((FSR/(2*1))*points)]))+.15,'-m');
plot(ff,circshift(ESig,([0 -ceil((FSR/(2*1))*points)]))+.15,'-k');

% Plot sum total of all three
figure(108); plot(ff,ESigTot); xlim([-0.7e8,.7e8]);

```

```

%% Determine correct phase by plotting at different phases:
figure(103); hold on; clf
for ii=1:4;
    phase2 = (ii)*(pi/4);
    G2=@(w) (Airy(w).*conj(Airy(w+0))-conj(Airy(w)).*Airy(w-0))*exp(1i*phase2);
    Gy2=@(w) (Y(w).*conj(Y(w+0))-conj(Y(w)).*Y(w-0))*exp(1i*phase2);
    subplot(4,1,ii);plot(ff,G2(ff)/2,'-.',ff,Gy2(ff)/max(abs(Gy2(ff))));
    xlim([-2e8,2e8]);
    text(xpos,ypos-0.4,['phase = ',num2str(phase2/pi),'*\pi'])
    ii*10;% Counter, delete semicolon to activate
end

%% Hansch Couillaud Error Signal - not complete yet
% Initialization
load HCExpErrSig %load experimental HC error signal
HCOffset = -4e6;HClexp = .225*1; %0.469*1
HCffexp = linspace(w0-HClexp+HCOffset,w0+HClexp+HCOffset,2500);
theta = 0.25*pi; %Determines percentage launched into each polarization.
% Controls magnitude and polarity of Error Signal
C = 0.5*3e8*8.85e-12; % Constant used in HC
P0 = EFR*.08;order = 14;
del_wlHC = (P0/tauR)*sqrt(1+alpha^2);%Locking range half-width
% Determine polarization electric field magnitudes:
Epar =@(w) 1*exp(1i.*w)*cos(theta);
Eper =@(w) 1*exp(1i.*w)*sin(theta);
% Original H-C Equations
% Erpar =@(w) Epar(w).*(sqrt(R1)-((1-R1)/sqrt(R1))*R1*...
% exp(1i.*2*pi*(w-w0)/FSR)./(1-R1*exp(1i.*2*pi*(w-w0)/FSR)));
Erpar =@(w) Epar(w).*Airy(w);% Leave Erpar, above, but is simply
% Airy*input wave, tho above is slightly wrong.
Erper =@(w) Eper(w).*sqrt(R1);
% ErperHC =@(w) Erper(w); %Perhaps redefine this to include birefringence?
% Amplitudes and phases (must be redefined to make each resonance the same)
yPhiHC =@(w) -asin((w-w0)./del_wlHC) - atan(alpha);
yPhiplusHC =@(w) -asin((w-wplus)./del_wlHC) - atan(alpha);
yPhiminusHC =@(w) -asin((w-wminus)./del_wlHC) - atan(alpha);
yAmpHC =@(w) Gain*exp(-(w-w0)/del_wlHC).^order);
yAmpplusHC =@(w) Gain*exp(-(w-wplus)/del_wlHC).^order);
yAmpminusHC =@(w) Gain*exp(-(w-wminus)/del_wlHC).^order);
ErparHC=@(w) Erpar(w).*(Airy(w).*(w < (wminus-del_wlHC*factor))... % Outside
+ (yAmpminusHC(w).*exp(1i.*yPhiminusHC(w))).*...
((wminus-del_wlHC*factor) <= w & w <= (wminus+del_wlHC*factor))... % '-'
Resonance
+ Airy(w).*...
((wminus+del_wlHC*factor) <= w & w <= (w0-del_wlHC*factor))... % Between
'-' and w0
+ (yAmpHC(w).*exp(1i.*yPhiHC(w))).*...
((w0-del_wlHC*factor) <= w & w <= (w0+del_wlHC*factor))... % w0 Resonance
+ Airy(w).*...
((w0+del_wlHC*factor) <= w & w <= (wplus-del_wlHC*factor))+... % Between
w0 and '+'
+ (yAmpplusHC(w).*exp(1i.*yPhiplusHC(w))).*...
((wplus-del_wlHC*factor) <= w & w <= (wplus+del_wlHC*factor))... % '+'
resonance
+ Airy(w).*(w > (wplus+del_wlHC*factor))); %Outside '+' ;

```

```

% % Experimenting with dispersion (2 polarization signals):
% ErparHC=@(w) Airy(w).*(w < (w0-del_wl*factor))...
% + (yAmpHC(w).*exp(1i.*yPhiHC(w))).*...
% ((w0-del_wl*factor) <= w & w <= (w0+del_wl*factor))... % w0 Resonance
% + Airy(w).*(w > (w0+del_wl*factor)); %Outside plus resonance;
wper = w0+3e8;
% del_wlHCper = (P0*sin(theta)/tauR)*sqrt(1+alpha^2);%Locking range half-
width
% yPhiHCper = @(w) -asin((w-wper)./del_wlHCper) - atan(alpha);
% yAmpHCper = @(w) Gain*exp(-(w-wper)/del_wlHCper).^order);
% ErperHC=@(w) Airy(w).*(w < (wper-del_wlHCper*factor))...
% + (yAmpHCper(w).*exp(1i.*yPhiHCper(w))).*...
% ((wper-del_wlHCper*factor)<=w & w <=(wper+del_wlHCper*factor))... % w0
Resonance
% + Airy(w).*...
% (w > (wper+del_wlHCper*factor)); %Outside plus resonance;
AiryHC = @(w) (R1*(exp(1i.*2*pi*(w-wper)/FSR)-1)./...
(1-R1^2*exp(1i.*2*pi*(w-wper)/FSR)));
ErperHC = @(w) Eper(w).*AiryHC(w);
% Error Signal Definitions
% % Note: Error and Error1 are equivalent.
Error = @(w) -C*abs(1*exp(1i.*w)).^2*1*cos(theta)*sin(theta)*(1-R1)*R1.*...
sin(2*pi*(w-w0)/FSR)./((1-R1).^2+4*R1*sin(2*pi*(w-w0)/FSR/2).^2);
Error1 = @(w) C*((abs(0.5*(Erpar(w)+1i.*Erper(w))).^2-...
(abs(0.5*(Erpar(w)-1i.*Erper(w))).^2));
% Error2 = @(w) C*((abs(0.5*(ErparHC(w)+1i.*ErperHC(w))).^2-...
% (abs(0.5*(ErparHC(w)-1i.*ErperHC(w))).^2));
Error2 = @(w) C*((abs(0.5*(ErparHC(w)+1i.*ErperHC(w))).^2-...
(abs(0.5*(ErparHC(w)-1i.*ErperHC(w))).^2));
figure(209); plot(ff,-Error1(ff),ff,Error(ff));ylim([-5e-4,5e-4])
% Error2 = @(w) -C*(abs(0.5*(Epar(w)*ErparHC(w)+1i.*(Erper(w)).^2)).^2-...
% abs(0.5*(Epar(w)*ErparHC(w)-1i.*(Erper(w)).^2)).^2);
% Error2 = @(w) -C*(abs(0.5*(ErparHC(w)+1i.*ErperHC(w)).^2-...
% abs(0.5*(ErparHC(w)-1i.*ErperHC(w)).^2));
% F = 50;% Amplify factor
% Plot Cavity Resonance Amp and Phase, Error Signals,
figure(200);clf;set(gcf,'name','HC Error Signal Simulation')
plot(ff,abs(ErparHC(ff))/max(abs(ErparHC(ff))),...
ff,angle(ErparHC(ff))./Epar(ff)/pi,...
ff,Error(ff)/max(abs(Error(ff))),ff,Error2(ff)/max(abs(Error2(ff))));
legend('Amplitude Response','Phase Response/\pi',...
'Original Error Signal','New Error','Location','SouthEast')
title('Hansch-Couillaud Error Signal');
ylabel('Arbitrary Units');xlabel('Detuning Frequency')
jj = 5;xlim([w0-1/jj,w0+1/jj]);ylim([-1.25,1.25])
% % Plot Sim Error signal vs measured
figure(201)
plot(ff,Error2(ff)/max(abs(Error2(ff))),...
-HCffexp,HCErrSig(:,2)/max(HCErrSig(:,2))+.2)
xlim([-1.5e8,1.5e8]); ylim([-1.25,1.25])
xpos1 = -3e7;xpos2 = 2e7;ypos = -.23;
text(xpos1,ypos,['EFR = ',num2str(P0)])
text(xpos1,ypos-.1,['Gaussian Order = ',num2str(order)])
text(xpos2,ypos,['alpha = ',num2str(alpha)])

```



```

text(xpos2,ypos-0.1,['R1 = ',num2str(R1)])
text(xpos2,ypos-0.2,['X-vector Ratio = ',num2str(HClexp/1)])

%% Plot comparison of HC to PDH Error Signals
figure(300);clf;set(gcf,'name','PDH vs. HC Error Signals')
F = 50; %Amplify factor
plot(ff,G(ff),'b',ff,Gy(ff)/60,'g',ff,Error(ff)*1000,'.b',...
     ff,-F*Error2(ff),'r')
legend('PDH Error Signal','PDH Error Signal, Cavity with Gain',...
       'HC Error Signal','HC Error Signal, Cavity with Gain');
title('Hansch-Couillaud Error Signal');
ylabel('Arbitrary Units');xlabel('Detuning Frequency')
xlim([w0-1/j,w0+1/j])
% % Comparison of HC to PDH Measured Signals
figure(700)
plot(-HCffexp,HCErrSig(:,2)/max(HCErrSig(:,2)),...
     -ffexp,ExperErr(:,2)/max(ExperErr(:,2)))
xlim([-5e7,5e7])

```

## **Allan Deviation Simulation**

```

clear all
clc
datapoints = 1024*4;
f = zeros(datapoints,1);
% DEFINE 'INSTANTANEOUS' FREQUENCY
% for continuously drifting frequency.
f(1) = 10e9;f0 = f(1);
% f = linspace(10e9,11e9,datapoints);
% for random walk drift
% for nn = 2:datapoints
%     f(nn) = f(nn-1) + 100*(rand -.5) + 0*rand;
% end
RW = f0/10^15; %Random Walk Magnitude
WN = f0/1/10^5; %White Noise Magnitude
SN = 1*f0/1/10^15; %Sinusoidal Modulation Magnitude
w = .2; %Sinusoidal Modulation Frequency
f = RW*cumsum(rand(1,datapoints) - 0.5) + WN*(rand(1,datapoints) - 0.5) ...
    + SN*cos(w*(1:1:datapoints)) + f0;
f = round(f/10)*10;% to Add in quantization error - appropriate level is
% relative to the level of noise
%OBSERVATION: Ratio of random walk to white noise determines the shape, but
% the magnitude of those (probably relative to the nominal frequency)
% determines the vertical offset
%OBSERVATION: More white noise leads to longer downslope at short ADEV
% times.
%OBSERVATION: significant white noise (10 order of mag higher than RW)
% results in SAME ADEV and STDEV. Conversely, significant RW compared to
% WN results in flat value of STDEV, increasing value of ADEV - hence the
% advantage of ADEV.
y = f; tau0 = 1;
[sig2,tau,ff] = avar(y,tau0);
ADEV = sqrt(sig2)/f0;
% [sig2,tau] = avarold(y,tau0);

```

```

% ADEVold = sqrt(sig2);
%(tau0 is the original simple spacing, so make it equal to 1, no big deal)
% The output is the tau and allan variance, take the sqrt to get deviation,
% ff is array of averaged vectors for use in figures
[sig3,tau1] = stvar(y,tau0);
STDEV = sqrt(sig3)/f0;
% fm = reshape(ff,[datapoints,1]);
%% Plot Instantaneous Values, ADEV, and STDEV
figure(3);clf
subplot(3,1,1); plot(f);%ylim([f0-1e7,f0+1e7])
title('Instantaneous Frequency Values','FontSize',12,'FontWeight','bold');
xlabel('Time(A.U.)');ylabel('Frequency')
subplot(3,1,2);loglog(tau,ADEV,'.-');ylim([10^-10,10^-2])
title('Allan Deviation','FontSize',12,'FontWeight','bold');
xlabel('Measurement Time(Units of number of values used)');
ylabel('Fractional Frequency Deviation')
subplot(3,1,3);loglog(tau1,STDEV,'.-',tau,(STDEV-ADEV));ylim([10^-10,10^-2])
title('Standard Deviation','FontSize',12,'FontWeight','bold');
xlabel('Measurement Time(Units of number of values used)');
ylabel('Fractional Frequency Deviation')

%% Plot offset average vectors
figure(2);clf % graphing the averages used for ADEV
plot(f); hold on;
plot(ff(:,1)-.2e6,'.g')
plot(ff(:,2)-.4e6,'.r')
plot(ff(:,3)-.6e6,'.k')
plot(ff(:,4)-.8e6,'.m')
plot(ff(:,5)-1e6,'.c')
plot(ff(:,6)-1.2e6,'.y')
plot(ff(:,7)-1.4e6,'.g')
plot(ff(:,8)-1.6e6,'.r')
plot(ff(:,9)-1.8e6,'.b')
title('Instantaneous Frequency Values and Averages');
xlabel('Time(A.U.)');ylabel('Frequency')

```

## REFERENCES

- [1] T. Udem, R. Holzwarth, and T. W. Hänsch, "Optical frequency metrology," *Nature*, vol. 416, pp. 233-237, 2002.
- [2] S. A. Diddams, "The evolving optical frequency comb [Invited]," *J. Opt. Soc. Am. B*, vol. 27, pp. B51-B62, 2010.
- [3] N. R. Newbury, "Searching for applications with a fine-tooth comb," *Nat Photon*, vol. 5, pp. 186-188, 2011.
- [4] S. A. Diddams, A. Bartels, T. M. Ramond, C. W. Oates, S. Bize, E. A. Curtis, J. C. Bergquist, and L. Hollberg, "Design and control of femtosecond lasers for optical clocks and the synthesis of low-noise optical and microwave signals," *Selected Topics in Quantum Electronics, IEEE Journal of*, vol. 9, pp. 1072-1080, 2003.
- [5] R. J. Jones, K. D. Moll, M. J. Thorpe, and J. Ye, "Phase-Coherent Frequency Combs in the Vacuum Ultraviolet via High-Harmonic Generation inside a Femtosecond Enhancement Cavity," *Physical Review Letters*, vol. 94, p. 193201, 2005.
- [6] S.-W. Kim, "Metrology: Combs rule," *Nat Photon*, vol. 3, pp. 313-314, 2009.
- [7] S. T. Cundiff, "Metrology: New generation of combs," *Nature*, vol. 450, pp. 1175-1176, 2007.
- [8] T. Udem, S. A. Diddams, K. R. Vogel, C. W. Oates, E. A. Curtis, W. D. Lee, W. M. Itano, R. E. Drullinger, J. C. Bergquist, and L. Hollberg, "Absolute Frequency Measurements of the Hg<sup>+</sup> and Ca Optical Clock Transitions with a Femtosecond Laser," *Physical Review Letters*, vol. 86, p. 4996, 2001.
- [9] T. Rosenband, D. B. Hume, P. O. Schmidt, C. W. Chou, A. Brusch, L. Lorini, W. H. Oskay, R. E. Drullinger, T. M. Fortier, J. E. Stalnaker, S. A. Diddams, W. C. Swann, N. R. Newbury, W. M. Itano, D. J. Wineland, and J. C. Bergquist, "Frequency Ratio of Al<sup>+</sup> and Hg<sup>+</sup> Single-Ion Optical Clocks; Metrology at the 17th Decimal Place," *Science*, vol. 319, pp. 1808-1812, March 28, 2008.
- [10] I. Coddington, W. C. Swann, L. Nenadovic, and N. R. Newbury, "Rapid and precise absolute distance measurements at long range," *Nature Photonics*, vol. 3, pp. 351-356, Jun 2009.
- [11] M. U. Piracha, D. Nguyen, D. Mandridis, T. Yilmaz, I. Ozdur, S. Ozharar, and P. J. Delfyett, "Range resolved lidar for long distance ranging with sub-millimeter resolution," *Optics Express*, vol. 18, pp. 7184-7189, Mar 29 2010.
- [12] M. U. Piracha, D. Nguyen, I. Ozdur, and P. J. Delfyett, "Chirped pulse lidar using a mode locked laser source for metrology," in *Photonics Conference (PHO), 2011 IEEE*, 2011, pp. 700-701.
- [13] M. T. Murphy, U. Th, R. Holzwarth, A. Sizmann, L. Pasquini, C. Araujo-Hauck, H. Dekker, S. D. Odorico, M. Fischer, T. W. Hänsch, and A. Manescau, "High-precision wavelength calibration of astronomical spectrographs with laser frequency combs," *Monthly Notices of the Royal Astronomical Society*, vol. 380, pp. 839-847, 2007.
- [14] T. Steinmetz, T. Wilken, C. Araujo-Hauck, R. Holzwarth, T. W. Hänsch, L. Pasquini, A. Manescau, S. D'Odorico, M. T. Murphy, T. Kentischer, W. Schmidt, and T. Udem, "Laser Frequency Combs for Astronomical Observations," *Science*, vol. 321, pp. 1335-1337, September 5, 2008.
- [15] D. A. Braje, M. S. Kirchner, S. Osterman, T. Fortier, and S. A. Diddams, "Astronomical spectrograph calibration with broad-spectrum frequency combs," *European Physical Journal D*, vol. 48, pp. 57-66, 2008.

- [16] L. Chih-Hao, J. B. Andrew, E. C. Claire, C. Guoqing, C. Li-Jin, F. Peter, F. Gabor, G. G. Alexander, X. K. Franz, F. P. David, S. Dimitar, S. Andrew, and W. Ronald, "Femtosecond Laser Frequency Comb for Precision Astrophysical Spectroscopy," 2009, p. CM11.
- [17] F. Quinlan, S. Ozharar, S. Gee, and P. J. Delfyett, "Harmonically mode-locked semiconductor-based lasers as high repetition rate ultralow noise pulse train and optical frequency comb sources," *Journal of Optics A-Pure and Applied Optics*, vol. 11, pp. -, Oct 2009.
- [18] A. Bartels, D. Heinecke, and S. A. Diddams, "Passively mode-locked 10 GHz femtosecond Ti:sapphire laser," *Opt. Lett.*, vol. 33, pp. 1905-1907, 2008.
- [19] S. Ozharar, I. Ozdur, F. Quinlan, and J. P. J. Delfyett, "Optical frequency comb generation by direct modulation of CW light," in *Enabling Photonics Technologies for Defense, Security, and Aerospace Applications IV*, Orlando, FL, USA, 2008, pp. 69750J-9.
- [20] S. Ozharar, F. Quinlan, I. Ozdur, S. Gee, and P. J. Delfyett, "Ultraflat optical comb generation by phase-only modulation of continuous-wave light," *IEEE Photonics Technology Letters*, vol. 20, pp. 36-38, Jan-Feb 2008.
- [21] S. Ozharar, S. Gee, F. Quinlan, S. Lee, and P. J. Delfyett, "Pulse-amplitude equalization by negative impulse modulation for rational harmonic mode locking," *Optics Letters*, vol. 31, pp. 2924-2926, Oct 1 2006.
- [22] J. Chen, J. W. Sickler, E. P. Ippen, and F. X. Käertner, "Low Timing-Jitter High Repetition-Rate Femtosecond Pulse Trains via Locking to External Fabry-Perot Cavities," in *Conference on Lasers and Electro-Optics/Quantum Electronics and Laser Science Conference and Photonic Applications Systems Technologies*, 2008, p. CFI6.
- [23] A. Martinez and S. Yamashita, "Multi-gigahertz repetition rate passively modelocked fiber lasers using carbon nanotubes," *Opt. Express*, vol. 19, pp. 6155-6163, 2011.
- [24] J. Chen, W. S. Jason, E. P. Ippen, and F. X. Kaertner, "High Repetition Rate, Low Jitter, Fundamentally Mode-Locked Soliton Er-Fiber Laser," in *Conference on Lasers and Electro-Optics/Quantum Electronics and Laser Science Conference and Photonic Applications Systems Technologies*, 2007, p. CThHH3.
- [25] J. W. Nicholson and D. J. DiGiovanni, "High-Repetition-Frequency Low-Noise Fiber Ring Lasers Mode-Locked With Carbon Nanotubes," *Photonics Technology Letters, IEEE*, vol. 20, pp. 2123-2125, 2008.
- [26] P. J. Delfyett, L. T. Florez, N. Stoffel, T. Gmitter, N. C. Andreadakis, Y. Silberberg, J. P. Heritage, and G. A. Alphonse, "High-Power Ultrafast Laser-Diodes," *IEEE Journal of Quantum Electronics*, vol. 28, pp. 2203-2219, Oct 1992.
- [27] P. J. Delfyett, S. Gee, M.-T. Choi, H. Izadpanah, W. Lee, S. Ozharar, F. Quinlan, and T. Yilmaz, "Optical Frequency Combs From Semiconductor Lasers and Applications in Ultrawideband Signal Processing and Communications," *IEEE Journal of Lightwave Technology*, vol. 24, pp. 2701-2719, Jul 2006.
- [28] P. W. Juodawlkis, J. C. Twichell, G. E. Betts, J. J. Hargreaves, R. D. Younger, J. L. Wasserman, F. J. O'Donnell, K. G. Ray, and R. C. Williamson, "Optically sampled analog-to-digital converters," *Microwave Theory and Techniques, IEEE Transactions on*, vol. 49, pp. 1840-1853, 2001.
- [29] J. Zhi, D. E. Leaird, H. Chen-Bin, M. Houxun, M. Kourogi, K. Imai, and A. M. Weiner, "Spectral Line-by-Line Pulse Shaping on an Optical Frequency Comb Generator," *Quantum Electronics, IEEE Journal of*, vol. 43, pp. 1163-1174, 2007.
- [30] G. Li, "Recent advances in coherent optical communication," *Adv. Opt. Photon.*, vol. 1, pp. 279-307, 2009.

- [31] F. Quinlan, S. Gee, S. Ozharar, and J. P. J. Delfyett, "Semiconductor based, high repetition rate mode-locked lasers for time and frequency based coherent communications and signal processing applications," in *Enabling Photonics Technologies for Defense, Security, and Aerospace Applications III*, Orlando, FL, USA, 2007, pp. 65720B-14.
- [32] T. Yilmaz, C. M. DePriest, T. Turpin, J. H. Abeles, and P. J. Delfyett, "Toward a photonic arbitrary waveform generator using a modelocked external cavity semiconductor laser," *IEEE Photonics Technology Letters*, vol. 14, pp. 1608-1610, Nov 2002.
- [33] D. J. Jones, S. A. Diddams, J. K. Ranka, A. Stentz, R. S. Windeler, J. L. Hall, and S. T. Cundiff, "Carrier-Envelope Phase Control of Femtosecond Mode-Locked Lasers and Direct Optical Frequency Synthesis," *Science*, vol. 288, pp. 635-639, April 28, 2000 2000.
- [34] T. Ohara, "160-Gb/s OTDM transmission using integrated all-optical MUX/DEMUX with all-channel modulation and demultiplexing," *IEEE Photonics Technology Letters*, vol. 16, p. 650, 2004.
- [35] P. J. Delfyett and B. K. Mathason, "Toward terabit networking, instrumentation, and signal processing using hybrid WDM-OTDM technologies," in *Terahertz and Gigahertz Electronics and Photonics II*, San Diego, CA, USA, 2000, pp. 9-15.
- [36] S. A. Diddams, D. J. Jones, J. Ye, S. T. Cundiff, J. L. Hall, J. K. Ranka, R. S. Windeler, R. Holzwarth, T. Udem, and T. W. Hänsch, "Direct Link between Microwave and Optical Frequencies with a 300 THz Femtosecond Laser Comb," *Physical Review Letters*, vol. 84, p. 5102, 2000.
- [37] S. M. Foreman, K. W. Holman, D. D. Hudson, D. J. Jones, and J. Ye, "Remote transfer of ultrastable frequency references via fiber networks," *Review of Scientific Instruments*, vol. 78, pp. 021101-25, 2007.
- [38] J. Davila-Rodriguez, M. Bagnell, C. Williams, and P. J. Delfyett, "Multiheterodyne Detection for Spectral Compression and Downconversion of Arbitrary Periodic Optical Signals," *Lightwave Technology, Journal of*, vol. 29, pp. 3091-3098, 2011.
- [39] M. Bagnell, J. Davila-Rodriguez, C. Williams, and P. J. Delfyett, "Multiheterodyne Detection and Sampling of Periodically Filtered White Light for Correlations at 20 km of Delay," *Photonics Journal, IEEE*, vol. 4, pp. 504-511, 2012.
- [40] F. R. Giorgetta, CoddingtonI, BaumannE, W. C. Swann, and N. R. Newbury, "Fast high-resolution spectroscopy of dynamic continuous-wave laser sources," *Nat Photon*, vol. 4, pp. 853-857, 2010.
- [41] Z. W. Barber, F. R. Giorgetta, P. A. Roos, I. Coddington, J. R. Dahl, R. R. Reibel, N. Greenfield, and N. R. Newbury, "Characterization of an actively linearized ultrabroadband chirped laser with a fiber-laser optical frequency comb," *Opt. Lett.*, vol. 36, pp. 1152-1154, 2011.
- [42] G. C. Valley, "Photonic analog-to-digital converters," *Opt. Express*, vol. 15, pp. 1955-1982, 2007.
- [43] A. S. Bhushan, F. Coppinger, and B. Jalali, "Time-stretched analogue-to-digital conversion," *Electronics Letters*, vol. 34, pp. 839-841, 1998.
- [44] Y. Han and B. Jalali, "Photonic Time-Stretched Analog-to-Digital Converter: Fundamental Concepts and Practical Considerations," *J. Lightwave Technol.*, vol. 21, p. 3085, 2003.
- [45] D. Mandridis, I. Ozdur, F. Quinlan, M. Akbulut, J. J. Plant, P. W. Juodawlkis, and P. J. Delfyett, "Low-noise, low repetition rate, semiconductor-based mode-locked laser source suitable for high bandwidth photonic analog-digital conversion," *Applied Optics*, vol. 49, pp. 2850-2857, May 20 2010.
- [46] D. Mandridis, I. Ozdur, C. Williams, and P. J. Delfyett, "100 MHz chirped pulse and frequency comb laser source using an intra-cavity etalon and long-term stabilization," in *IEEE Photonics Society, 2010 23rd Annual Meeting of the*, 2010, pp. 301-302.

- [47] D. Mandridis, C. Williams, I. Ozdur, and P. J. Delfyett, "Low noise chirped pulse mode-locked laser using an intra-cavity Fabry-Pérot etalon," *Opt. Express*, vol. 19, pp. 8994-8999, 2011.
- [48] M. Becker, D. Kuizenga, and A. Siegman, "Harmonic mode locking of the Nd:YAG laser," *Quantum Electronics, IEEE Journal of*, vol. 8, pp. 687-693, 1972.
- [49] A. L. Schawlow and C. H. Townes, "Infrared and Optical Masers," *Physical Review*, vol. 112, pp. 1940-1949, 1958.
- [50] T. Yilmaz, C. M. DePriest, A. Braun, J. Abeles, and P. J. Delfyett, "Noise in Fundamental and Harmonic Modelocked Semiconductor Lasers: Experiments and Simulations," *IEEE Journal of Quantum Electronics*, vol. 39, pp. 838-849, 2003.
- [51] F. Rana, H. L. T. Lee, R. J. Ram, M. E. Grein, L. A. Jiang, E. P. Ippen, and H. A. Haus, "Characterization of the noise and correlations in harmonically mode-locked lasers," *J. Opt. Soc. Am. B*, vol. 19, pp. 2609-2621, 2002.
- [52] S. Gee, F. Quinlan, S. Ozharar, and P. J. Delfyett, "Simultaneous optical comb frequency stabilization and super-mode noise suppression of harmonically mode-locked semiconductor ring laser using an intracavity etalon," *IEEE Photonics Technology Letters*, vol. 17, pp. 199-201, Jan 2005.
- [53] F. Quinlan, S. Gee, S. Ozharar, and P. J. Delfyett, "Ultralow-jitter and amplitude-noise semiconductor-based actively mode-locked laser," *Optics Letters*, vol. 31, pp. 2870-2872, Oct 1 2006.
- [54] I. T. Ozdur, S. Ozharar, M. Akbulut, F. Quinlan, D. Mandridis, and P. J. Delfyett, "Frequency Stabilized Mode-Locked Laser with 1000 Finesse Intracavity Etalon," in *Conference on Lasers and Electro-Optics/Quantum Electronics and Laser Science Conference and Photonic Applications Systems Technologies*, 2009, p. CMII4.
- [55] J. Davila-Rodriguez, I. Ozdur, C. Williams, and P. J. Delfyett, "A semiconductor-based, frequency-stabilized mode-locked laser using a phase modulator and an intracavity etalon," *Opt. Lett.*, vol. 35, pp. 4130-4132, 2010.
- [56] Y. Katagiri and A. Takada, "Supermode selection of a subterahertz-harmonic colliding-pulse mode-locked semiconductor laser using continuous-wave light injection," *Photonics Technology Letters, IEEE*, vol. 9, pp. 1564-1566, 1997.
- [57] F. Quinlan, S. Gee, S. Ozharar, and J. Delfyett, Peter, "Supermode noise suppression of a harmonically modelocked laser by external optical injection," in *Enabling Photonics Technologies for Defense, Security, and Aerospace Applications II*, Orlando (Kissimmee), FL, USA, 2006, pp. 624300-5.
- [58] F. Quinlan, S. Gee, S. Ozharar, and P. J. Delfyett, "Greater than 20-dB supermode noise suppression and timing jitter reduction via CW injection of a harmonically mode-locked laser," *IEEE Photonics Technology Letters*, vol. 19, pp. 1221-1223, Jul-Aug 2007.
- [59] A. Pikovsky, M. Rosenblum, and J. Kurths, "Discovery of synchronization by Christiaan Huygens," in *Synchronization: A Universal Concept in Nonlinear Sciences*, ed: Cambridge University Press, 2001, pp. 357-361.
- [60] M. Bennett, M. F. Schatz, H. Rockwood, and K. Wiesenfeld, "Huygens's clocks," *Proceedings of the Royal Society of London. Series A: Mathematical, Physical and Engineering Sciences*, vol. 458, pp. 563-579, 8 March 2002.
- [61] K. Kurokawa, "Noise in Synchronized Oscillators," *Microwave Theory and Techniques, IEEE Transactions on*, vol. 16, pp. 234-240, 1968.
- [62] K. Kurokawa, "Injection locking of microwave solid-state oscillators," *Proceedings of the IEEE*, vol. 61, pp. 1386-1410, 1973.

- [63] H. L. Stover and W. H. Steier, "LOCKING OF LASER OSCILLATORS BY LIGHT INJECTION," *Applied Physics Letters*, vol. 8, pp. 91-93, 1966.
- [64] C. J. Buczek, R. J. Freiberg, and M. L. Skolnick, "Laser injection locking," *Proceedings of the IEEE*, vol. 61, pp. 1411-1431, 1973.
- [65] A. Siegman, "Lasers," ed Sausalito, CA: University Science Books, 1986, pp. 1073-1074, 1129-1170
- [66] B. Razavi, "A study of injection locking and pulling in oscillators," *Solid-State Circuits, IEEE Journal of*, vol. 39, pp. 1415-1424, 2004.
- [67] Y. K. Park, G. Giuliani, and R. L. Byer, "Stable single-axial-mode operation of an unstable-resonator Nd:YAG oscillator by injection locking," *Opt. Lett.*, vol. 5, pp. 96-98, 1980.
- [68] Y. Park, G. Giuliani, and R. Byer, "Single axial mode operation of a Q-switched Nd:YAG oscillator by injection seeding," *Quantum Electronics, IEEE Journal of*, vol. 20, pp. 117-125, 1984.
- [69] C. Henry, "Theory of spontaneous emission noise in open resonators and its application to lasers and optical amplifiers," *Lightwave Technology, Journal of*, vol. 4, pp. 288-297, 1986.
- [70] C. Henry, N. Olsson, and N. Dutta, "Locking range and stability of injection locked 1.54  $\mu\text{m}$  InGaAsP semiconductor lasers," *Quantum Electronics, IEEE Journal of*, vol. 21, pp. 1152-1156, 1985.
- [71] M. Osinski and J. Buus, "Linewidth broadening factor in semiconductor lasers--An overview," *Quantum Electronics, IEEE Journal of*, vol. 23, pp. 9-29, 1987.
- [72] S. Kobayashi and T. Kimura, "Optical phase modulation in an injection locked AlGaAs semiconductor laser," *Quantum Electronics, IEEE Journal of*, vol. 18, pp. 1662-1669, 1982.
- [73] C.-H. Chang, L. Chrostowski, and C. J. Chang-Hasnain, "Injection locking of VCSELs," *Selected Topics in Quantum Electronics, IEEE Journal of*, vol. 9, pp. 1386-1393, 2003.
- [74] E. K. Lau, W. Liang Jie, and M. C. Wu, "Enhanced Modulation Characteristics of Optical Injection-Locked Lasers: A Tutorial," *Selected Topics in Quantum Electronics, IEEE Journal of*, vol. 15, pp. 618-633, 2009.
- [75] N. Hoghooghi, I. Ozdur, M. Akbulut, J. Davila-Rodriguez, and P. J. Delfyett, "Resonant cavity linear interferometric intensity modulator," *Optics Letters*, vol. 35, pp. 1218-1220, Apr 15 2010.
- [76] N. Hoghooghi and P. J. Delfyett, "Theoretical and Experimental Study of a Semiconductor Resonant Cavity Linear Interferometric Intensity Modulator," *Lightwave Technology, Journal of*, vol. 29, pp. 3421-3427, 2011.
- [77] T. Jung, S. Ji-Lin, D. T. K. Tong, S. Murthy, M. C. Wu, T. Tanbun-Ek, W. Wenshen, R. Lodenkamper, R. Davis, L. J. Lembo, and J. C. Brock, "CW injection locking of a mode-locked semiconductor laser as a local oscillator comb for channelizing broad-band RF signals," *Microwave Theory and Techniques, IEEE Transactions on*, vol. 47, pp. 1225-1233, 1999.
- [78] A. Takada and W. Imajuku, "Linewidth narrowing and optical phase control of mode-locked semiconductor ring laser employing optical injection locking," *Photonics Technology Letters, IEEE*, vol. 9, pp. 1328-1330, 1997.
- [79] R. Adler, "A Study of Locking Phenomena in Oscillators," *Proceedings of the IRE*, vol. 34, pp. 351-357, 1946.
- [80] L. J. Paciorek, "Injection locking of oscillators," *Proceedings of the IEEE*, vol. 53, pp. 1723-1727, 1965.
- [81] C. Henry, "Theory of the linewidth of semiconductor lasers," *Quantum Electronics, IEEE Journal of*, vol. 18, pp. 259-264, 1982.

- [82] F. Mogensen, H. Olesen, and G. Jacobsen, "Locking Properties and Stability Properties for a Semiconductor Laser with External Light Injection," *IEEE Journal of Quantum Electronics*, vol. QE-21, July 1985.
- [83] R. Lang, "Injection Locking Properties of a Semiconductor Laser," *IEEE Journal of Quantum Electronics*, vol. QE-18, pp. 976-983, June 1982.
- [84] R. W. P. Drever, J. L. Hall, F. V. Kowalski, J. Hough, G. M. Ford, A. J. Munley, and H. Ward, "Laser phase and frequency stabilization using an optical resonator," *Applied Physics B: Lasers and Optics*, vol. 31, pp. 97-105, 1983.
- [85] R. Pound, "Electronic Frequency Stabilization of Microwave Oscillators," *Rev. Sci. Instrum.*, vol. 17, p. 490, 1946.
- [86] E. D. Black, "An introduction to Pound-Drever-Hall laser frequency stabilization," *Am. J. Phys.*, vol. 69, pp. 79-88, 4 April 2000.
- [87] V. Wulfmeyer, M. Randall, A. Brewer, and R. M. Hardesty, "2- $\mu$ m Doppler lidar transmitter with high frequency stability and low chirp," *Opt. Lett.*, vol. 25, pp. 1228-1230, 2000.
- [88] A. Sträßer, T. Waltinger, and M. Ostermeyer, "Injection seeded frequency stabilized Nd:YAG ring oscillator following a Pound-Drever-Hall scheme," *Appl. Opt.*, vol. 46, pp. 8358-8363, 2007.
- [89] M. Ostermeyer, T. Waltinger, and M. Gregor, "Frequency stabilization of a Q-switched Nd:YAG laser oscillator with stability better 300 kHz following an rf-sideband scheme," *Optics Communications*, vol. 282, pp. 3302-3307, 2009.
- [90] C. Williams, F. Quinlan, and P. J. Delfyett, "Injection-Locked Mode-Locked Laser With Long-Term Stabilization and High Power-per-Combine," *IEEE Photonics Technology Letters*, vol. 21, pp. 94-96, Jan-Feb 2009.
- [91] C. G. Williams, F. Quinlan, and P. J. Delfyett Jr., "Injection Locked Mode-Locked Laser with Long-Term Feedback Stabilization," in *Conference on Lasers and Electro-Optics/Quantum Electronics and Laser Science Conference and Photonic Applications Systems Technologies*, 2008, p. CThP5.
- [92] L. C. Archundia and P. J. Delfyett, "External cavity multiwavelength semiconductor mode-locked lasers gain dynamics," *Optics Express*, vol. 14, pp. 9223-9237, Oct 2 2006.
- [93] D. von der Linde, "Characterization of the Noise in Continuously Operating Mode-Locked Lasers," *Applied Physics B*, vol. 39, pp. 201-217, 1986.
- [94] T. W. Hänsch and B. Couillaud, "Laser frequency stabilization by polarization spectroscopy of a reflecting reference cavity," *Optics Communications*, vol. 35, pp. 441-444, 1980.
- [95] J. M. Boon-Engering, W. E. van der Veer, E. A. J. M. Bente, and W. Hogervorst, "Stabilization of an optical cavity containing a birefringent element," *Optics Communications*, vol. 140, pp. 285-288, 1997.
- [96] P. Esherick and A. Owyong, "Polarization feedback stabilization of an injection-seeded Nd:YAG laser for spectroscopic applications," *J. Opt. Soc. Am. B*, vol. 4, pp. 41-47, 1987.
- [97] C. Williams, J. Davila-Rodriguez, K. Bagnell, and P. J. Delfyett Jr., "Stabilization of an Injection Locked Harmonically Mode-Locked Laser via Polarization Spectroscopy for Frequency Comb Generation," in *Lasers and Electro-Optics (CLEO), 2012 Conference on*, San Jose, CA, 2012, p. JTh2A.50
- [98] C. Williams, F. Quinlan, J. Davila-Rodriguez, and P. J. Delfyett Jr., "Optical Injection Locking of a Coupled Opto-Electronic Oscillator," in *Conference on Lasers and Electro-Optics/International Quantum Electronics Conference and Photonic Applications Systems Technologies*, 2009, p. CThF3.



- [99] C. Williams, F. Quinlan, J. Davila-Rodriguez, D. Mandridis, and P. J. Delfyett, "Injection Locked Coupled Optoelectronic Oscillator with Long-Term Feedback Stabilization," in *Frontiers in Optics*, 2009, p. FMD2.
- [100] C. Williams, J. Davila-Rodriguez, D. Mandridis, and P. J. Delfyett, "Noise Characterization of an Injection-Locked COEO With Long-Term Stabilization," *Lightwave Technology, Journal of*, vol. 29, pp. 2906-2912, 2011.
- [101] C. Williams, D. Mandridis, J. Davila-Rodriguez, and P. J. Delfyett, "Injection locked coupled optoelectronic oscillator for optical frequency comb generation," in *SPIE Defense, Security, and Sensing*, Orlando, FL, 2011.
- [102] N. Yu, E. Salik, and L. Maleki, "Ultralow-noise mode-locked laser with coupled optoelectronic oscillator configuration," *Opt. Lett.*, vol. 30, pp. 1231-1233, 2005.
- [103] E. Salik, Y. Nan, and L. Maleki, "An Ultralow Phase Noise Coupled Optoelectronic Oscillator," *Photonics Technology Letters, IEEE*, vol. 19, pp. 444-446, 2007.
- [104] I. Ozdur, M. Akbulut, N. Hoghooghi, D. Mandridis, S. Ozharar, F. Quinlan, and P. J. Delfyett, "Optical frequency stabilized coupled optoelectronic oscillator," in *LEOS Annual Meeting Conference Proceedings, 2009. LEOS '09. IEEE*, 2009, pp. 507-508.
- [105] X. S. Yao and L. Maleki, "Dual microwave and optical oscillator," *Opt. Lett.*, vol. 22, pp. 1867-1869, 1997.
- [106] E. Rubiola, E. Salik, S. Huang, N. Yu, and L. Maleki, "Photonic-delay technique for phase-noise measurement of microwave oscillators," *J. Opt. Soc. Am. B*, vol. 22, pp. 987-997, 2005.
- [107] C. Williams, F. Quinlan, and P. J. Delfyett, "CW injection locking for long-term stability of frequency combs," in *Enabling Photonics Technologies for Defense, Security, and Aerospace Applications V*, Orlando, FL, USA, 2009, pp. 733903-10.
- [108] D. W. Allan, "Statistics of Atomic Frequency Standards," *Proceedings of the Institute of Electrical and Electronics Engineers*, vol. 54, pp. 221-8, 1966.
- [109] D. Sullivan, D. Allan, D. Howe, and F. Walls, "Characterization of Clocks and Oscillators," in *NIST Technical Notes*, N. I. o. S. a. T. US Department of Commerce, Ed., ed. Gaithersburg, MD, USA: US Government Printing Office, 1990, p. 352.
- [110] E. Rubiola, *Phase noise and frequency stability in oscillators*. Cambridge, UK ; New York: Cambridge University Press, 2009.
- [111] C. Williams, D. Mandridis, J. Davila-Rodriguez, A. Klee, and P. J. Delfyett, "Dependence of RF frequency on injected optical frequency of an injection locked coupled opto-electronic oscillator," in *Photonics Conference (PHO), 2011 IEEE*, 2011, pp. 477-478.
- [112] D. Howe, D. Allan, and J. Barnes. *Properties of Oscillator Signals and Measurement Methods* [Web Page]. Available: <http://tf.nist.gov/phase/Properties/main.htm>
- [113] D. Howe, D. Allan, and J. Barnes, "Properties of Signal Sources and Measurement Methods," in *Symposium on Frequency Control*, Philadelphia, PA, USA, 1981.
- [114] E. Rubiola, "On the measurement of frequency and of its sample variance with high-resolution counters," *Review of Scientific Instruments*, vol. 76, pp. 054703-6, 2005.
- [115] D. W. Allan. *Allan's Time* [Web Page]. Available: <http://www.allanstime.com>
- [116] D. W. Allan. (2012). *Conversion of Frequency Stability Measures from the Time-domain to the Frequency-domain, vice-versa and Power-law Spectral Densities* [Web Page]. Available: <http://www.allanstime.com/Publications/DWA/Conversion from Allan variance to Spectral Densities.pdf>